TECHNISCHE UNIVERSITÄT MÜNCHEN

WISSENSCHAFTSZENTRUM WEIHENSTEPHAN FÜR ERNÄHRUNG, LANDNUTZUNG UND UMWELT

LEHRSTUHL FÜR ZOOLOGIE

Multimodal integration in single neurons in the midbrain of chicken (*Gallus gallus domesticus*)

Katharina Lischka

Vollständiger Abdruck der von der Fakultät Wissenschaftszentrum Weihenstephan für Ernährung, Landnutzung und Umwelt der Technischen Universität München zur Erlangung des akademischen Grades eines

Doktors der Naturwissenschaften (Dr. rer. nat.)

genehmigten Dissertation.

Vorsitzender:	Prof. Dr. Michael Schemann
Prüfer der Dissertation:	1. Prof. Dr. Harald Luksch
	2. Prof. Dr. Benjamin Schusser

Die Dissertation wurde am 29.04.2019 bei der Technischen Universität München eingereicht und durch die Fakultät Wissenschaftszentrum Weihenstephan für Ernährung, Landnutzung und Umwelt am 18.07.2019 angenommen.

Table of Contents

Summary

The chicken is a diurnal and gregarious bird with a well-developed visual and auditory system. It uses these senses to react to stimuli in its environment, e.g., predators. The neuronal pathways that relay these sensory signals are well defined, and much information is available on the processing throughout the brain. An essential area for the processing of both sensory signals is the optic tectum, a part of the midbrain. Optic tectum homologues exist in all vertebrates and are similar in structure, retinotopic map formation and function.

The cellular integration of information from different sensory modalities in this area was the major focus of this study. Particularly, I studied a cellular candidate for multimodal integration in the optic tectum, the so-called Shepherd's crook neuron (SCN). The morphology and the physiological properties of downstream target areas suggest that this cell type may integrate both auditory and visual sensory input. The Shepherd crook cell has two dendritic arborization fields: an apical dendrite terminating in retinorecipient layers of the optic tectum, and a basal dendrite terminating in deeper layers where auditory information is available. The axon of the Shepherd's crook neuron originates from the apical dendrite with direct axodendritic signal propagation of the visual information without passing the soma. Immunohistological experiments were performed to determine the expression patterns of different ion channels and structural proteins. A multi-compartment model based on the expression patterns was created which explained the signal propagation recorded in physiological experiments.

The results show that SCN hold all the attributes to integrate different sensory information precisely timed and at high frequencies. The morphology and the expression patterns of structural proteins indicate the location of the axon initial segment at the axon just after branching off from the apical dendrite. Data from the multi-compartment model showed a higher activity on the axon compared to the soma. This axodendritic generation of action potentials was also seen in the direction of signal propagation in slice experiments, where the signal always spread from this axodendritic region to the soma (independent of stimulation site (visual, auditory, audiovisual)). In summary, this study revealed that Shepherd's crook neurons are involved in the integration of visual and auditory signals in the optic tectum. As a result of the

audiovisual processing, SCN may contribute to the formation of a multimodal map of space in the optic tectum.

Zusammenfassung

Das Huhn ist ein tagaktiver und in Gruppen lebender Vogel mit einem gut entwickelten visuellen und auditorischen System. Diese Sinne benutzt es unter anderem, um auf wichtige Reize in der Umgebung wie z.B. Fressfeinde zu reagieren. Die verschiedenen Projektionsbahnen dieser sensorischen Informationen im Gehirn wurden im Detail studiert. Während der Weiterleitung passieren beide sensorische Signale eine gemeinsame Hirnregion: das optische Tektum, einem Teil des Mittelhirns. Diese Region findet sich bei allen Wirbeltieren und weist grundlegende Ähnlichkeiten in der Struktur, der Bildung einer retinotopischen Karte und der Funktion auf.

Die hier vorliegende Arbeit beschäftigt sich mit der zellulären Integration verschiedener sensorischer Informationen in diesem Gehirnareal. Speziell wurde ein charakteristischer Zelltyp, das Shepherd's Crook Neuron (SCN) untersucht, dass auf Grund seiner Morphologie sowie physiologischer Daten seines Zielgebietes einen guten Kandidaten für die Integration beider sensorischer Modalitäten darstellt. Diese Zelle besitzt zwei große dendritische Areale: apikale Dendriten in retinorezipienten Schichten des Tektums und basale Dendriten in Schichten, die auditorische Eingänge erhalten. Das Axon zweigt dabei charakteristischerweise vom apikalen Dendriten ab, was eine direkte Weitergabe der Erregung ohne Involvierung des Somas vermuten lässt. Es wurden immunhistochemische Experimente durchgeführt, um die Expression verschiedener Ionenkanäle und Strukturproteine zu lokalisieren. Auf dieser Basis wurde ein Multi-Kompartiment Modell entworfen und mit physiologischen Experimenten zur Signalausbreitung untermauert.

Die Experimente zeigen, dass SCN alle Voraussetzungen besitzen, um verschiedene sensorische Informationen zeitlich präzise und mit hoher Frequenz zu integrieren. Die Morphologie und die Expressionsmuster der Strukturproteine weisen auf die Lokalisation des Axoninitiationssegments am Axonabgang vom apikalen Dendriten hin. Experimente mit einem Multi-Kompartiment Modell zeigen eine erhöhte Aktivität durch simultane Stimulation an beiden dendritischen Eingangsregionen, die vor allem am Axon sichtbar ist. Diese axodendritische Generierung eines Aktionspotentials spiegelte sich auch in der Signalausbreitung wieder.

Unabhängig von der Stimulation (visuell, auditorisch, audiovisuell) breitete sich das Signal immer von der axodendritischen Region hin zum Soma aus.

Zusammenfassend konnte diese Arbeit belegen, dass Shepherd’s Crook Neurone prinzipiell die Fähigkeit besitzen visuelle und akustische Signale zu integrieren und so zum Aufbau einer multimodalen, räumlichen Karte im optischen Tektum beitragen können.

Introduction

The introduction is modified from the Introduction sections that correspond to the following publications:

1) “Expression patterns of ion channels and structural proteins in a multimodal cell type of the avian optic tectum” (Lischka, Ladel, Luksch, & Weigel, 2018)

This article is published in The Journal of Comparative Neurology, which permits authors the reproduction of published articles for dissertations without charge or further license.

2) “Effects of early eye removal on the morphology of a multisensory neuron in the chicken optic tectum” (Lischka, Yan, Weigel, & Luksch, 2018)

This article is published in Brain Research, which permits authors the reproduction of published articles for dissertations without charge or further license.

Multisensory integration

Multisensory integration is defined as a process where two or more sensory information streams are combined to form a product which is distinct from the input and cannot be easily deconstructed to reconstitute the input components (Stein, Stanford, Ramachandran, Perrault, & Rowland, 2009). These differences result either in response enhancement or response depression.

Multisensory enhancement is the most reliable index of multisensory integration (Stein, Stanford, & Rowland, 2014). It describes the non-linear integration of input activity which leads to increased responses compared to the linear summation of inputs (Stein et al., 2009). In mammals, Meredith and Stein (1986) showed that multisensory integration does not only occur on network or brain level, but also in single neurons. For instance, single cells in the cat superior colliculus were stimulated by the simultaneous presence of visual and auditory input with a response that was higher than the sum of each individual response, called a multisensory

enhancement (Stein & Stanford, 2008). Regarding the integration of primary sensory inputs, the optic tectum (TeO) of birds is also a suitable model to study cellular mechanisms. In *in vivo* studies in the barn owl, Knudsen (1982) revealed the highly correlated receptive fields of tectal neuronal units responding to visual or auditory input. This correlation allows the owl to assign each environmental cue to a specific location in the optic tectum (defined by azimuth and elevation). Hence, the optic tectum constitutes a sensory map of space for its visual and auditory field. Maczko, Knudsen, and Knudsen (2006) provided the first indirect evidence that individual neuron types in the barn owl optic tectum are capable of integrating different sensory modalities. In their experiments, neuronal cells in the isthmic nuclei responded to both visual and auditory input. This was an interesting result as these nuclei only receive input from the optic tectum in chicken. Thus, it is likely that neurons in the optic tectum exhibit similar integration of audiovisual signals similar to the cat superior colliculus.

The avian midbrain

"The avian midbrain is subdivided in a part dominated by visual input, the optic tectum (TeO, counterpart to the superior colliculus in mammals) and a part dominated by auditory input, the *nucleus mesencephalicus lateralis pars dorsalis* (MLd, counterpart to the inferior colliculus (IC) in mammals). The midbrain is involved in many functions such as integrating different sensory modalities, movement initiation, bottom-up attention caused by the isthmic system and top-down attention mediated by projections from the hyperpallium (Karten, Cox, & Mpodozis, 1997; Knudsen, 2007; Knudsen, Cohen, & Masino, 1995; Luksch, 2003; Luksch & Golz, 2003; Miceli, Repérant, Bavikati, Rio, & Volle, 1997; Sridharan & Knudsen, 2015; Wylie, Gutierrez-Ibanez, Pakan, & Iwaniuk, 2009)."[1]

This thesis set out to investigate cellular mechanisms related to visual and auditory processing in the visually dominated part, the optic tectum. "The TeO is composed of 15 layers, each of which can be characterized by its cell-type specificity, connectivity, density and layer thickness (Luksch, 2003)."[2] However, the knowledge about the cell types forming the curved structure of the TeO is sparse. The most superficial layer (layer 1), called the stratum opticum, contains all the afferent axonal projections of more than 20 different types of retinal ganglion cells from the contralateral retina (Yamagata, Weiner, Dulac, Roth, & Sanes, 2006), as well as tectofugal fibers

[1] Lischka, Ladel, Luksch, & Weigel, 2018
[2] Lischka, Ladel, Luksch, & Weigel, 2018

from a projection neuron located in layer 10 (Vega-Zuniga, Trost, Schicker, Bogner, & Luksch, 2018). The terminals of retinal ganglion cells spread at least to four different superficial layers of the chicken optic tectum. There is a discrepancy of identified retinorecipient layers. Mey and Thanos (2000b) defined the layers 2 to 5 and 7 as retinorecipient, while Yamagata et al. (2006) showed that layer 3 to 5 and 7 are retinorecipient. In layer 5, horizontal multipolar cells are located that arborize locally and have no axonal structures. They might form a local inhibitory circuit with retinotectal synapses (Luksch & Golz, 2003). Layer 7 is surrounded by two densely packed cell bands (layer 6 and 8, Sebesteny, Davies, C., D., Zayatis, Németh, & Tömböl, 2002). However, layer 7 does not contain cell somata, but consists of dendritic arborizations of tectal cells from layer 10 and 11 that receive synaptic input from the terminations of retinal fibers (Sebesteny et al., 2002; Vega-Zuniga et al., 2014). In layer 10, two prominent projection neurons are described, the Shepherd's crook neuron (SCN) and the vine neuron. The SCN form a tecto-isthmic circuit with the three isthmic nuclei located close to the tectum (Garrido-Charad et al., 2018; Y. Wang, Major, & Karten, 2004), while the vine neurons contribute to the ventrothalamic circuit (Vega-Zuniga et al., 2018). In layer 13, SGC cells with large somata are located. These cells project to the nucleus rotundus and receive input via bottlebrush endings from the retinal ganglion cells (Luksch, Cox, & Karten, 1998; Luksch, Karten, Kleinfeld, & Wessel, 2001). In summary, the optic tectum is a densely packed area of cells receiving different sensory input and processing this input to other areas (reviewed in Luksch (2003) and Wylie et al. (2009)). Despite the large body of data on input and output connections, the intratectal networks of the optic tectum and its interaction with other neuronal structures are less well described.

"An advantage of the layered tectal structure is the strict distinction into input and output layers, which facilitate the study of physiological properties and signal propagation in layer-specific neurons."[3] The TeO receives input from different primary senses. "As mentioned above, the visual signal is processed by retinal ganglion cells (RGCs) and relayed from the retina to the contralateral stratum opticum via the optic tract (SO, layer 1 of the optic tectum) and terminate in retinorecipient laminae (layer 2 to 5 and 7, (Mey & Thanos, 2000a; Yamagata et al., 2006). Incoming visual information is integrated by tectal cells to generate responses to luminance, motion and direction (Jassik-Gerschenfeld & Guichard, 1972; Luksch, Khanbabaie, & Wessel, 2004; Verhaal & Luksch, 2016b), and passed on towards higher brain regions (Luksch, 2003). In addition to visual information, auditory information also reaches the TeO (Knudsen, 1982; Niederleitner & Luksch, 2012). In chicken, the auditory signal is processed from the brainstem to

[3] Lischka, Ladel, Luksch, & Weigel, 2018

two interconnected structures in the midbrain: the MLd and the TeO. The central part of the inferior colliculus (ICc) relays the auditory information either via the external part of the inferior colliculus (ICx) directly to the deeper layers of the optic tectum (Pena & Gutfreund, 2014) or across an external portion of the *formatio reticularis lateralis* (FRLx; (Niederleitner, Gutierrez-Ibanez, Krabichler, Weigel, & Luksch, 2016; Niederleitner & Luksch, 2012)."[4] The primary somatosensory information pathway in birds is similar to the pathway in mammals. It predominantly projects through the medial lemniscus distinct thalamic nuclei and terminates in separate somatosensory fields in the telencephalon (Wild, 1985, 1995). The midbrain receives also primary somatosensory information from the dorsal column and external cuneate nuclei (DCN). These projections terminate primary in intercollicular regions adjacent to and partly surrounding the MLd (Wild, 1985, 1995). "In general, the avian optic tectum integrates topographic, visual and auditory information into a multisensory map of space, which is dominated by the visual modality (Knudsen, 1982; Meredith & Stein, 1986; Witten & Knudsen, 2005)."[5]

Vision and hearing in birds

Vision and hearing in birds is essential for prey capture, escape behavior, and communication. Vision provides information about speed, resolution and range necessary to guide flight and other behaviors (Davies & Green, 1994; Gill, 2007; Perrins, 1990), while hearing mainly provides information about enemies, and other kinds of danger, social relations, and communications (Dooling, Fay, & Popper, 2000). The combination of both sensory cues facilitates the location of potential danger or social interactants.

The visual pathway is subdivided in three major projection systems, the tectofugal and the thalamofugal pathway, and a third one including the accessory optic system and the pretectum (Figure 1, Salva, Mayer, & Vallortigara, 2015; Wylie et al., 2009). All of the three visual pathways begin in the retina and innervate the contralateral hemisphere. The tectofugal pathway is the most prominent one as it contains the majority of fibers. Retinal ganglion cells project from the retina to the contralateral optic tectum, where they innervate the superficial layers. Visual input is forwarded from neurons in the deep layers (output layers) to the thalamic nucleus rotundus, which mainly receives its input from tectal cells located in the stratum griseum centrale (SGC)

[4] Lischka, Ladel, Luksch, & Weigel, 2018
[5] Lischka, Ladel, Luksch, & Weigel, 2018

(Benowitz & Karten, 1967, Luksch, Cox, & Karten, 1998). From the *nucleus rotundus*, the visual signal is propagated to the telencephalic entopallium. Tectal neurons also send descending projections to the ION and back to the retina (Crossland & Hughes, 1978; Gutiérrez-Ibáñez et al., 2012; Uchiyama, Ohno, & Kodama, 2012). The tectofugal pathway generates an orienting response to a stimulus of interest, especially when moving stimuli are presented (Frost & Nakayama, 1983; Frost, Wylie, & Wang, 1990). But there is also evidence that the tectofugal pathway is involved in discrimination of color, brightness and pattern (Engelage & Bischof, 1993; Hodos & Karten, 1970; Jarvis, 1974).

The thalamofugal pathway starts at the retina, where retinal ganglion cells project contralaterally to the *nucleus geniculatus lateralis pars dorsalis* (GLd) (in the literature also named as *nucleus opticus principalis thalami* (OPT)) in the thalamus which further conveys the information on to the dorsal pole of its telencephalic target, the visual Wulst (Karten, Hodos, Nauta, & Revzin, 1973; Medina & Reiner, 2000). The main functions of the thalamofugal pathway in chicken is fine pattern discrimination (Rogers, Lesley, J., 1995; Deng & Rogers, 2002). The third pathway involves two nuclei in the mesencephalon: nucleus lentiformis mesencephalic (LM), and nucleus of the basal optic root (nBOR). These nuclei receive visual information from the retina and processes the information to cerebellar regions. The main functions are the displacement of the visual field by self-movement, the analysis of the optic flow and the generation of optokinetic responses (Pakan & Wylie, 2006; Wylie, Pakan, Elliott, Graham, & Iwaniuk, 2007 Giolli, Blanks, & Lui, 2006; Simpson, 1984; Simpson, Leonard, & Soodak, 1988).

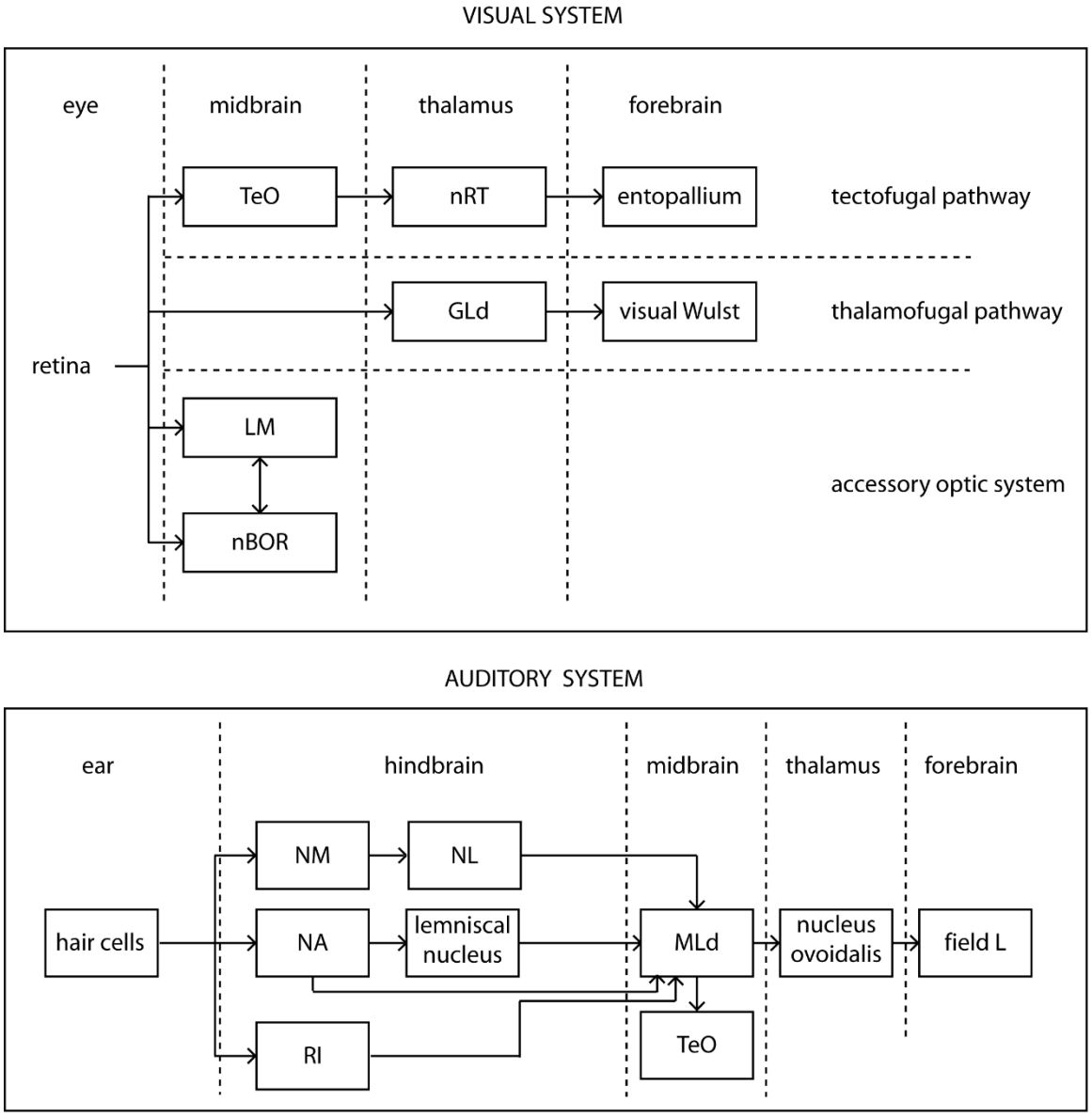

Figure 1. The visual and auditory system. The visual system is divided in three main pathways: the tectofugal pathway, the thalamofugal pathway and the accessory optic system. The auditory system only separates in different nuclei in the brainstem for the processing of time and intensity. TeO: optic tectum, LM: nucleus lentiformis mesencephali, nBOR: nucleus of the basal optic root, nRT: nucleus rotundus, GLd: nucleus geniculatus lateralis pars dorsalis, NM: nucleus magnocellularis, NA: nucleus angularis, RI: regio intermedius, NL: nucleus laminaris, MLd, mesencephalicus lateralis pars dorsalis.

The auditory pathway (Figure 1) starts at the inner ear and projects to the cochlear nuclei *nucleus angularis* (NA), *nucleus magnocellularis* (NM), and *regio intermedius* (RI). Before innervating the midbrain, the auditory projections of the NM project to an additional brainstem nucleus, the *nucleus laminaris* (NL) (Wang & Karten, 2010; Wang, Zorio & Karten, 2017). From these brainstem nuclei, the pathway continues to the *nucleus mesencephalicus lateralis pars*

dorsalis (MLd, counterpart of the inferior colliculus (IC) in mammals) in the midbrain, where it also innervates the deeper layers of the optic tectum (TeO; Niederleitner et al., 2016). In chicken, the MLd consists of three subdivisions that receive auditory input from the different brainstem nuclei (Wang & Karten, 2010). The nuclei compute distinct aspects of the auditory signal. NA processes interaural level differences (ILD) and NM processes interaural time differences (ITD, e.g. Knudsen & Konishi, 1978; MacLeod & Carr, 2005; Sullivan & Konishi, 1984). For instance, the dorsal NA responds to high frequencies and projects to the ventral MLd, while the ventral NA responds to low frequencies and projects to the dorsal MLd (Köppl & Carr, 2003; Wang & Karten, 2010). The external part of the MLd/IC (ICx) projects topographically to the optic tectum and relays information on sound localization (Knudsen & Knudsen, 1983; Pérez & Peña, 2006). As this projection was shown only in barn owls that are auditory specialists, Niederleitner et al. (2016) re-analysed this connection in the chicken and found a very sparse direct ICx-OT projection. However, these authors described an additional relay nucleus interconnected between the external portion of the inferior colliculus and the optic tectum which sends ascending input to the deep and middle layers of the optic tectum, as well as descending projections through the tectopontine-tectoreticular pathway. The axonal termination field of individual neurons covered large areas of the tectal extent, which indicated a rather coarse topography. From the midbrain the primary auditory information is passed on to *nucleus ovoidalis* (Ov) in the thalamus and ends in the auditory telencephalon (Y. Wang et al., 2017). This region comprises Field L (L1, L2a, and L3) in the caudal nidopallium (CM), the dorsal nidopallium (Nd) and the ventromedial portion of the intermediate arcopallium (Aivm). The Field L/CM complex is a laminar structure. L2a cells receive primary auditory input from cells in the Ov. The axons of L2a cells innervate the two laminas CM and L1. From these two laminas axonal projections are described back to L2a and other auditory regions in the telencephalon (Müller & Scheich, 1985; Wang, Brzozowska-Prechtl, & Karten, 2010). Hence, this primary auditory pathway relays time and intensity information, which are important for sound localization (Klump, 2013; Knudsen, 1987) and a wide range of complex sounds (Woolley & Casseday, 2004; Woolley, Gill, & Theunissen, 2006).

As described above, both the visual pathway as well as the auditory pathway are processed in the dorsal midbrain, the optic tectum. Here, distinct layers in the optic tectum are involved in the processing of different sensory signals. Likely, neuronal cells in the tectal layers integrate this signal either unimodal or bimodal.

A candidate for multisensory integration in the chicken optic tectum

“Despite the findings of visual and auditory sensory maps of space in the optic tectum of birds (Knudsen, 1982), little is known about the multimodal integration on the cellular level. A candidate cell type for multimodal integration in the optic tectum is the Shepherd’s crook neuron (SCN), the soma of which is located in layer 10 (Figure 2).

SCNs have dendrites in retinorecipient layers and deep layers, respectively. The axon of this neuron has a unique organization as it originates at the apical dendrite and immediately turns downwards in a characteristic curve crossing the deep layers to terminate in the isthmic nuclei (Garrido-Charad et al., 2018; Luksch, 2003; Ramón y Cajal, 1909). SCNs are the only tectal input neurons to the isthmic nuclei by forming a reciprocal network which is involved in bottom-up control of attention (Garrido-Charad et al., 2018; Goddard, Mysore, Bryant, Huguenard, & Knudsen, 2014; Lai, Brandt, Luksch, & Wessel, 2011; Meyer et al., 2008; Wang, Luksch, Brecha, & Karten, 2006). As units in the isthmic nuclei respond to both visual and auditory stimuli, and the isthmic nuclei receive no other input, it is likely that integration of visual and auditory input occurs upstream of the isthmic nuclei (Maczko et al., 2006).

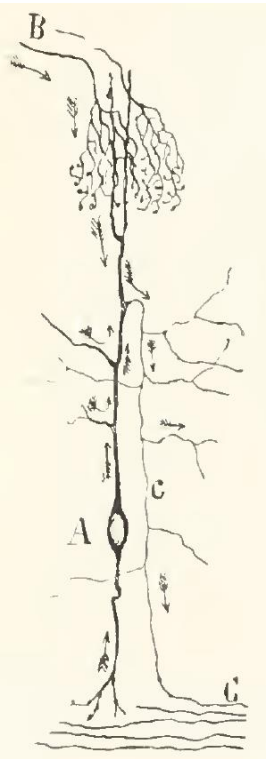

These findings strengthen the hypothesis that SCNs are cellular candidates for the integration of visual and auditory input. The Shepherd’s crook neuron had first been described by Ramón y Cajal (1909) who suggested direct information flow from visual input onto the axon, without prior integration in the neuronal soma. Axon-carrying dendrites suggest an axopetal information flow, as the soma does not participate in the initiation of nerve impulses (Triarhou, 2014). For example, in GABAergic *substantia nigra* neurons of rats, which contain an axon emerging from the dendrite, an action potential can be recorded first at the dendrite before activity in the soma occurs (Häusser, Stuart, Racca, & Sakmann, 1995).

Figure 2. Signal propagation in Shepherd's crook neurons.
Ramón y Cajal already suggested in 1909 that an incoming visual signal in cells with axon-carrying dendrites in the optic tectum directly jumps on the axon without previous passing the soma (indicated by several arrows). Moreover, these cells integrate signal from deeper layers. A: soma. B: retinal ganglion cells. C: output region. c. axon. Reproduced with permission from Ramón y Cajal, 1909.

The authors claimed that this activity pattern was the consequence of the morphological characteristic found in these neurons. Because of the unique morphology and its putative role in multisensory integration, it is of interest to understand the information flow in SCN cells, as only the visual input at the apical dendrite might reach the axonal initiation zone directly; auditory input to the lower and intermediate tectal layers would necessarily be integrated in the soma. The computation of bimodal input in tectal SCN cells could thus shed light on multimodal integration in neurons in general."[6]

Development and differentiation

"The development of the nervous system in vertebrates is characterized by a complex ensemble of cellular and molecular mechanisms (Nakamura & Sugiyama, 2004)."[7] Based on their genetic program, neurons need the appropriate molecular signals and contacts during precisely specified time windows to develop correctly (Watanabe, Sakuma, & Yaginuma, 2018). For instance, intermediate laminar organization is dependent on the expression of a guidance factor (e.g. Sema3A) and the receptor specific for this guidance factor (NRP1). When Sema3A was mis-expressed, the tangential migration of cells in the intermediate laminas was repelled (Watanabe, Sakuma, & Yaginuma, 2014). In addition, neuronal activity patterns are required in specific phases of development to, e.g., generate the fine-tuning of spatial maps and the morphological differentiation (Constantine-Paton, 1990; Eric Knudsen, 2004; Zhang & Poo, 2001). "Interrupting this precisely timed interplay leads to malformation or death of the embryo during its development (Barkovich, Millen, & Dobyns, 2009). In the precocial chicken, the sensory pathways have to be established precisely during development (Mey & Thanos, 2000a; Rubel & Fritzsch, 2002). The tectum is involved in integrating sensory information, interfacing these to both premotor networks and higher brain regions (Luksch, 2003; Wylie et al., 2009)."[8] The effect of missing sensory input on the morphology of identified neurons can be analyzed in the tectum as the individual layers contain identified neuronal cell types that can be approached with great accuracy (Heidmann & Luksch, 2001). In addition, at least for the visual input the course and trajectory of retinal fibers is clearly separated from the cells, and synaptic contact occurs at distal dendrites.

[6] Lischka, Ladel, Luksch, & Weigel, 2018
[7] Lischka, Yan, Weigel, & Luksch, 2018
[8] Lischka, Yan, Weigel, & Luksch, 2018

In general, the formation of the tectal layers during embryogenesis occurs in three spatially distinct, but chronologically overlapping, phases of cell proliferation and migration. Remarkably, tectal development progresses with a temporal delay along the rostro-ventro-lateral to caudo-dorso-medial axis in all three developmental zones. In addition, the cells also proliferate in a characteristic sequence (‘outside-in’ and ‘inside-out’ gradient) (LaVail & Cowan, 1971).

The development of the optic tectum starts at embryonic day 4 with the first wave of cell proliferation. In this first developmental step (E4 to E6) the inner zone (layer 12 and 13: stratum griseum centrale (SGC), layer 14: stratum album centrale (SAC), layer 15: stratum griseum periventriculare (SGP) and stratum fibrosum periventriculare (SFP)) is generated, followed by the development of the outer zone (layer 1 to 8 in the stratum griseum and fibrosum superficiale (SGFS)) between E4 and E8. At last, the middle zone (layer 9 to 11 in SGFS) develops between E5 and E9 (Gray, Leber, & Sanes, 1990; Gray & Sanes, 1991; Watanabe & Yaginuma, 2015). The development of the visual system is described by an interaction between the development of the eye and the development of the optic tectum. Between E6 and E14 the TeO differentiates histologically. By that time, retinal ganglion cells from the contralateral retina arrive at the anterior-ventral pole of the tectum and start to build the stratum opticum. Only a small number of retinal afferents innervate the ipsilateral hemisphere (Mey & Thanos, 2000a), and that projection appears to be lost during the first days after hatching. At E17, first visually evoked potentials can be recorded in the tectum, suggesting that retinotectal synapses have matured sufficiently to generate postsynaptic responses. In respect to the innervation of the tectum by fibers from the auditory midbrain, no data are currently available. In my thesis I focused upon a specific intermediate neuron in the optic tectum. The Shepherd’s crook neuron can be distinguished from primitive epithelial cells at day 7 ½ to 8 (Stage 33 to 34) by the appearance of their characteristic axon branch. At day 11 (stage 37) the soma reaches the intermediate layers and the distance between soma and axon branch begins to shorten by perikaryal translocation. Domesick and Morest (1977) described that the differentiation of dendrites starts after perikaryal translocation finished. In this study, the differentiation was observed by the thickening of apical and basal structures, which resulted in the formation of dendritic interactions with the retinal afferents in the superficial layers. A SCN reaches its mature form at day 19 (Domesick & Morest, 1977). I used the knowledge of the well-studied development of the chicken optic tectum, and in particular SCNs, to investigate the influence of multisensory input on single cells during their development.

Aims of this thesis

The aim of this thesis was to study the contribution of Shepherd's crook neurons to multimodal integration of the chicken optic tectum. Based on the published background of cell connectivity in the chicken optic tectum, single cell contributions to tectal networks and the role of single neurons in multimodal integration, the model system yields several features to investigate this issue. In my thesis I focused on the following questions:

- Are SCNs processing auditory information or is the cell response driven by visual input only?
- How do SCNs integrate information from two senses?
- Does simultaneous excitation from two input modalities lead to multisensory enhancement or multisensory depression?
- How do sensory inputs influence SCN development?
- Is the ability of multisensory integration already reflected on protein expression on the (sub-) cellular level?
- What is the function of the axon branch at the transition from the apical dendrite to the primary dendrite?
- Can the hypothesis of axopetal information flow put forward by Ramon y Cajal be affirmed?

This project combines neuroanatomy, electrophysiology and modeling to investigate primary sensory integration in the optic tectum of the chicken midbrain. The findings of the thesis will contribute to the cellular understanding of multimodal integration in the optic tectum.

Material and Methods

The paragraphs ‘Anesthesia’, ‘Slice preparation’, ‘Tracer injections’, ‘Antibody characterization’, ‘Immunohistochemistry’, and ‘Data analysis of colocalization’ are modified from the Material and Methods section that corresponds to the following publication:

“Expression patterns of ion channels and structural proteins in a multimodal cell type of the avian optic tectum” (Lischka, Ladel et al., 2018)

The article is published in The Journal of Comparative Neurology, which permits authors the reproduction of published articles for dissertations without charge or further license.

- -

The paragraphs ‘Enucleation’, ‘Histology and Immunohistochemistry’ and ‘Data analysis enucleation’ are modified from the Material and Methods section that corresponds to the following publication:

“Effects of early eye removal on the morphology of a multisensory neuron in the chicken optic tectum” (Lischka, Yan et al., 2018)

The article is published in Brain Research, which permits authors the reproduction of published articles for dissertations without charge or further license.

General procedure

Anesthesia

“Hatchlings of the White Leghorn chicken of both sexes were anesthetized with a mixture of ketamine (Ketamidor; 10 % solution; 100 mg/ml; Inresa Arzneimittel, dissolved with Aqua dest. 1:1) and xylazinhydrochloride (Proxylaz 2 % solution; 20 mg/ml; Bayer) at 37.5 and 5 mg/kg body weight prior to decapitation. This procedure does not require a special permit under the German Law of Animal Protection; however, animal numbers were reported to the respective authorities.”[9]

Slice preparation

“During the brain preparation and brain slicing ice-cooled oxygenated ACSF solution was used (120 mM NaCl, 3 mM KCl, 1 mM $MgCl_2$, 23 mM $NaHCO_3$, 1.2 mM NaH_2PO_4, 2 mM $CaCl_2$, 11 mM D-glucose; pH 7.4; osmolarity 305 mOsm; oxygenated with carbogen: 95 % O_2 and 5 % CO_2). After decapitation, the brain was isolated by opening the skull with one medial and two lateral cuts behind the eyes. Forebrain, hindbrain, and cerebellum were discarded, and the midbrain was separated in its two hemispheres. Each hemisphere was embedded in low-melting point agarose (low-melting point agarose, Sigma, USA, Cat# A4675-500G, 1.65 % dissolved in HEPES puffer [290 mM Saccharose, 5 mM HEPES, 3 mM KCl, 3 mM $MgCl_2 \cdot 6H_2O$; pH 7.4]) and sliced horizontally.”[10] I used 1000 µm thick slices for the tracing experiments and 500 µm thick slices for the physiological experiments. “The slices were collected in an interface recovery chamber (I-RC; idea: C. Gutierrez-Ibanez und T. Vega-Zuniga; design and development: T. Vega-Zuniga, C. Gutierrez-Ibanez, and C. Fink) filled with ACSF that was continuously oxygenated with carbogen at room temperature.”[11] Before the tracing and physiological experiments, the fluid level in the I-RC was reduced to support the viability of the cells, which were damaged during the slicing process by creating a two-condition environment. Hence, one

[9] Lischka, Ladel, Luksch, & Weigel, 2018
[10] Lischka, Ladel, Luksch, & Weigel, 2018
[11] Lischka, Ladel, Luksch, & Weigel, 2018

surface was exposed to an oxygen-rich environment, while the other surface remains supplied with nutrients form the ringer solution (Gähwiler, 1997; Y. Huang, Williams, & Johnson, 2012; Ting, Daigle, Chen, & Feng, 2014). After 1 hr, the removed ACSF was added again to the I-RC to increase the fluid level (to a level where the slices were completely covered with aCSF).

Expression patterns of structural proteins and ion channels in Shepherd's crook neurons

Tracer injections

"Electrodes for tracer injection were fabricated from borosilicate glass (GB100-8P, 0.58 x 1.00 x 80 mm, Science Products GmbH, Germany) with a microelectrode puller (P97, Sutter Instruments Co., USA)." The tip of the electrodes was broken to a tip diameter of approximately 20 µm. "Then, the electrodes were filled with mineral oil and inserted into a Nanoliter 2000 Injector (World Precision Instruments, USA). The electrode tips were filled with a dextran-coupled Texas Red solution (5 % w/v, 3000 MW, Invitrogen, Molecular Probes, Cat# D3328) dissolved in 0.1 M PB (0.023 mM $NaH_2PO_4 \cdot 1\ H_2O$, 0.08 mM $Na_2HPO_4 \cdot 2\ H_2O$, pH 7.4). SCNs were retrogradely labelled at room temperature by injecting the fluorescent dye in the *nucleus isthmi pars magnocellularis*. After the injection, the slices were incubated in oxygenated ACSF for 4 hrs at room temperature to allow transport of the tracer in SCNs. Afterwards, slices were fixed in 4 % PFA for 2 hrs and subsequently transferred into 30 % sucrose (w/v in 0.1 M PB) overnight for cryoprotection before resectioning to 25 µm thin sections with a sliding microtome (Microtome HM440E, Microm). The sections were stored in 0.1 M PB until further processing."[12]

Antibody characterization

"Alignments of the sequence of every antibody between the host species and chicken were performed with the Basic Local Alignment Search Tool (BLAST) to analyze the analogy of the antigens (Table 1). Most antigens of the target proteins were more than 80 % identical with the species the antibody was raised in. The antibody against the heavy polypeptide of neurofilament had only an analogy of 65 %. The specificity of some epitopes was already described in other studies (Table 2). In addition, Western blot analyses for sodium channel antibodies and structural proteins were conducted, as they had not been characterized in chicken tissue so far. For tissue preparation, chicken midbrain hemispheres were solubilized with a tissue homogenizer (SpeedMill PLUS, Analytic Jena, Germany) in radioimmunoprecipitation assay

[12] Lischka, Ladel, Luksch, & Weigel, 2018

buffer (150 mM NaCl, 1.0% NP-40, 0.5% sodium deoxycholate, 0.1% SDS, 50 mM Tris)."[13] The incubation of the homogenized tissue in the lysis buffer (2 hrs at 4 °C) causes the disruption of the cells and the release of proteins to the buffer. After the incubation period the solution was centrifuged at 12000 rpm for 20 min at 4 °C to separate the proteins from the cell debris. The dissolved protein solution was loaded on a gel which separated the proteins according to their size by eletrophoresis. "After electroblotting the proteins on a nitrocellulose membrane (Criterion™ Blotter, Bio-Rad) the membrane was incubated in 4 % skim milk followed by incubation in the primary antibody (1:10000 NF200, 1:200 Ankyrin G, 1:1000 PanNa_v, 1:500 Na_v1.6) overnight at 4 °C. To detect the immunosignal, the membrane was incubated with a secondary antibody (1:10000, Peroxidase AffiniPure Donkey Anti-Rabbit IgG (H+L); 1:20000, Peroxidase AffiniPure Donkey Anti-Goat IgG (H+L); Jackson Immuno Research Laboratories) for 1 hr at room temperature. Directly afterwards, the protein was detected by chemiluminescence."[14]

Immunohistochemistry

For the immunohistochemical double labelling experiments, midbrain hemispheres were sliced, SCN retrogradelly labelled and the slices resectioned as previously described in the chapter 'General Procedure – Slice Preparation' and the chapter 'Expression patterns of structural proteins and ion channels in Shepherd's crook neurons – Tracer injections', respectively. "Sections were rinsed in PBS (0.1 M PB with 0.75 % NaCl) followed by an incubation with a blocking solution (3.5 hrs at RT) containing 1 % bovine serum albumin (BSA, Roth, Cat# 0163.2), 5 % normal goat serum (NGS, Linaris S-1000, Cat# ADI-20011-100) and 0.5 % Triton X-100 (Tx100, Fluka) for staining against K_v3.1b, Na_v1.6, Pan-Na_v, and Neurofilament 200. For immunochemistry against Ankyrin G, the blocking solution contained 1 % bovine serum albumin, 5 % normal horse serum (NHS, Linaris EPN2000-50HN, Cat# EPN2000-50HN) and 0.5 % Triton X-100. Primary antibodies were diluted in 0.1 M PBS containing 1 % BSA and 1 % NGS or NHS. The sections were incubated with the primary antibodies overnight (NF200, PanNa_v, Na_v1.6, Na_v1.2 K_v3.1) or for 4 days (Ankyrin G). To identify the axon and axon initial segment (AIS) Neurofilament 200 (1:1000, Sigma-Aldrich, Cat# N4142, RRID: AB_477272) and Ankyrin G (1:200, Santa Cruz Biotechnology, Cat# sc-31778, RRID: AB_2289736) were used. To label the voltage-gated sodium and potassium channels, Na_v1.6 (1:200, Alomone Labs, Cat# ASC-009,

[13] Lischka, Ladel, Luksch, & Weigel, 2018
[14] Lischka, Ladel, Luksch, & Weigel, 2018

RRID: AB_2040202), $Na_v1.2$ (1:200, Alomone Labs, Cat# ASC-002, RRID: AB_2040005), Pan-Na_v (1:500, Alomone Labs, Cat# ASC-003, RRID: AB_2040204), $K_v3.1b$ (1:200, Alomone Labs, Cat# APC-014, RRID: AB_2040166) and $K_v3.3$ (1:200, Alomone Labs, Cat#APC-102, RRID:AB_2040170) were used. However, no antibody staining in the tectal layer 10 cell was obtained with the $K_v3.3$ antiserum in chicken and so no conclusion was made regarding the presence or absence of this channel SCNs. However, it cannot be excluded that the tested antibody against $K_v3.3$ does not bind to its epitope in the chicken midbrain at all."[15] In between the incubation in primary and secondary antibody solution, the sections were rinsed three times in PBS (0.1 M PB with 0.75 % NaCl) and again incubated in blocking solution for 30 min. "As secondary antibodies, Alexa Fluor 488 (goat anti-rabbit, 1:500, Molecular Probes, Cat# A11094, RRID: AB_221544), Alexa Fluor 488 (donkey anti-goat, 1:500, Thermo Fischer Scientific, Cat# A-11034 also A11034, RRID: AB_2576217) and Alexa Fluor 546 (goat anti-rabbit, 1:500, Thermo Fischer Scientific, Cat# A11010, RRID: AB_10584649) were used."[16] The secondary antibodies were diluted in 0.1 M PBS containing 1 % BSA. Sections were incubated in secondary antibody solution for 2h at room temperature and subsequently rinsed again three times in PBS (0.1 M PB with 0.75 % NaCl). "The sections were mounted on microscope slides and were embedded in n-Propylgallat (0.2%, diluted in DMSO, Glycerol and PBS). To specifically label myelin, the sections were incubated in FluoroMyelin (1:3000 in 0.1M PB for 20 min, F34651, Thermo Fischer Scientific), which binds at the lipophilic sites of axon sheaths."[17]

Table 1. List of all antibodies used in this study.
Note. The table specifies each antibody by its antigen and immunogen, and indicates the manufacturer, the respective Research Recourse Identifiers (RRID) as well as the dilution of each antibody. Table reproduced from Lischka, Ladel, Luksch, & Weigel, 2018, with permission from the publisher. See table 1 on page 25.

[15] Lischka, Ladel, Luksch, & Weigel, 2018
[16] Lischka, Ladel, Luksch, & Weigel, 2018
[17] Lischka, Ladel, Luksch, & Weigel, 2018

Antibody	*Antigen*	*Immunogen*	*Source, Cat. #, Host Species, clonality, RRID*	*Dilution*
anti-ankyrin G	purified C-terminus of ankyrin G from human	goat IgG	Santa Cruz Biotechnology Cat. # sc-31778 goat (polyclonal) AB_2289736	1:200
anti-calbindin	produced against recombinant rat calbindin D-28k	antiserum	Swant, Cat# CB-38a, rabbit (polyclonal) AB_10000340	1:2000
anti-K_v3.1b	amino acid residues 567-585 of rat K_v3.1b	Peptide CKESPVIAKYMPTEAVRVT	Alomone Labs Cat. # APC-014 rabbit (polyclonal) AB_2040166	1:200
anti-K_v3.3	amino acid residues 701-718 of rat K_v3.3	Peptide KSPITPGSRGRYSRDRAC	Alomone Labs Cat. # APC-102 rabbit (polyclonal) AB_2040170	1:200
anti-Na_v1.2	amino acid residues 467-485 of rat Na_v1.2	Peptide (C)ASAESRDFSGAGGIGVFSE	Alomone Labs Cat. # ASC-002 rabbit (polyclonal) AB_2040005	1:200
anti-Na_v1.6	amino acid residues 1042-1061 of rat Na_v1.6	Peptide CIANHTGVDIHRNGDFQKNG	Alomone Labs Cat. # ASC-009 rabbit (polyclonal) AB_2040202	1:200
anti-Neurofilament 200	neurofilament heavy polypeptide	IgG fraction of antiserum	Sigma-Aldrich, Cat. # N4142 rabbit (polyclonal) AB_477272	1:1000
anti-Pan-Na_v	amino acid residues 1501-1518 of rat Na_v1.1	Peptide TEEQKKYYNAMKKLGSKK(C)	Alomone Labs Cat. # ASC-003 rabbit (polyclonal) AB_2040204	1:500
Alexa Fluor 488 anti-goat produced in donkey	purified goat IgG (H+L)	goat IgG (H+L)	Thermo Fisher Scientific Cat. # A-11034 also A11034 donkey (polyclonal) AB_2576217	1:500
Alexa Flour 488 anti-rabbit produced in goat	purified rabbit IgG (H+L)	rabbit IgG (H+L)	Molecular Probes Cat. # A11094 goat (polyclonal) AB_221544	1:500
Alexa Fluor 546 anti-rabbit produced in goat	purified rabbit IgG (H+L)	rabbit IgG (H+L)	Thermo Fisher Scientific Cat. # A11010 goat (polyclonal) AB_10584649	1:500
DAPI				1:1000
Peroxidase AffiniPure Donkey Anti-Rabbit produced in donkey	purified rabbit IgG (H+L)	rabbit IgG (H+L)	Jackson ImmunoResearch Laboratories Cat. # 711-035-152 donkey (polyclonal) AB_10015282	1:10000
Peroxidase AffiniPure Donkey Anti-Goat produced in donkey	purified goat IgG (H+L)	goat IgG (H+L)	Jackson ImmunoResearch Laboratories Cat. # 705-035-147 donkey (polyclonal) AB_2313587	1:20000

Table 2. Alignments between host species of antigen and chicken.
Alignments between host species of antigen and chicken depicting the accordance of the epitope between host species and chicken and the description of this epitope in other studies on chicken. Table reproduced from Lischka, Ladel, Luksch, & Weigel, 2018, with permission from the publisher.

Epitope	***species of immunogen***	***protein similarity in chicken [%]***	***antigen alignment***	***described in literature***
anti-ankyrin G	several	82	epitope unknown no alignment possible	(H. Kuba et al., 2014), chicken
anti-calbindin	rat	79	epitope unknown no alignment possible	(Vega-Zuniga et al., 2014), chicken
anti-K_v3.1b	rat	96	rat: KESPVIAKYMPTEAVRVT chicken: KESPVIAKYMPTEAVRVT alignment:100 %	(Parameshwaran, Carr, & Perney, 2001), chicken, (Y. Wang et al., 2006), chicken; (Kuenzel, Wirth, Luksch, Wagner, & Mey, 2009), chicken
anti-K_v3.3	rat	69	rat: KSPITPGSRGRYSRDRAC chicken: sequence unknown	(Deng et al., 2005), electric fish
anti-Na_v1.2	rat	92	rat: ASAESRDFSGAGGIGVFSE chicken: AAADSRDYSGVGGIGGFSE alignment: 74 %	(Hu et al., 2009), chicken;(H. Kuba et al., 2014), chicken
anti-Na_v1.6	rat	94	rat: CIANHTGVDIHRNGDFQKN chicken: CIANHTGADIHRDIDYQKN alignment: 79 %	(H. Kuba et al., 2014), chicken
anti-Neurofilament 200	several	65	epitope unknown no alignment possible	(Shin et al., 2003), chicken
anti-Pan-Na_v	rat	88	rat: TEEQKKYYNAMKKLGSKK chicken: TEEQKKYYNAMKKLGSKK alignment: 100 %	(H. Kuba et al., 2014), chicken

Data analysis for colocalization

"To analyze the localization of the different structural proteins and ion channels on SCN neurons, fluorescence images were taken with a confocal laser scanning microscope (Olympus FV1000/IX81, Olympus, Germany) using a 60x or a 100x objective. Colocalization was analyzed in MATLAB (MATLAB, version R2017a, MathWorks®). Here, fluorescence channels were separated and sharpened as well as noise reduced by a 3D-unsharpen filter and a 3D-kernel filter. The background fluorescence based on the mean± 1.5 × S.D. of the whole-image intensity were removed. The position of the neuron in the z-axis was identified by edge detection ("canny") in the channel showing the retrogradely labelled neuron. Information at pixel positions

more than five z-slices away from the detected edge was discarded in all channels. A region of interest on the retrogradely labeled cell was defined by saving the x-y coordinates of several points on this region (soma, primary dendrite, axon) in a vector. Data of both fluorescence channels were correlated over the length of the region of interest to maintain a fluorescence intensity profile of both channels. The resulted profile plot visualized the expression of the different labeled proteins along the soma, the primary dendrite and part of the axon. The expression patterns for each target protein were averaged ($Na_v1.6$ n=29, $PanNa_v$ n=10, $K_v3,.1$ n=17, NF200 n=14, Ankyrin n=7) and plotted to an intensity profile containing all averaged expression patterns of every antibody used in this study."[18]

[18] Lischka, Ladel, Luksch, & Weigel, 2018

Multi-compartment model based on anatomical data

The multi-compartment model was implemented in Neuron (version 7.6.2, Yale University, USA) programmed with Python (version 2.7.14) in collaboration with Thomas Künzel (group leader of the Auditory Neurophysiology group at RWTH Aachen, Aachen, Germany). The compartments and their properties were based on the neuroanatomical data of Shepherd's crook neurons (see expression patterns of proteins and morphological parameters). Different sections (soma, primary dendrite, axon initial segment, axon [segmented in node and internode], apical dendrite, basal dendrite, proximal basal dendrite) were defined and shaped in length and diameter. Due to the lack of physiological details of each part of the SCNs, Hodgkin and Huxley conditions were assumed for every compartment. In the neuron model two stimulation sites (mimicking synaptic inputs) were defined: one at the apical and one at the basal dendrite. The activation of a single input region was twice as high as for activation of both input regions. Activation in the multi-compartment model means a defined stochastic distribution of input spikes at the input regions. The output as action potential rate was computed for both soma and axon. The different experimental protocols were executed, the spike rate recorded, and analyzed statistically (Kruskal-Wallis test, Mann Whitney U test).

Signal propagation in Shepherd's crook neurons after visual and auditory stimulation

Hybrid voltage sensor imaging

Immediately after slice recovery (see section 'slice preparation' under Materials and Methods) the slices were transferred to ACSF containing 0.5 µM dipicrylamine (DPA) at least 45 min before the start of the experiment. Afterwards, slices were transferred to the working chamber under the microscope and continuously perfused with oxygenated DPA-containing ACSF. To avoid floating, the slices were fixed on a poly-D-lysin coated cover slip and oriented in the recording chamber so that the stimulation electrodes could be placed on the desired positions. Bipolar electrodes were used, which were made of nichrome wire with 50 µm diameter (NC7620F, formvar coated, Science Products GmbH, Germany). The single electrodes were stuck together with insulating varnish (CRC Industries Deutschland GmbH, Germany) except for the tip. The two connected, insulated wires were stabilized by a glass capillary and connected to a wiring pin at the end of the electrode. This plug connection was used to link the electrode with the stimulus generator via a cable. The bipolar stimulation electrodes were placed in the corresponding visual and auditory sensory input regions in the TeO under microscopic control (Examiner.A1, Zeiss, Germany; Digital Sight DS-5M-L1, Nikon, Japan). To image the signal propagation SCNs were labelled with a lipophilic carbocyanine fluorescent dye (DiO, 3,3'-dioctadecyloxa-carbocyanine perchlorate; 2 µM DiO dissolved in internal solution [100 mM potassium D-gluconic acid, 40 mM KCl, 10 mM HEPES, 2 mM $MgCl_2 \cdot 6\ H_2O$, 2 mM EGTA, 2 mM Mg-ATP, 0.1 mM $CaCl_2 \cdot 2\ H_2O$; adjusted to pH 7.4 with KOH, osmolarity 264 mOsm, after DiO addition osmolarity increases to 292 mOsm]). via a micropipette (Table 3). The micropipette was positioned by a micromanipulator (SM 5-9, Luigs & Neumann, Germany) to attach the cell. The pipette resistance was controlled by a patch clamp amplifier (EPC9, HEKA, Germany).

Table 3. Program for pulling cell-attached recording micropipettes.
Sutter P-97. Micropipettes were fabricated from borosilicate glass (GB150F-8P, 0.86 x 1.50 x 80 mm, Science Products GmbH, Germany) with a microelectrode puller (Sutter Instruments Co., USA).

Line	***Heat***	***Pull***	***Velocity***	***Delay***
1	RAMP		21	1
2	RAMP		21	1
3	RAMP-20		21	1
4	RAMP-20		18	1
5	RAMP	27	17	1

After the cell was labelled sufficiently, which was checked by a bright fluorescence and a visible axon origin, hybrid voltage sensor imaging (hVOS; Chanda et al., 2005) was performed. HVOS makes use of the Förster resonance energy transfer (FRET). In this case, DiO functions as electron donor and DPA as electron acceptor. DiO was illuminated with an LED with a peak wavelength of 457 nm (LZ4-00B208, LED Engin, USA). The energy transfer from the electron donor to the electron acceptor results in a quenching of brightness that was detectable through a CCD camera system (NeuroCCD-SM256, RedShirtImaging, USA; frame rate of 2 kHz at 80 x 80 pixel resolution with Neuroplex software, version 9.3.0, RedShirtImaging, LLC, Georgia, USA).

DPA moves in the membrane in dependence of the membrane potential. Depolarization leads to a physical approach of DPA to the DiO that result in a higher quenching of the signal. HVOS has a high temporal fidelity and, thus, can reflect action potentials (Chanda et al., 2005; Voll, 2015; D. Wang, Zhang, Chanda, & Jackson, 2010). Using this process provides the ability to measure changes in membrane potential at different loci, and thus the spread of the signal at a high temporal resolution.

Stimulation protocol

Shepherd's crook neurons receive input from retinal ganglion cells and likely from terminals in deeper layers. The visual and auditory signal were mimicked by positioning two stimulation electrodes in layers 2 to 4 (activation of the visual input to the optic tectum) and layer 13 (activation of the auditory input to the optic tectum). The stimulation electrodes were individually or simultaneously triggered. Each stimulus was bipolar with a stimulus length of 0.5 ms (250 µs

negative followed by 250 µs positive current flow) and a stimulus strength between 50 and 150 µA depending on the excitability of the recorded cell. Three stimuli with 200 ms interstimulus time were presented three times with 20s intervals. Stimuli were controlled via an analogue output module of the Neuroplex software and generated by an isolated pulse stimulator (model 2100, A-M Systems, USA).

Data analysis in hybrid voltage sensor imaging experiments

Data acquisition was controlled and preprocessed by the Neuroplex software. To analyze the signal propagation in SCNs data were processed with a custom-written script (Figure 3) based on a data analysis procedure described by Hochbaum et al. (2014). First, data were imported to MATLAB. The trigger time points were detected, and data with a high level of noise was removed. A high noise level was usually caused by moving particles or underexposed parts of the image that did not contain information. Afterwards, data was high-pass filtered by a fast Fourier transformation (10 Hz) and a 3-D Kernel. For further analyzing, the data points were broken down into segments according to the stimulation times, and a specific point on the labeled cell was selected. At this image point the recorded action potentials were analyzed referring to the spike form, latency, and number of action potentials. Based on the recorded signal form a normalized, 10-fold oversampled template was generated and a cross correlation over all recording traces performed to detect the occurrence of action potentials and their exact time point. On the prelabeled neuron three points were marked (one on the primary dendrite close to the branch of the axon from the primary dendrite, and two on the soma -one at the transition from the primary dendrite to the soma, and the other at the transition from the soma to the basal dendrite) and the signal at this specific position plotted against time. Using this information, it was possible to visualize the signal propagation in the region of interest by creating short videos. The data were statistically analyzed in MATLAB (MATLAB, version R2017a, MathWorks®) using the Kruskal-Wallis test.

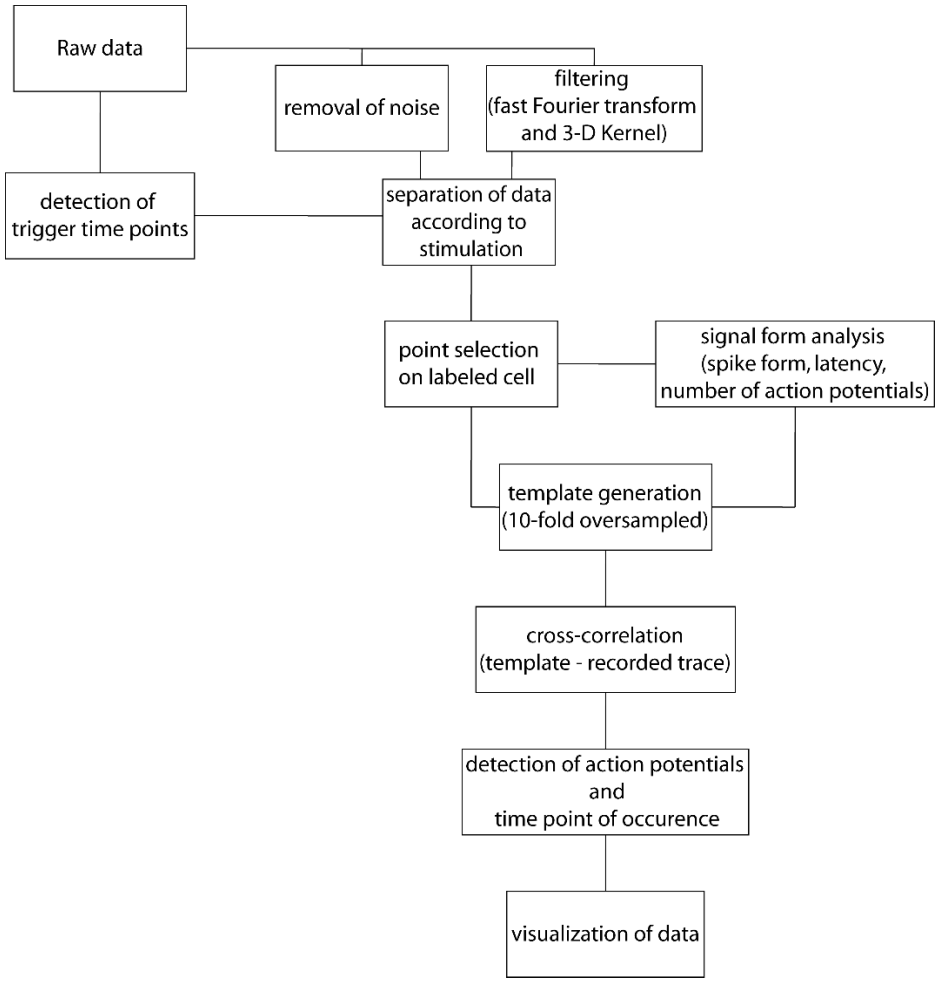

Figure 3. Flowchart of data analysis in hybrid voltage sensor imaging.
The raw data acquired in the hybrid voltage sensor imaging experiments were processed with a custom-written script in MATLAB based on the data analysis procedure previously described by Hochbaum et al. (2014).

Plasmid construction, plasmid amplification and plasmid transfection in chicken embryos for GFP expression in layer 10 neurons

Amplification of plasmid encoding a farnesylated GFP under the control of a CMV promoter (pAcGFP)

Glycerol stocks, which contained bacteria with inserted pAcGFP plasmids, were incubated in bacterial growth medium (LB medium) overnight at room temperature. Plasmid containing bacteria were selected by their ampicillin resistance. The plasmid amplification followed the protocol 'Plasmid DNA purification' of Macherey-Nagel Nucleo Bond ® Xtra Midi/Maxi for maxi preparation. After the plasmid amplification the isolated DNA was dissolved in sterile H_2O. To guarantee a highly purified DNA solution an additional purification step (containing Phenol/Chloroform/Isoamylalcohol [25:24:1] was performed. The DNA concentration was measured by a Nanodrop (plasmid concentration of current stock: 2.86 µg/µl). The sequence is shown in Figure 4A.

Amplification of plasmid encoding a cytosolic GFP under the control of a β-actin promoter (pβactineGFP)

For the amplification of a cytosolic GFP-expressing plasmid, *E. coli* DH 10b cells were transfected with a GFP encoding plasmid in a Multiporator (Eppendorf, settings: current 2500 V, pulse length 5 ms). The transfected cells were transferred to 1 ml LB medium and incubated for 30 min on a shaker (220 rpm) at room temperature. After incubation, the cell suspension was streaked on two agar plates and transfected cells were selected by their ampicillin resistance. The agar plates were incubated overnight at 37.5 °C before colonies were picked. Picked colonies were added again to LB medium containing ampicillin and incubated overnight at room temperature on a shaker (220 rpm). Further plasmid amplification followed the procedure

described under ‘Amplification of plasmid encoding a farnesylated GFP under the control of a CMV promoter (pAcGFP)’. The sequence is shown in Figure 4B.

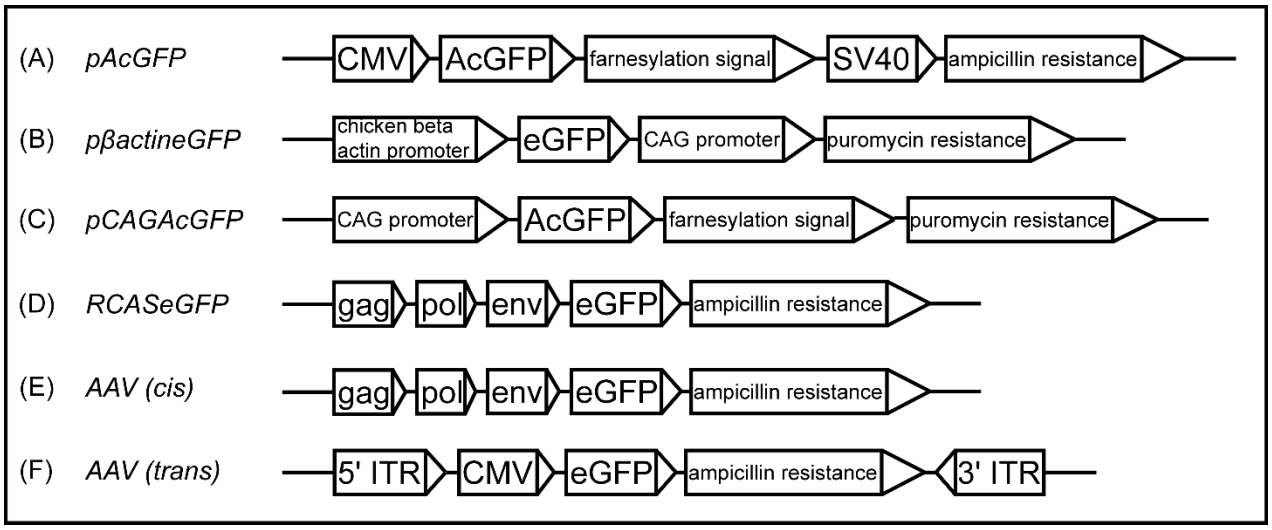

Figure 4. Sequence of GFP expressing plasmid.
(A) pAcGFP. The plasmid contains a CMV promotor, a farnesylation signal, a GFP, and an ampicillin resistance. The length of the whole plasmid sequence is 5865 bp. (B) pβactineGFP. The plasmid contains a cytosolic GFP, a chicken beta actin promotor, a CAG promotor and a puromycin resistance. The length of the whole plasmid sequence is 8982 bp. (C) pCAGAcGFP. The plasmid contains a CAG promoter, a GFP, a farnesylation signal, and an ampicillin resistance. The length of the whole plasmid sequence is 5865 bp. (D) RCASeGFP. The vector contains a CAG promoter, a cytosolic GFP, and an ampicillin resistance. The length of the whole vector sequence is 12369 bp. (E) AAV (cis). The vector contains cap and rep sequences, a cytosolic GFP, and an ampicillin resistance. The length of the whole vector sequence is 6548 bp. (F) AAV (trans). The vector contains a 5’ inverted terminal repeat (5’ITR), a CMV promoter, a cytosolic GFP, an ampicillin resistance, and a 3’ inverted terminal repeat (3’ITR). The length of the whole vector sequence is 7409 bp.

Construction of plasmid encoding a farnesylated GFP under the control of a CAG promoter (pCAGAcGFP)

For plasmid construction I started a PCR with primers designed to amplify GFP from a commercially available plasmid. Another plasmid with a CAG promoter was digested with EcoR1 and Not1. The PCR product and the digested plasmid was loaded on a 0.8 % agarose gel and the DNA fragments were separated by electrophorese according to their size, the required DNA bands were purified (Quiagen, GmbH Germany) and the concentration measured (Nanodrop®). The GFP product had a concentration of 107.4 ng/µl and the CAG product had a concentration of 56.7 ng/µl. To construct the desired plasmid a Gibson kit were used (Gibson Assembly®

Cloning Kit, New England Biolabs). After incubating the transfected cells overnight, four clones (concentration clone #1 385.9 ng/µl, clone #2 470.2 ng/µl, clone #3 289.9 ng/µl, clone #4 384.5 ng/µl; measured with Nanodrop®) were picked for a mini preparation (Promega GmbH, Germany). As clone #2 had the greatest profit, this clone was sequenced and used for further cell transfection. After electroporation of DT40 cells with clone #2 (electroporation parameter: 250 V, 125 ms, 8 times), cells were incubated at 37 °C for 48 h. The final concentration of the plasmid was 263 ng/µl. As this concentration was too low for in ovo transfection, the DNA was precipitated two times to reach a final concentration of 893 ng/µl. The plasmid solution was stored at -20 °C until use. The sequence is shown in Figure 4C.

Transfection and *in ovo* electroporation

In ovo electroporation of chicken embryos were performed according to published protocols (e.g. Nakamura & Funahashi, 2001; Nakamura, Watanabe, & Funahashi, 2000; Weigel, Flisikowska, Schnieke, & Luksch, 2014). Briefly, fertilized eggs of the White Leghorn chicken were incubated in a breeder (3000-D, Brutmaschinen-Janeschitz GmbH, Germany) for 46 hrs at 37.8 °C and 50 % humidity. After this incubation time the eggs attained HH stage 11 to 12 according to Hamburger and Hamilton (1951). 2 ml of albumin were removed with a syringe, and the eggs were opened to get access to the embryo through a small hole (Figure 5A). Different GFP-containing plasmids (pAcGFP, pβActin_eGFP, pCAGGFP, RCAS) were injected with a small injection glass capillary (Figure 5B, Table 5, borosilicate glass, GB100-8P, 0.58 x 1.00 x 0.80 mm, Science Products GmbH, Germany) into the lumen of the second brain vesicle. Gold-coated electrodes were placed along the second brain vesicle (Figure 5C, Genetrodes, 45-0115, BTX, Harvard Apparatus Inc., MA, USA), and the brain was electroporated (5 pulses, 50ms duration, 25 Volt, 1 Hz; Grass S48 stimulator, Medical Instruments, USA). To compensate the removal of albumen and to cool the embryo, 2 ml of ‘chicken ringer’ were added to the egg (150 mM NaCl, 5.4 mM KCl, 2.2 mM $CaCl_2$, and 2.4 mM $NaHCO_3$). After resealing the egg with adhesive tape, the eggs were incubated under the same conditions until preparation at E18 to E21. For analyzing the expression pattern of different plasmids and different transfection days, the whole brain was isolated and transferred to 4 % PFA. For imaging the signal propagation in specific neuronal cells in layer 10, the brain was isolated and sectioned as described in the section ‘Slice preparation’.

Table 4. Parameters for pulling of transfection pipettes.
Pipettes were fabricated from borosilicate glass (GB100-8P, 0.58 x 1.00 x 0.80, Science Products GmbH, Germany) with a microelectrode puller (Sutter P-97, Sutter Instruments Co., USA).

Parameter	*Pressure*	*Heat*	*Pull*	*Velocity*	*Time/Delay*
Value	500	491	120	40	165

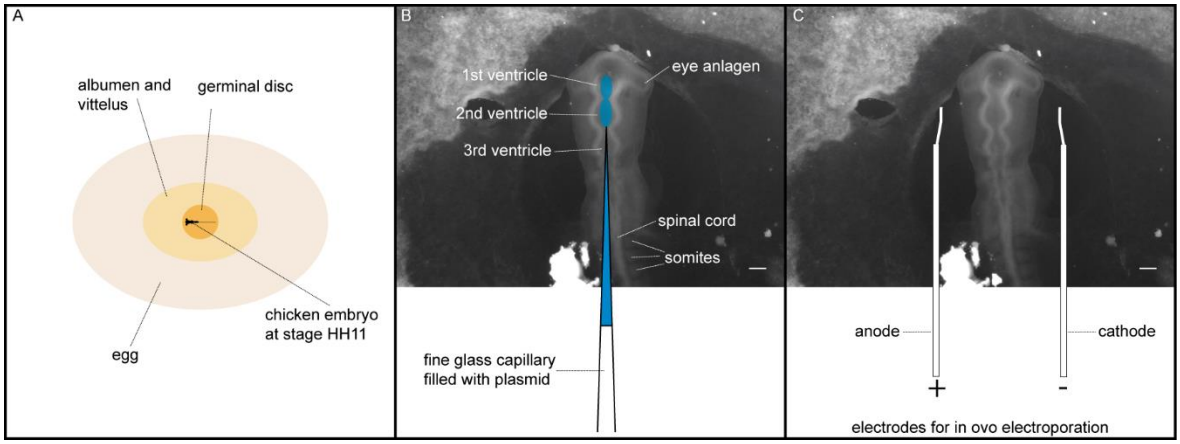

Figure 5. Transfection and electroporation of chicken embryo at HH11.
(A) Schematic overview of a chicken embryo at stage HH11. 46 hours before transfection and *in ovo* electroporation the egg was placed in a breeding incubator without movement. To get access to the embryo, a small hole was cut in the top of the egg. (B) Schematic view of an embryo at stage HH11 after plasmid/viral vector injection in the second vesicle. (C) Schemata of the placement of the electroporation electrodes. Only the tip is non-insulated to help establishing an electric field during current pulses.

To increase the transfection efficiency and survival of the embryo several parameters (impact of storage period before incubation, impact of antibiotics, impact of disinfection, of the egg shell, impact of stronger disinfectant) were tested and compared in terms of lower infection rate with viruses and bacteria.

Viral vectors

In addition to in ovo electroporation, embryos at HH 11 were transfected with adeno-associated viral vectors (Figure 4 E and F, rAAVs) and RCAS system (Figure 4D, Replication-Competent ASLV long terminal repeat [LTR] with a splice acceptor). The rAAVs contained the ITR sequence of serotype 2 combined with the capsid sequence of different serotypes (#1 titer $1.24x10^{13}$, #5 titer $4.21x10^{13}$, #8 titer $3.34x10^{13}$, and #9 titer $3.6x10^{13}$). The injection of rAAVs followed the

same procedure as described in section ‘Transfection and *in ovo* electroporation’ but without the electroporation step. Two different titers (#titer1 $1x10^9$ and #titer2 $1x10^7$) of rAAVs were injected.

Effect of missing retinal innervation on the development of Shepherd's crook neurons

Enucleation

Pre-incubation and egg opening were done following the description in the section 'Transfection and *in ovo* electroporation'. "At HH11, the eye anlagen are clearly visible on both sides of the first vesicle (Figure 6B). One eye *anlagen* was unilaterally removed with a fine, etched tungsten electrode (Figure 6A and 6C). After enucleation, the egg was resealed with tape and incubated until stage E19 to E21 for slice preparation."[19]

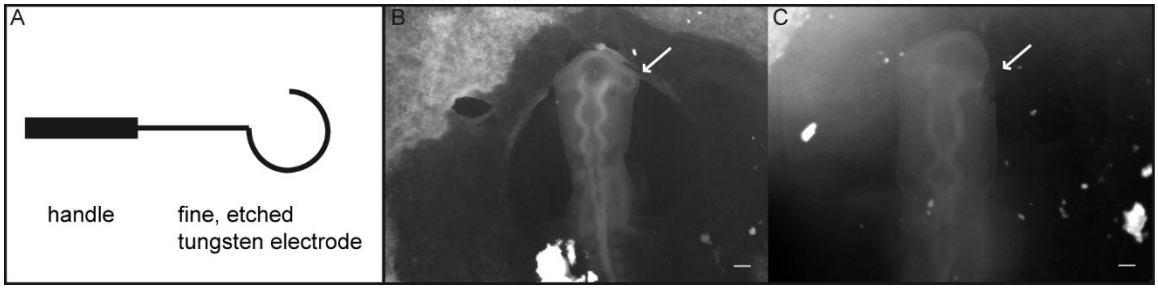

Figure 6. Early eye removal in chicken embryos at HH11.
(A) Custom made tool from a fine, etched tungsten electrode to unilateraly remove the eye anlagen at stage HH11. (B) A chicken embryo at stage HH11. The white arrow indicates the right eye anlagen. (C) A chicken embryo at stage HH11 after removal of the right eye anlagen (white arrow). Scale bar in (B) and (C): 200 µm. Figure reproduce from Lischka, Yan, Weigel, & Luksch, 2018, with permission from the publisher.

Histology and immunohistochemistry

In order to study changes in the morphology of SCNs, they were retrogradely labelled as described earlier (Material and Methods section, chapter 'Expression patterns of structural proteins and ion channels in Shepherd's crook neurons', paragraph 'Tracer injections'). "Here, biocytin (biocytin hydrochloride, #B1758, Sigma-Aldrich, Steinheim, Germany) was injected in three separated sites of the IMC in 1000 µm thick slices of 12 individual embryos. After a transport time of 4 hrs, which allowed retrograde tracer transportation, and fixation in 4 % PFA

[19] Lischka, Yan, Weigel, & Luksch, 2018

for 2 hrs, the slices were resectioned to 40 µm sections on a microtome (Microm HM440E, GMI, USA). Labeled structures were visualized with a 3'3-Diaminobenzidine protocol (DAB; #102924, Merck, Darmstadt, Germany) combined with tyramide signal amplification (TSA; biotin-tyramide, #LS-3500, Iris Biotech GmbH, Marktredwitz, Germany) as described previously (Krabichler et al., 2017)."[20] Briefly, the sections were incubated for 12 min in 0.5 % H_2O_2 (diluted in 75 % methanol) at room temperature to eliminate the endogenous peroxidases. After some washing steps, the sections were transferred into the avidin-biotin-complex solution and incubated for 1 hr at room temperature. For visualization of fine structures, the signal was amplified by the introduction of an additional biotin-tyramide complex which increased the available binding sites for avidin. The oxidation of DAB with 1 % H_2O_2 lasted for 3 min before several washing steps were performed. "The sections were mounted onto gelatin-subbed glass slides, dried, and counterstained with neutral red for further analyzing."[21]

Data analysis in enucleation experiments

"The TeO and single neurons were photographed with an Olympus BX63 microscope with attached digital cameras (DP26 for bright field, XM10 for epifluorescence). The thickness of the TeO and several parameters of SCN morphology were measured with the CellSensDimension software (version 1.7, Olympus, Hamburg, Germany). As the thickness of the TeO varies in dorsoventral direction and across animals, I compared enucleated and control hemispheres of the same animals (N = 11). To account for intratectal variances I measured at four positions per slice between stages E19 and E21. Fifteen slices of eleven individuals were analyzed. The reconstruction of single SCNs were done semi-automatically with Neuromantic software (Version 1.7.5, Myatt et al., 2012). All data were tested for normal distribution and statistical significance in SigmaPlot (software version 11.0.0, Systat Software GmbH, USA) using the Kolmogorov-Smirnov test followed by the Mann-Whitney rank sum test. Data are shown as median and average of the absolute deviation from the median."[22]

[20] Lischka, Yan, Weigel, & Luksch, 2018
[21] Lischka, Yan, Weigel, & Luksch, 2018
[22] Lischka, Yan, Weigel, & Luksch, 2018

Results

The paragraph ‘Morphology and expression patterns of structural proteins and ion channels of Shepherd’s crook neurons’ of the Results is modified from the Results section that corresponds to the following publication:

“Expression patterns of ion channels and structural proteins in a multimodal cell type of the avian optic tectum” (Lischka, Ladel et al., 2018)

The article is published in The Journal of Comparative Neurology, which permits authors the reproduction of published articles for dissertations without charge or further license.

- -

The paragraph ‘Influence of missing retinal innervation on development of Shepherd’s crook neurons’ is modified from the Results sections that corresponds to the following publication:

“Effects of early eye removal on the morphology of a multisensory neuron in the chicken optic tectum” (Lischka, Yan et al., 2018)

The article is published in Brain Research, which permits authors the reproduction of published articles for dissertations without charge for further license.

The Shepherd´s crook neurons (SCNs) are candidate cells that likely perform multimodal integration in the chicken optic tectum. However, not much was known about ion channels expressed in these cells, the fine anatomy and their physiology. Thus, I studied the neuronal anatomy and electrophysiological responses to various stimulation. The aim was to find evidence for multimodal integration on the cellular level. I analyzed the molecular composition of different compartments in SCNs with immunocytochemistry. Based on these findings I implemented a multi-compartment model. As I was also interested in the signal propagation and the ability of SCNs to integrate two different sensory input signals, I performed hybrid voltage sensor imaging experiments with prelabeled SCNs (plasmid transfection by *in ovo*

electroporation or single cell labelling). In the following sections, the results of these projects are shown.

Expression patterns of structural proteins and ion channels of Shepherd’s crook neurons

The first aim of this project was the identification of the axon and the axon initial segment to determine the site of action potential generation in Shepherd’s crook neurons. Additionally, I was interested in the expression patterns of different voltage-gated ion channels. “First, I prelabeled SCN neurons to show their morphology (Figure 7A and E) and to allocate antibody-labeling patterns to subcellular regions. The morphology of Shepherd’s crook neurons was first described by Ramón y Cajal (1909). The somata are located in the intermediate layer 10 and are elongated in shape (21.85 µm ± 10.23 µm; n = 52; Figure 7F) with an apical and a basal dendrite. The white arrows in Figure 7B show the proposed signal flow in SCNs as proposed by Ramón y Cajal (1909). The apical dendrite splits in two or more main branches, which further branch into fine dendritic endings. The apical dendrite extends to the retinorecipient layers (Figure 7C; layer 2 to 7), the basal dendrite extends into the deeper layers (Figure 7D; layer 11 to 13). The axon branches from the apical dendrite at 79.09 µm ± 21.49 µm (Figure 7F, n = 52) and course perpendicularly through the deeper layers to the isthmic nuclei with terminals in each of the three nuclei (IMC, IPC, SLu) (Garrido-Charad et al., 2018; Y. Wang et al., 2006).

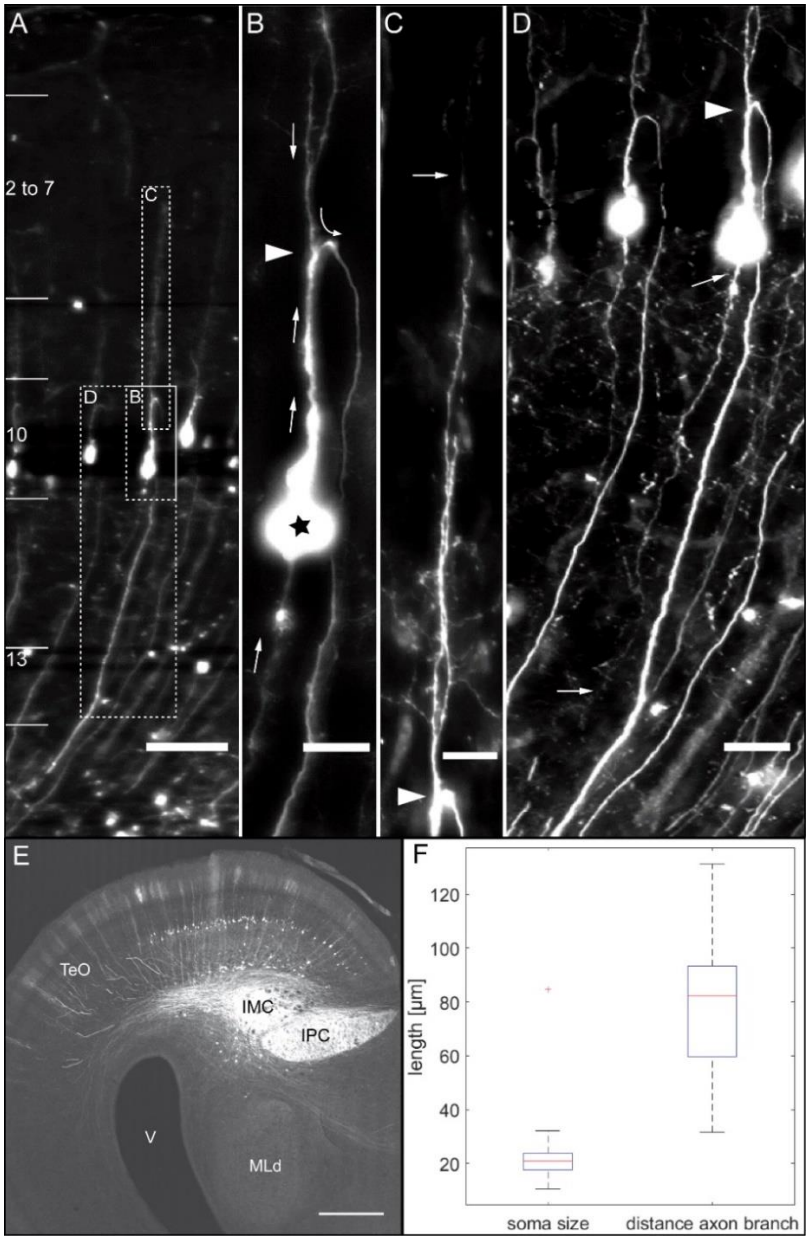

Figure 7. Morphology of a Shepherd's crook neuron.
(A) Overview of SCN in radial orientation in the TeO. (B) The soma is located in layer 10. The axon branches from the apical dendrite. Arrowhead point to the axon branch. Arrows indicate the suggested signal flow. (C) The apical dendrite extends toward the retinorecipient layers (2 to 5 and 7). Arrowheads show the beginning of the apical dendrite in layer 10 and the terminal endings in layer 2. (D) The basal dendrite projects to the deeper layers. Arrowheads indicate the beginning of the basal dendrite in layer 10 and the terminal endings in layer 13. (E) Overview of the TeO. Many radially oriented Shepherd's crook neurons were retrogradely labeled after an injection of a fluorescent dye in the IMC but also axons of IPC neurons. Detailed cell morphology is shown in (A) to (D). (F) Diagram indicates the soma length and the distance between soma and axon branch. The y-axis shows the length in micrometer [µm] (n=52). TeO: optic tectum. V: ventricle. IMC: *nucleus isthmi pars magnocellularis*. IPC: *nucleus isthmi pars parvocellularis*. MLd: *nucleus mesencephalis lateralis pars dorsalis*. Scale bar for (A) 50 µm. Scale bar in (B) to (D) 20 µm. Scale bar in (E) 500 µm. Figure reproduced from Lischka, Ladel, Luksch, & Weigel, 2018, with permission from the publisher.

To identify the different functional subcellular compartments, I used three different markers for structural proteins (NF200, Ankyrin G, and myelin) and four different markers for ion channels ($PanNa_v$, $Na_v1.6$, $Na_v1.2$, and $K_v3.1b$). I conducted western blot analyses (Figure 8) to test the antibody specificity in the chicken midbrain unless the specificity was already reported in the literature. The specificity of the $K_v3.1$ epitope (92 kDa) was described by Parameshwaran, Carr, and Perney ((2001); see also (Kuenzel et al., 2009; Y. Wang et al., 2006).

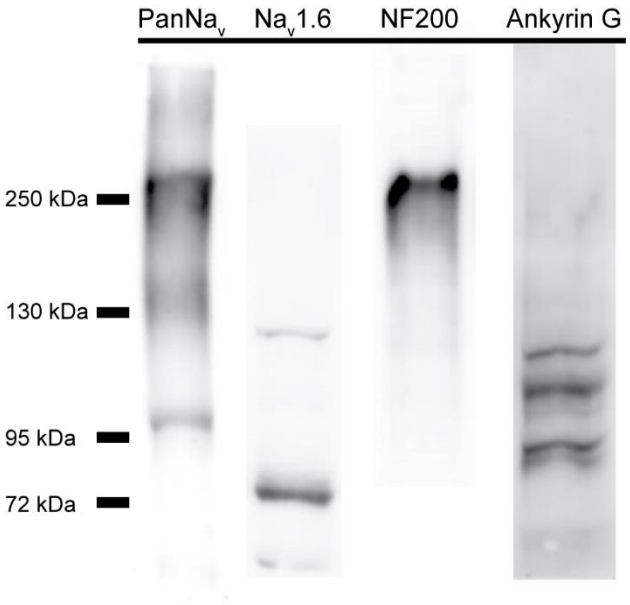

Figure 8. Antibody specificity of sodium channels and structural proteins
The specificity of PanNav, Nav1.6, NF200, and Ankyrin G were tested by Western Blot analyses on chicken midbrain tissue. Figure reproduced from Lischka, Ladel, Luksch, & Weigel, 2018, with permission from the publisher.

For the sodium channels $Na_v1.6$ and $PanNa_v$, the antibody specificity had not been tested so far in chicken. In other studies, the proteins were detected in rat or mouse brain lysates (Anderson, Hawkins, Thompson, Kearney, & George, 2017). For $Na_v1.6$ a single band with 225 kDa, and for $PanNa_v$ a single band with 250 kDa was observed (Caldwell, Schaller, Lasher, Peles, & Levinson, 2000). In chicken midbrain tissue, I detected two proteins with 130 and 70 kDa for $Na_v1.6$ and three proteins with 250, 130, and 110 kDa for $PanNa_v$ (Figure 8). The antibody against neurofilament 200 labels a protein of 200 kDa in the bovine spinal cord (ref. Sigma Aldrich). In chicken midbrain tissue, this antibody bound specifically to a band of 250 kDa (Figure 8). The Ankyrin G specificity was confirmed by a single band of 190 kDa on a mouse

brain tissue extract (ref. Santa Cruz Biotechnology). In chicken midbrain tissue, this antibody bound to several proteins of the size between 115 and 90 kDa (Figure 8)."[23] These bands of lower molecular weight may occur due to the digestion of the target protein because of the lack of proteinase inhibitors in the sample buffer.

[23] Lischka, Ladel, Luksch, & Weigel, 2018

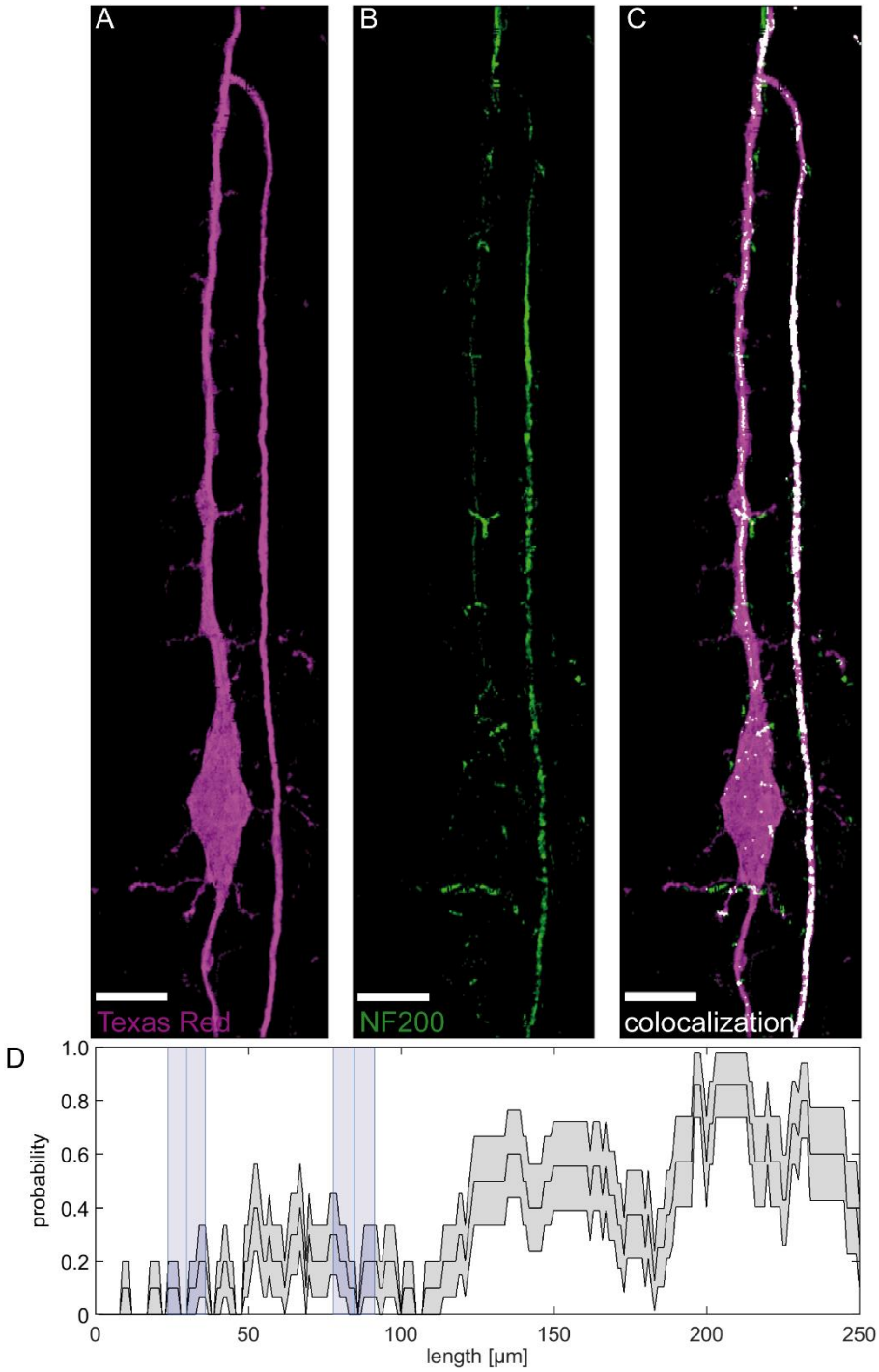

Figure 9. Expression pattern of the structural protein neurofilament 200.
(A) Retrogradely labeled SCN. (B) Expression pattern of neurofilament 200. (C) Overlay of neurofilament 200 on the labeled SCN. (D) Diagram of the probability of neurofilament 200 expression over the cell. n=17. x-axis indicates the length in micrometer [µm]. y-axis indicates the probability that neurofilament 200 is expressed. The analysis included the soma, the primary dendrite and the axon (defined as region of interest). The first blue bar indicates the mean soma size; the second blue bar indicates the mean axon origin. Error bars show the standard deviation. Scale bar in (A) to (C): 10 µm. Figure reproduced from Lischka, Ladel, Luksch, & Weigel, 2018, with permission from the publisher.

"Retrogradely labelled SCNs were analyzed in respect to the colocalization of expression patterns of different structural proteins. First, I labeled axonal structures with an antibody against the heavy chain of neurofilament (NF200). A strong immunoreaction with anti-neurofilament 200 was found on the axon that projects to the isthmic nuclei, and only a weak signal on the rest of the soma and the primary dendrite (Figure 9A–C). The expression pattern of NF200 starts approximately 50 µm after the axon branches from the apical dendrite (Figure 9D).

To identify the site of action potential generation in SCNs, I used an antibody against Ankyrin G. The expression of this protein is mainly limited to the beginning of the axon from the dendritic branching point, which extends approximately 50 µm along the axon (Figure 10A–C). This site is likely to be the action potential generation site (AIS) in SCNs (Figure 10D). Only Ankyrin G is expressed in the AIS, while the expression of NF200 starts after the AIS. By using antibodies against distinct subtypes of voltage-gated sodium and potassium channels, the functional properties of each compartment were investigated.

I labeled the tissue with an antibody against an epitope of rat $Na_v1.1$ channel that is identical in all isoforms of Na_v1 in vertebrates. The $PanNa_v$ expression pattern showed that sodium channels are densely expressed on the axon after the axon branch (Figure 11A–C). This isoform is also present at a lower density on the soma, the primary dendrite and the AIS (Figure 11D). Based on the expression pattern of $PanNa_v$, the question arose whether the expression of voltage-gated sodium channels is driven by one dominant sodium channel subtype. Thus, I used an antibody against the voltage-gated sodium channel subtype $Na_v1.6$. In SCNs, $Na_v1.6$ is strongly expressed on the axon after the axon origin. A weaker expression is also visible at the soma, the primary dendrite and the AIS. The tube-like structure of $Na_v1.6$ expression indicates that the sodium channels are located in the cell membrane of SCNs (Figure 11).

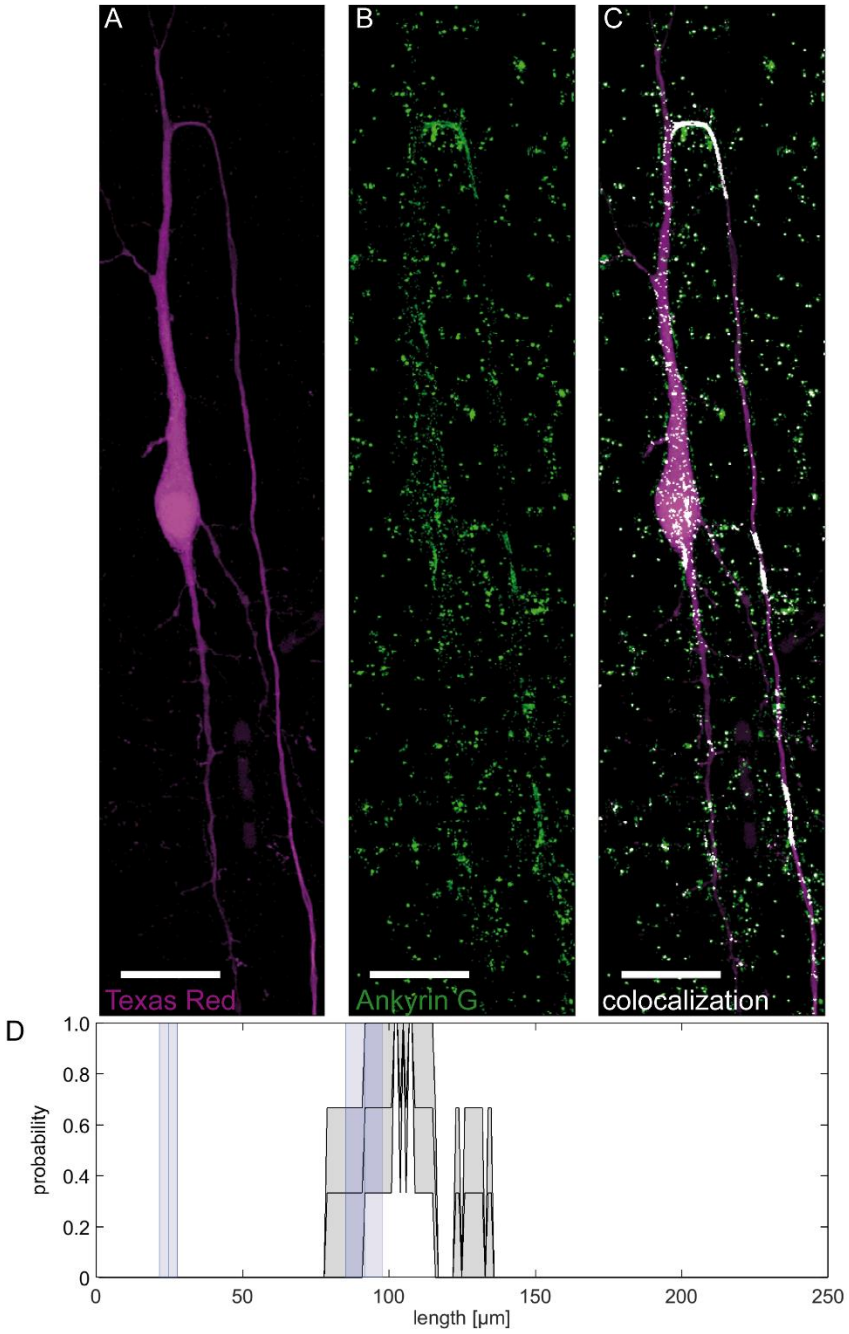

Figure 10. Expression pattern of the structural protein Ankyrin G.
(a) Retrogradely labeled SCN. (B) Expression pattern of Ankyrin G. (C) Overlay of Ankyrin G on the labeled SCN. (D) Diagram of the probability of Ankyrin G expression over the cell. n=7. x-axis indicates the length in micrometer [µm]. y-axis indicates the probability that Ankyrin G is expressed. The analysis included the soma, the primary dendrite and the axon (defined as region of interest). The first blue bar indicates the mean soma size; the second blue bar indicates the mean axon origin. Error bars show the standard deviation. Scale bar in (A) to (C): 20 µm. Figure reproduced form Lischka, Ladel, Luksch, & Weigel, 2018, with permission form the publisher.

The expression pattern of the subtype $Na_v1.6$ is similar to the expression pattern of the $PanNa_v$ antibody (Figure 12D). Another antibody against the voltage-gated sodium channel subtype $Na_v1.2$ was also tested but did not show any labeling on SCNs (data not shown).

For generating action potentials, voltage-gated potassium channels are also required. Thus, immunohistochemical labeling of the subtype $K_v3.1b$ was performed (Figure 13A–C). The expression of the voltage-gated potassium channel subtype $K_v3.1b$ ranges from the part of the basal dendrites proximal to the soma, along the soma, the primary dendrite and the beginning of the axon branch (Figure 13D). The tube-like distribution of potassium channels confirmed the localization of the voltage-gated ion channel in the cell membrane as it was expected from the natural localization in neurons (Figure 13B).

As myelination enables high propagation velocities in neurons, I investigated the myelination of SCN with a marker that binds via lipophilic affiliation to the high lipophilic content of myelin in axonal sheaths. The myelination of axons starts in layer 10 approximately 300 µm after the axon branches from the apical dendrite. The expression continues to the isthmic nuclei, where the axon terminates (Figure 14).

In Figure 15, the distribution of the expression patterns of all proteins investigated in this study is summarized. The neuronal segment between the distal part of the soma until the beginning of the axon (approximately 250 µm away from the axon origin) was defined as region of interest and is represented by the x-axis of the diagram. The mean soma length (21 µm) and site of the axon branch (79 µm) are indicated by vertical bars. I clearly saw a specific distribution for each structural protein in the AIS and the axon, respectively. At the beginning of the axon branch only Ankyrin G (green line, 92–115 µm) is expressed. After the axon branching from the primary dendrite, the Ankyrin signal decreases and the Neurofilament 200 expression (blue line, after 124 µm until end of region of interest) increases. Considering the molecular distribution of the sodium and potassium ion channels, the voltage-gated sodium channels are highly expressed on the axon (after 68 µm until end of region of interest). A dense expression of $Na_v1.6$ (after 110 µm until end of region of interest) starts after the axon branch similar to the NF200 expression. Hence, the highest density of sodium channels is not colocalized with the AIS. Sodium channels also exist on the soma, the primary dendrite and the AIS but to a lower extend.

K_v3.1b (beginning of region of interest until 77 µm) is mostly expressed on the soma, the primary dendrite and the AIS."[24]

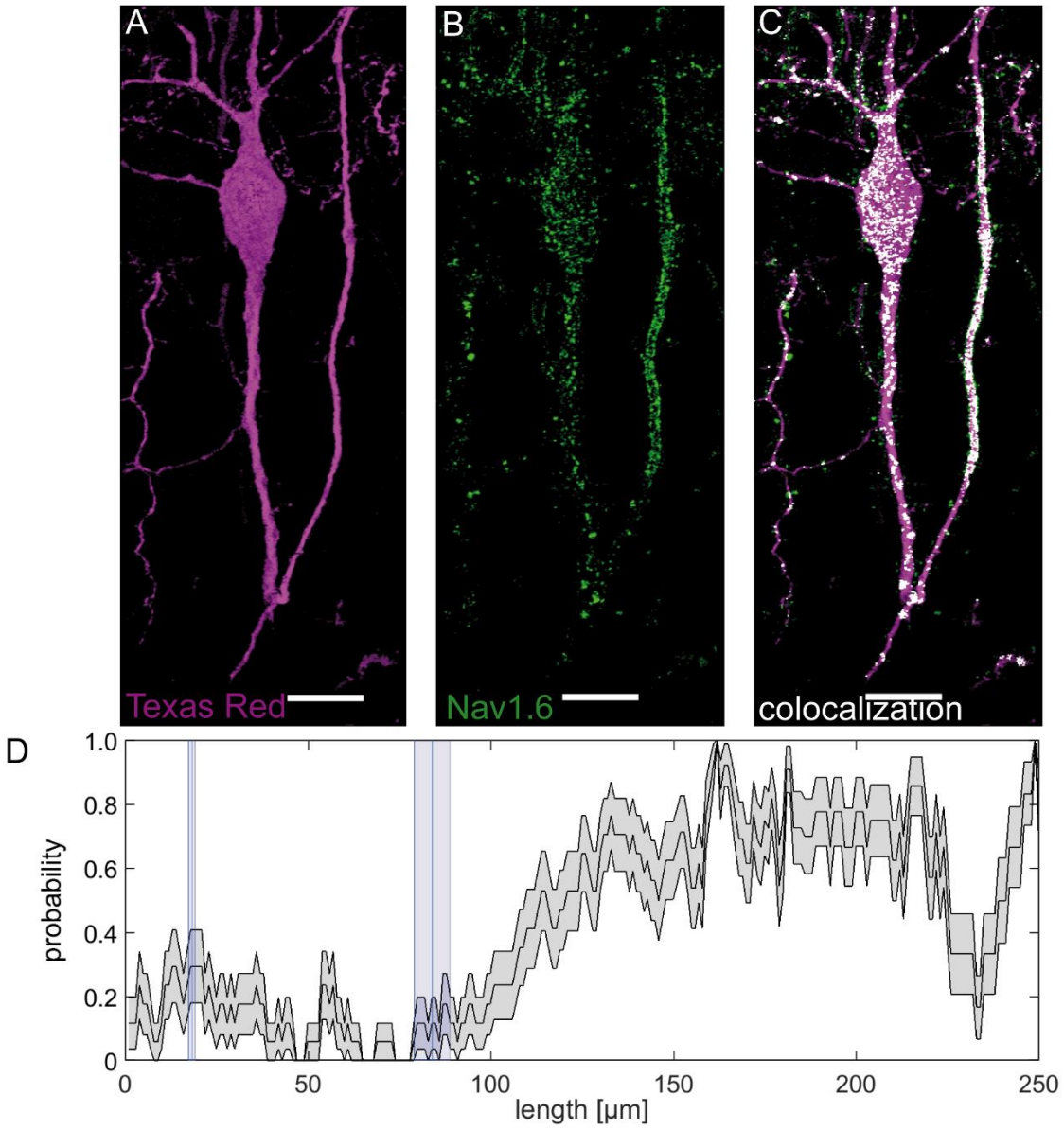

Figure 11. Expression pattern of the voltage-gated sodium channel subtype $Na_v1.6$.
(A) Retrogradely labeled SCN. (B) Expression pattern of the voltage-gated sodium channel subtype $Na_v1.6$. (C) Overlay of retrogradely labeled cells and $Na_v1.6$ channels on the somatodendritic regions, the primary dendrite, the axon initial segment and the axon. (D) Diagram of the probability of $Na_v1.6$ expression over the cell. n=29. x-axis indicates the length in micrometer [µm]. y-axis indicates the probability that $Na_v1.6$ is expressed. The analysis included the soma, the primary dendrite and the axon (defined as region of interest). The first blue bar indicates the mean soma size; the second blue bar indicates the mean axon origin. Error bars show the standard deviation. Scale bar in (A) to (C): 10 µm. Reproduced from Lischka, Ladel, Luksch, & Weigel, 2018, with permission from the publisher.

[24] Lischka, Ladel, Luksch, & Weigel, 2018

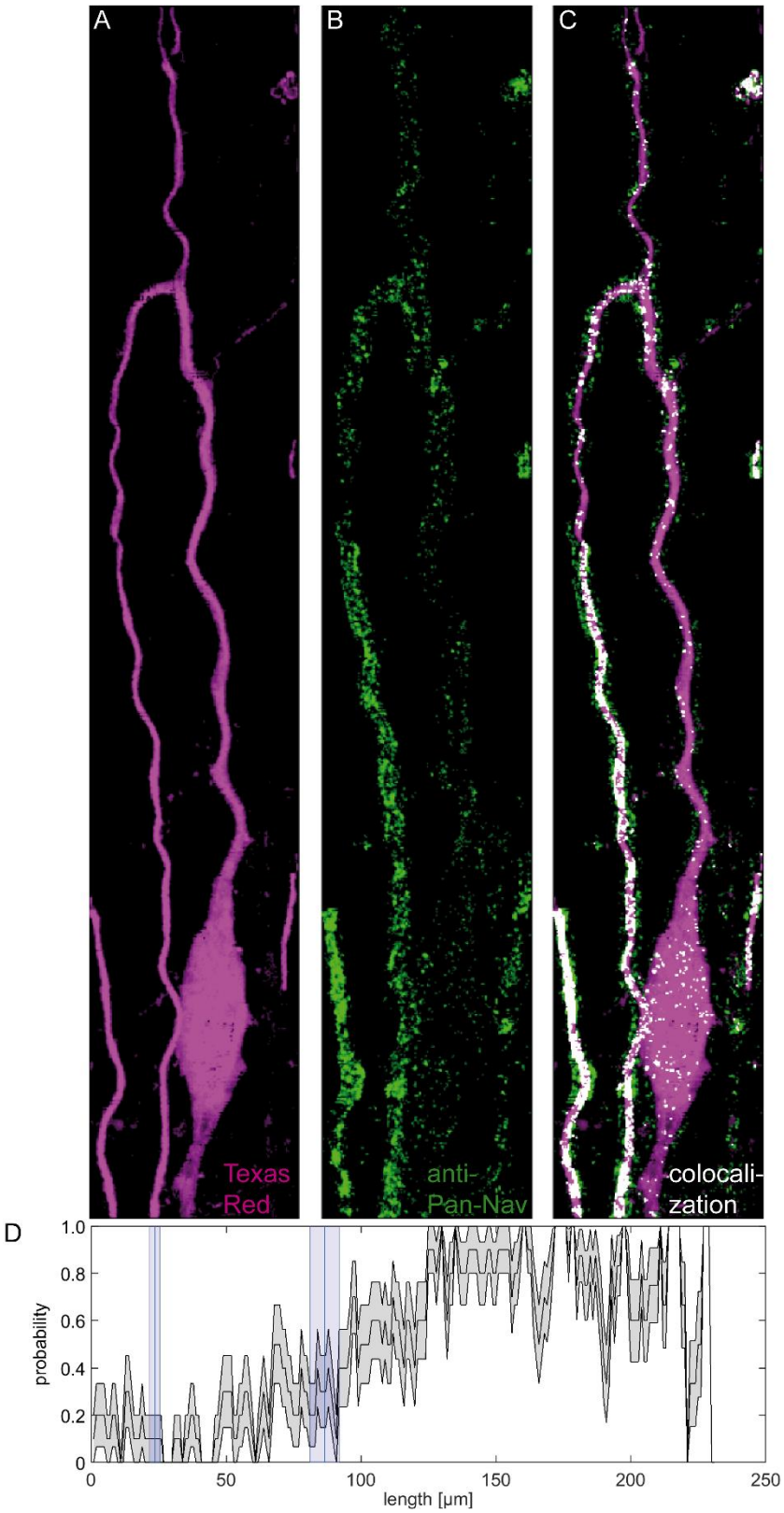

Figure 12. Expression pattern of the voltage-gated sodium channels PanNa$_v$.
(A) Retrogradely labeled Shepherd's crook neuron. Soma, primary dendrite and axon branch are shown. (B) Expression pattern of the voltage gated sodium channels. (C) Overlay of the retrogradely labeled SCN and the expression of PanNa$_v$. (D) Diagram of the probability of PanNa$_v$ expression over the cell. n=10. x-axis indicates the length in micrometer [µm]. y-axis indicates the probability that PanNa$_v$ is expressed. The analysis included the soma, the primary dendrite and the axon (defined as region of interest). The first blue bar indicates the mean soma size; the second blue bar indicates the mean axon origin. Error bars show the standard deviation. Scale bar in (A) to (C): 10 µm. Reproduced from Lischka, Ladel, Luksch, & Weigel, 2018, with permission from the publisher.

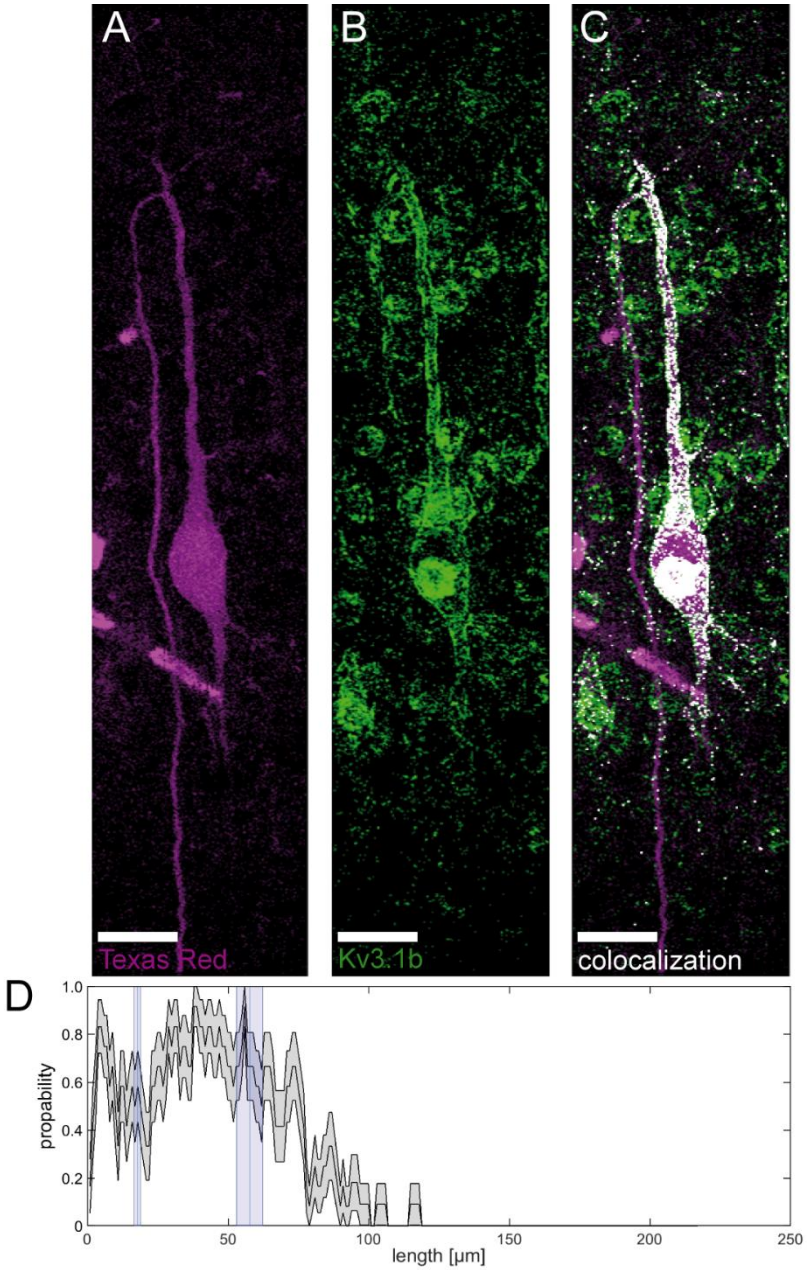

Figure 13. Expression pattern of the voltage-gated potassium channel subtype K_v3.1b.
(A) Retrogradely labeled SCN. Soma, primary dendrite and axon branch are shown. (B) Expression pattern of the potassium channel subtype K_v3.1b. (C) Colocalization of SCN and K_v3.1b. (D) Diagram of the probability of K_v3.1b expression over the cell. n=17. x-axis indicates the length in micrometer [µm]. y-axis indicates the probability that K_v3.1b is expressed. The analysis included the soma, the primary dendrite and the axon (defined as region of interest). The first blue bar indicates the mean soma size; the second blue bar indicates the mean axon origin. Error bars show the standard deviation. Scale bar (A) to (C): 20 µm. Reproduced from Lischka, Ladel, Luksch, & Weigel, 2018, with permission from the publisher.

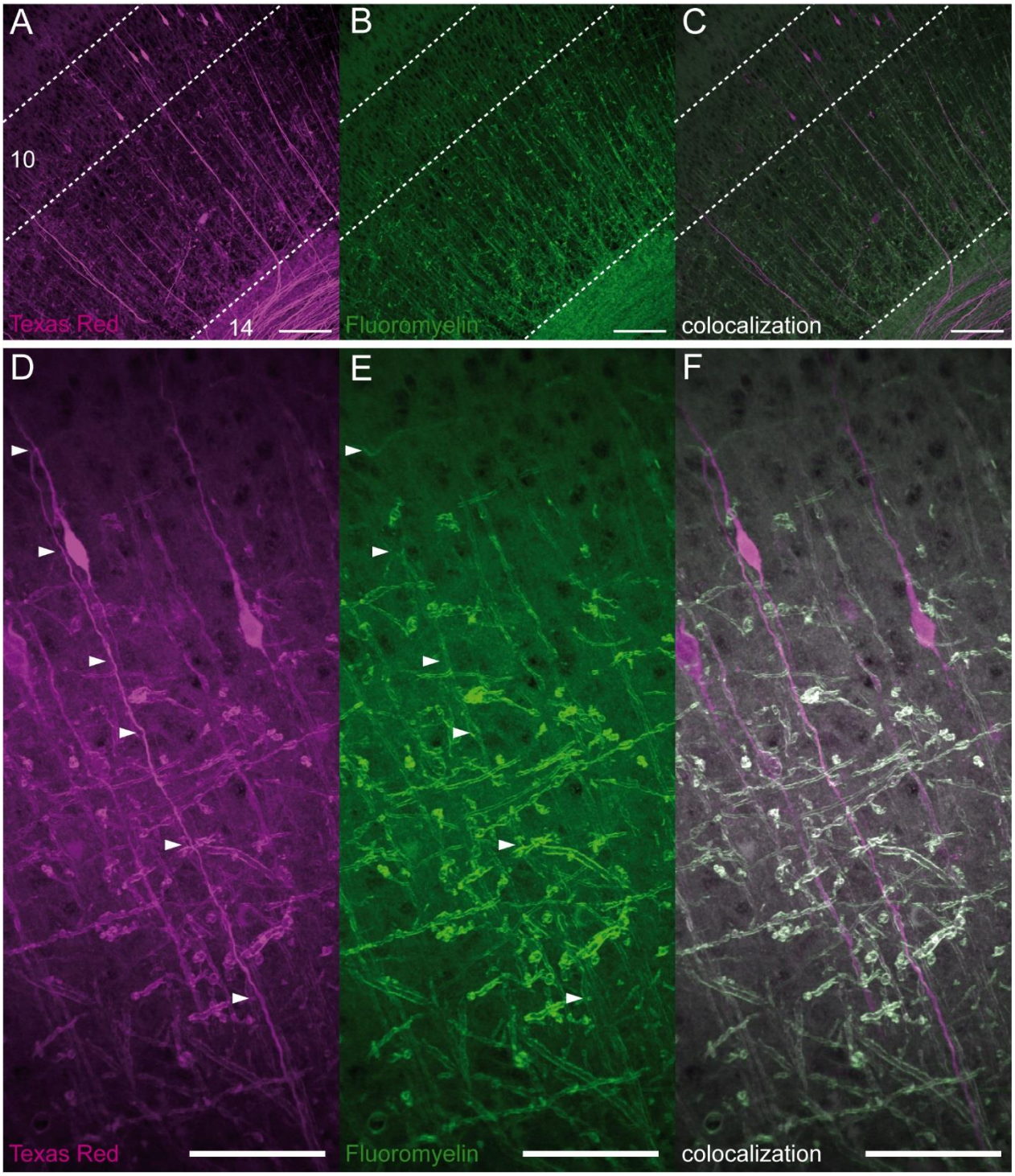

Figure 14. Myelination in the optic tectum.
(A) to (C) Overview of the TeO. Fluoromyelin continuously stains the myelinated axon of SCN from layer 10 to at least the output layer 14. (D) to (F) Detailed view of a SCN and its myelination. The white arrowheads indicate the axon in (D) and its myelination in (E). Scale bar for (A) to (C): 100 µm. Scale bar for (D) to (F): 100 µm. Reproduced from Lischka, Ladel, Luksch, & Weigel, 2018, with permission from the publisher.

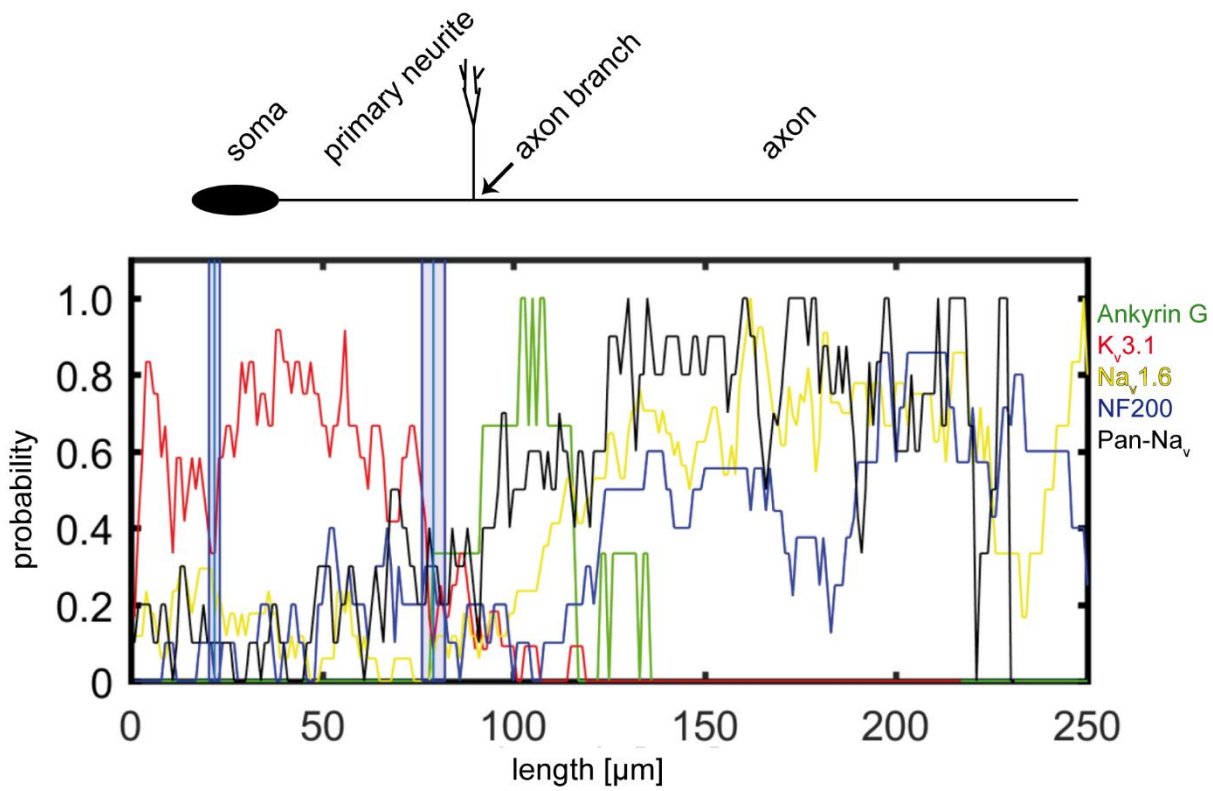

Figure 15. Distribution of the structural proteins NF200 and Ankyrin G and the voltage-gated sodium and potassium channels $Na_v1.6$, $K_v3.1b$, and PanNa_v.
The analysis includes the soma, the primary dendrite and the axon. The first blue bar indicates the mean soma size; the second blue bar indicates the mean axon origin. Red line: expression of Kv3.1b (n = 17). Yellow line: expression of Nav1.6 (n = 29). Blue line: expression pattern of NF200 (n = 14). Green line: expression pattern of Ankyrin G (n = 7). Black line: expression pattern of Pan-Nav (n = 10). Reproduced from Lischka, Ladel, Luksch, & Weigel, 2018, with permission from the publisher.

Multi-compartment model based on anatomical data

After identifying several expression patterns of structural proteins and ion channels, I implemented this information in a multi-compartment model of Shepherd's crook neurons in collaboration with Thomas Künzel, RWTH Aachen. The model consists of the following compartments: soma, primary dendrite (pNeurit), apical dendrite (aDend), basal dendrite (bDend), apical synapses (asyn), basal synapses (bsyn), axon initial segment (axonInit), and axon (node and internode). The schematic figure of the different expression patterns (Figure 16A) functioned as a template for the multi-compartment model (Figure 16B). The information of abundance of ion channels was derived from the respective antibody staining. Each compartment was characterized by its specific ion channel expression pattern. If information was missing, Hodgkin-Huxley like parameters were used. The active compartments are labeled in green in Figure 16B, while the passive compartments are shown in grey. The membrane voltage (V(rest)) was set to -50 mV, the membrane resistance (R(M)) to 394 MΩ, and the time constant (tau) to 28.9 ms. These values are based on physiological properties of SCNs (Voll, 2015). The end of the apical and basal dendrites functioned as stimulation sites. Here, a previous defined number of synapses were assumed to be active during stimulation. When the visual signal was mimicked, all synapses were allocated to the apical dendrite. When the auditory signal was mimicked, all synapses were allocated to the basal dendrite. During simultaneous activation synapses were uniformly distributed on the basal and apical dendrite. The multi-compartment model considered that the number of activated synapses during unimodal stimulation was equal to the number of activated synapses during bimodal stimulation.

In Figure 17A, examples for the three different stimulation types (auditory, visual, audiovisual) are shown. The activity was recorded at the soma and the axon and is indicated by green and red traces, respectively. Stimulating the model led to considerably higher activity recorded on the axon than on the soma (Figure 17A). Comparing the stimulation sites, apical synapses evoked more spikes recorded at the axon than basal synapses. In the example shown, activation of the basal synapses (auditory input) led to an action potential rate of 32 Hz (Figure 17A, lower diagram). An activation of the apical synapses (visual input) led to an action potential rate of 46 Hz (Figure 17A, middle diagram). Simultaneous stimulation of visual and auditory input regions generated the highest action potential rate (64 Hz, Figure 17A, upper diagram).

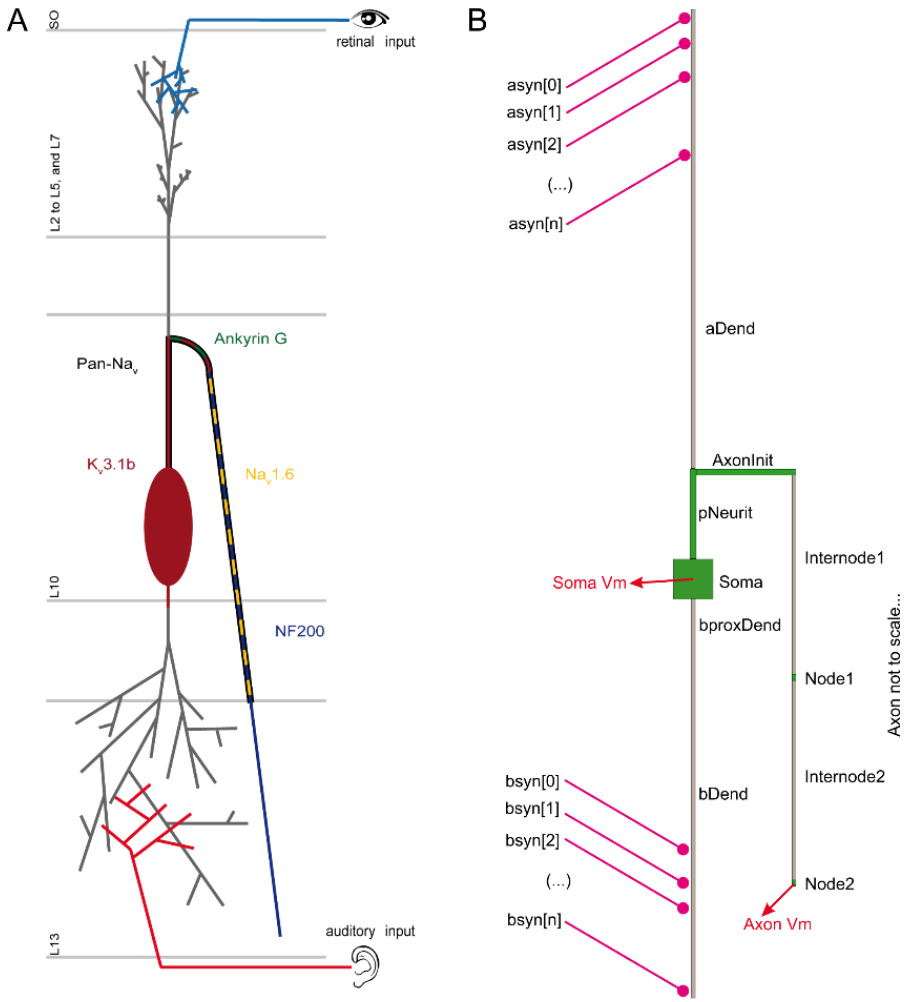

Figure 16. Multi-compartment model based on anatomical data.
(A) Schematic summary of expression patterns of ion channels and structural proteins in a multimodal cell type. The schemata of SCN show the location of soma and axon branch in terms of the layered structure of the TeO and the dendritic input sites of visual and auditory information. The same colors for every expression pattern are used as in Figure 15. SO: stratum opticum. L: layer. retinal input: visual input coming from the retinal ganglion cells. auditory input: terminals which ending in the deeper layers coming from the IC/FRLx. SO: stratum opticum. (B) The model contains six compartments: soma, primary dendrite (pNeurit), axon initial segment (AxonInit), axon (Node and Internode), apical dendrite (aDend), and basal dendrite (bDend), apical synapses (asyn), basal synapses (bsyn). Compartments which contain ion channels dynamics according to Hodgkin-Huxley are colorized green, passive compartments are shown in grey. Stimulation sites are apical and basal dendrites. Recording sites are soma and axon. Illustration in (A) is reproduced from Lischka, Ladel, Luksch, & Weigel, 2018, with permission from the publisher.

The three activation paradigms were repeated 100 times (Figure 17B). The spiking rates after 100 repetitions are highly different (Figure 17C). On the axon, the average action potential rate for double stimulation is 77 Hz, while the average action potential rate for single stimulation is much lower (apical activation: 56 Hz, basal activation: 41 Hz). The morphology of SCNs

suggests that synaptic stimulation of the apical dendrite evokes an action potential with a shorter latency than basal dendritic activation because of the shorter distance to the AIS. This might allow a slight compensation for different arrival times from different sensory systems. To see if a temporal offset of one stimulation site influences the response rate, the visual and auditory input were pre-activated 100 ms before the other sensory input (Figure 18A). A pre-activation of apical synapses evoked a spiking rate of 21 Hz, a pre-activation of basal synapses generated an action potential rate of 20 Hz, and a simultaneous activation of apical and basal activation led to a spiking rate of 23 Hz. The PSTHs of the three activation protocols (Figure 18B) show a peak shortly after 200ms, which represents the onset of the second or of both stimuli in parallel. The highest peak is visible in case of a simultaneous activation (~220 APs per bin), intermediate during preactivation of the apical dendrite (~160 APs per bin) and lowest but also broadest during preactivation of the basal dendrite (~120 APs per bin).

In a last data set, cross correlations of the voltage traces of presynaptic neurons (apical or basal) and the model were performed (Figure 18C), which shows how reliable presynaptic stimulations transform into postsynaptic activity. In the multi-compartment model, the correlation is higher for inputs at the apical synapse. This indicates that it is more likely to evoke an action potential output to an apical input activation than to a basal input activation. With these findings, the apical dendrite is assumed to propagate information more reliably than the information is propagated by the basal dendrite during simultaneous activation.

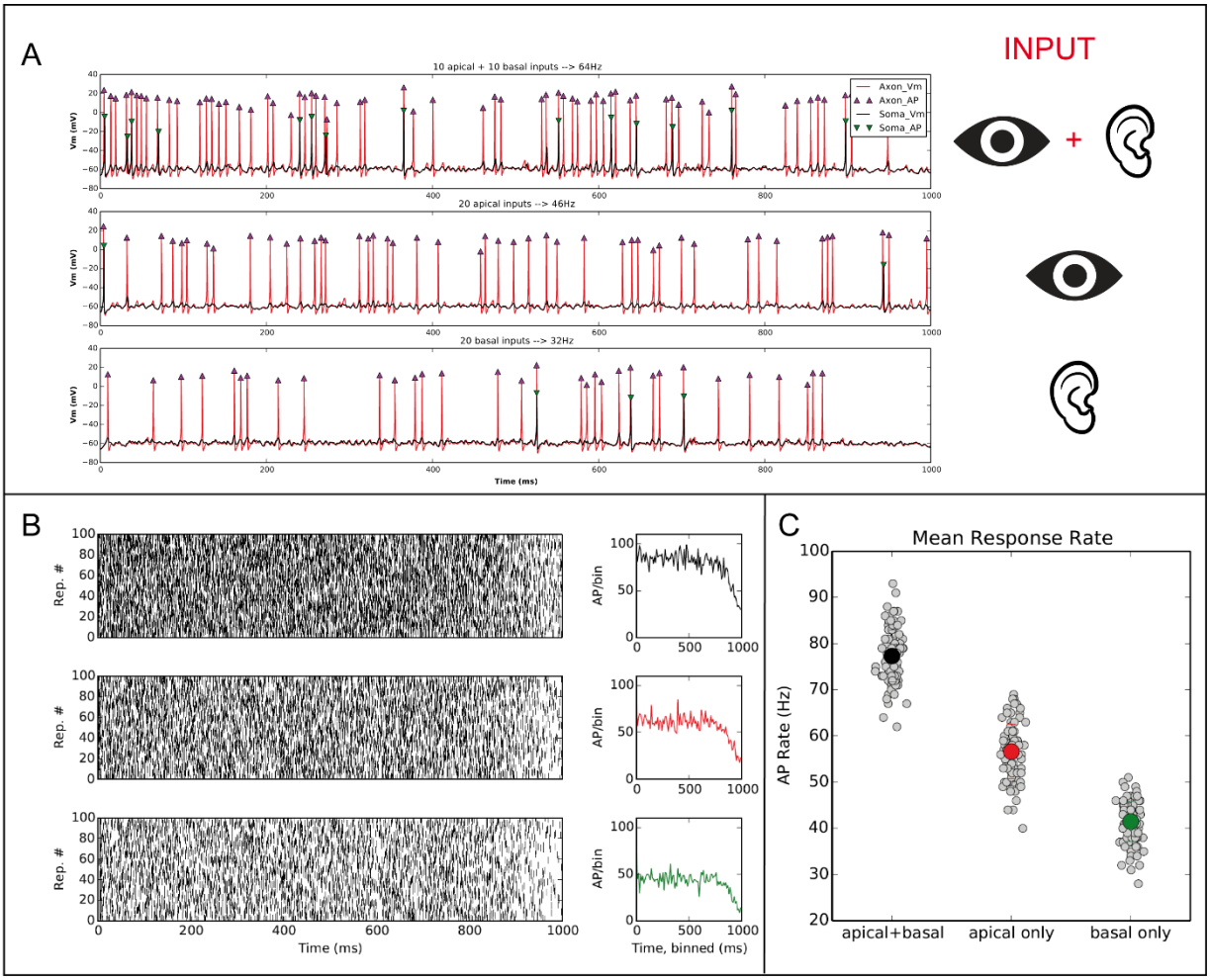

Figure 17. Response pattern of the multi-compartment model.
(A) Exemplary response pattern to three stimulus paradigms. In the upper diagram, the action potential rate on soma and axon is shown after double stimulation. In the middle diagram, the action potential rate on soma and axon is shown after visual stimulation. In the lower diagram, the action potential rate on soma and axon is shown after auditory stimulation. red trace: membrane voltage at axon recording site. green trace: membrane voltage at soma recording site. violet triangle: action potentials on axon. green triangle: action potentials on soma. (B) Repetitive activation of both (upper left panel), apical (middle left panel), and basal (lower left panel) stimulation sites (each n=100). Progression of numbers of action potentials per bin is shown for simultaneous activation (upper right panel) compared to single activation of apical (middle right panel) and basal stimulation site (lower right panel). (C) Mean response rate (Hz) to simultaneous or individual activation of apical and basal synapses. During double stimulation (black circle, 64 Hz) the action potential rate is enhanced compared to only visual (red circle, 46 Hz) and auditory (green circle, 32 Hz) stimulation.

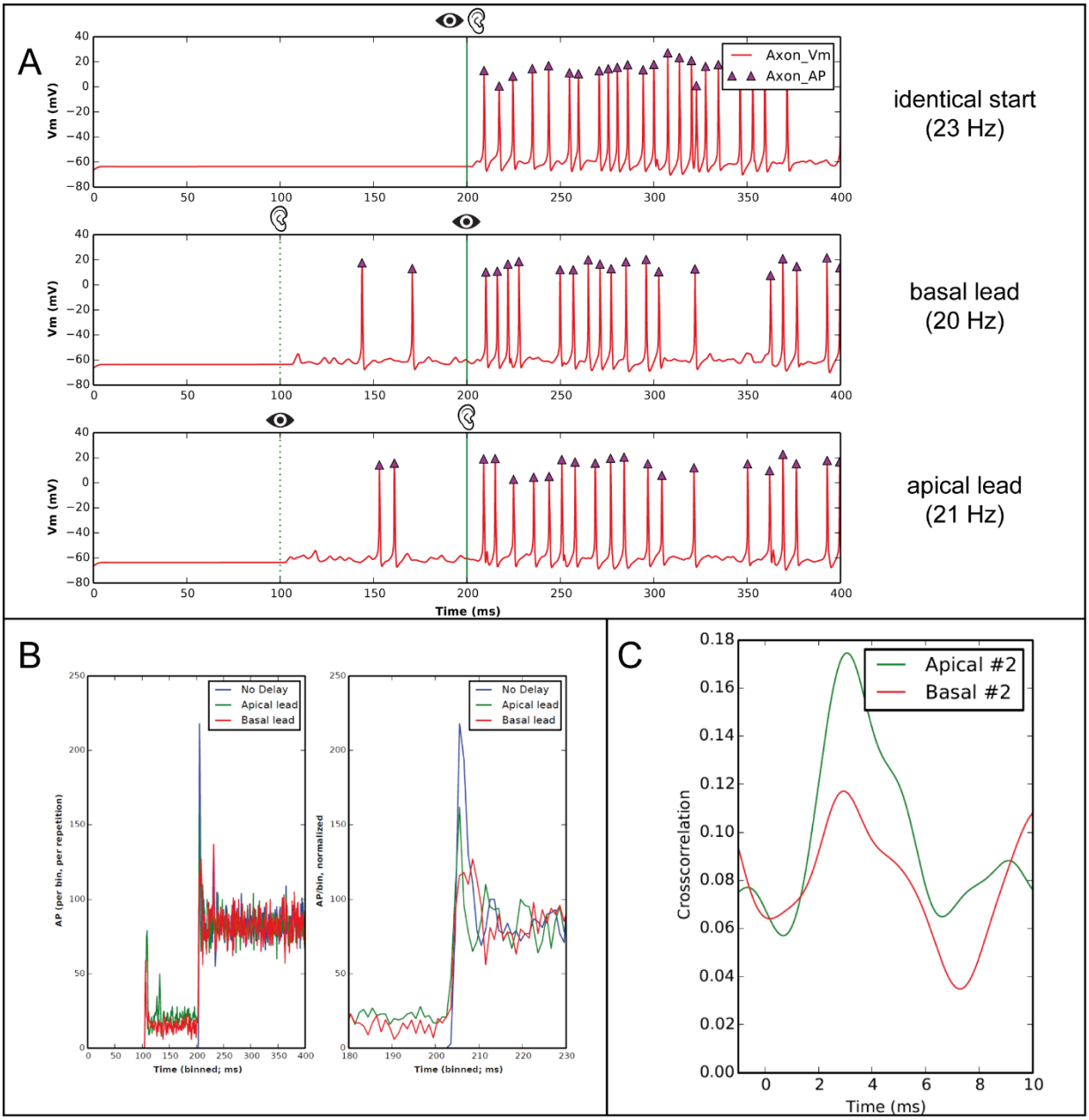

Figure 18. Effect of a temporal offset of one stimulation site on the multi compartment model response
(A) Preactivation of a single input shows no change in overall response rate. The upper diagram shows a simultaneous activation of both input regions. The middle diagram shows a preactivation of the auditory input region, while the lower diagram shows a preactivation of the visual input region. (B) Peristimulus time histogram (PSTH) for the three different stimulation protocols (no delay between visual and auditory activation: blue line; visual signal is activated 100 ms before the auditory signal: green line; auditory signal is activated 100 ms before the visual signal: red line). The highest peak is visible if the visual and auditory signal were simultaneously presented. The right diagram shows a detailed view of the PSTH at double stimulus onset. (C) The diagram shows the cross correlation of the input and output of apical and basal voltage traces, respectively. The cross correlation is higher after activation of apical dendrites.

Plasmid cloning for GFP expression in layer 10 neurons of the chicken optic tectum

The theoretical functionality shown by the multi-compartment model based on anatomical studies gave hints on how SCNs integrate two sensory modalities and further process them to the isthmic system. However, these results and predictions have to be related to physiological data. Therefore, hybrid voltage sensor imaging experiments were performed. This experimental approach is based on two components: an electron acceptor and an electron donor. Usually, the electron donor is a fluorescent dye. This dye can be directly introduced into the cell immediately before the experiment or introduced via a plasmid encoding an appropriate fluorophore. The latter method includes plasmid transfection and *in ovo* electroporation of chicken embryos at an early developmental stage. The theoretical advantages of genetically prelabelled neurons in the TeO are cell type specificity through plasmids containing specific markers for tectal cells, the saving of time, and the stable and homogeneous GFP expression in cells of the same cell type.

Figure 19 shows an example of a transfection at E2. Typically, I saw intense expression in cells in layer 13 (Figure 19C) and layer 9 (Figure 19D), and in some superficial layers (Figure 19B-D). The cells in layer 13 are presumably different SGC cell types (Luksch et al., 1998), however, dendritic endings can hardly be differentiated as they are possibly covered by other neurons. Most of the GFP expressing cells in layer 9 are presumably neurons projecting from the optic tectum to the isthmo-optic nucleus (ION) (Crossland & Hughes, 1978; Repérant et al., 2006; Wylie et al., 2009). In the ION, an intense labelling is visible. In layer 10, I also found transfected cells with the shape of Shepherd's crook neurons (Figure 19E-G).

Theoretically, different vectors could result in different expression patterns. Thus, I tested several vectors with different promotors. The three tested plasmids were pAcGFP, pβactin_eGFP and pCAG_AcGFP. pAcGFP and pCAGGFP encode a membrane-bound GFP, while pβactin_eGFP expresses a cytosolic GFP (Figure 19A). In addition, I applied recombinant adeno-associated viral vectors (rAAVs). Here, four different AAVs types were chosen. The vectors were distinguishable by their capsid region. The difference in this region causes different tissue specificity (Aschauer, Kreuz, Rumpel, & Qiu, 2013; Burger et al., 2004; Surace & Auricchio, 2008).

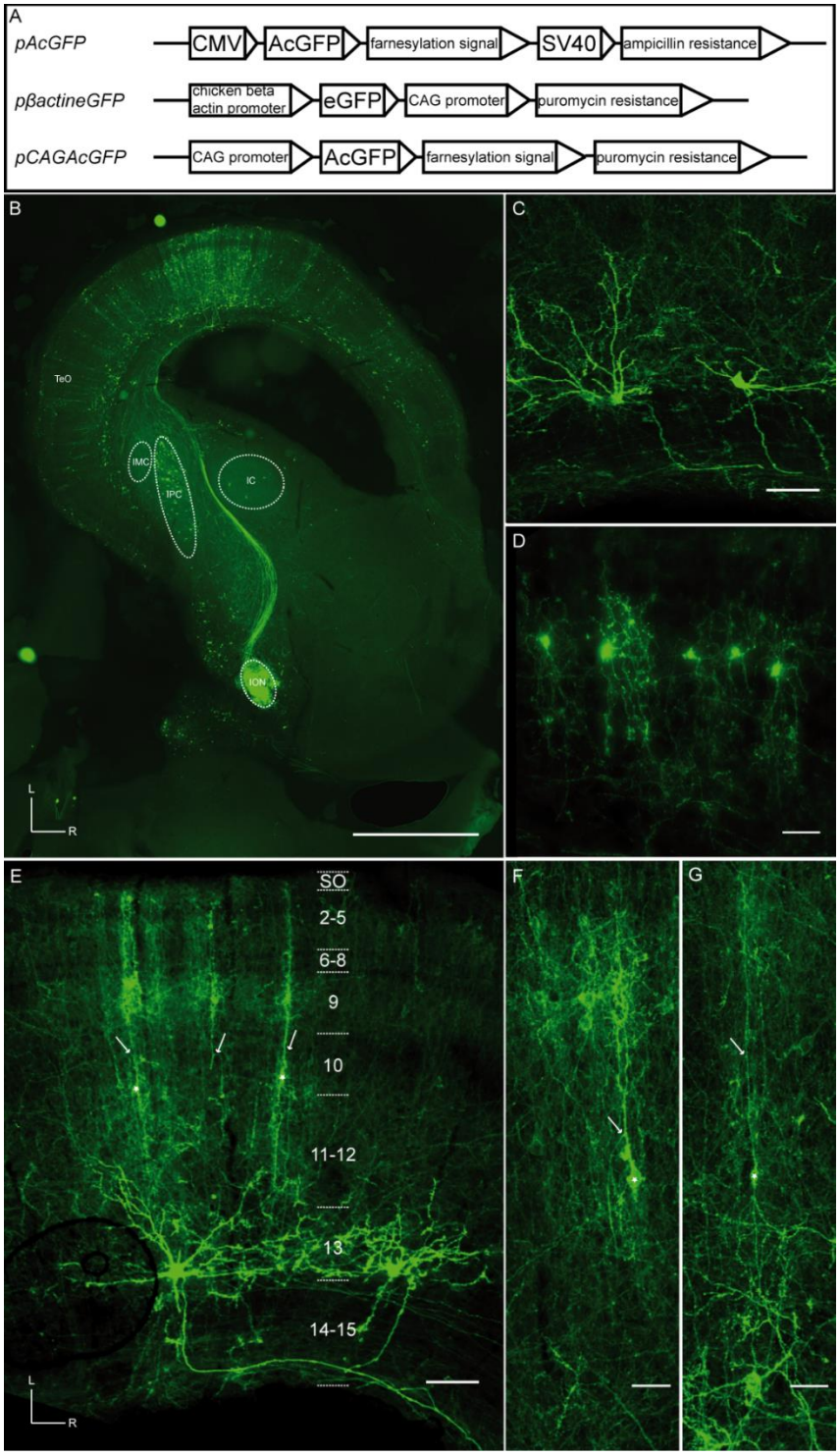

Figure 19. GFP expressing neurons in the chicken midbrain by transfection at HH11.
(A) Three different plasmids for *in ovo* transfection and electroporation. pAcGFP contains sequences of a CMV promoter, a membrane-anchored GFP, a farnesylation signal, a SV40, and an ampicillin resistance. pβactin_eGFP contains sequences of a chicken β-actin promoter, a cytosolic GFP, a CAG promoter, and

Figure 19 continued **I** a puromycin resistance. pCAG_AcGFP contains sequences of a CAG promoter, a membrane-anchored GFP, a farnesylation signal, and a puromycin resistance. (B) Exemplary overview of the optic tectum after transfection with one of the GFP-containing plasmids. The embryo was transfected with the plasmid pβactin_eGFP. TeO: optic tectum. IMC: *nucleus isthmi pars magnocellularis*. IPC: *nucleus isthmi parvocellularis*. IC: inferior colliculus. ION: istmo-optic nucleus. Scale bar 1000 µm (C) Two GFP expressing neurons located in layer 13. The embryo was transfected with the plasmid pβactin_eGFP. Scale bar 100 µm. (D) Five GFP-expressing neurons in layer 9. I assume that the axon of these cells project to the ION. The embryo was transfected with the plasmid pAcGFP. Scale bar 50 µm. (E) Three SCN cells with their soma located in layer 10 and two SGC cells with their soma located in layer 13. Note the fine dendritic branching of the SCN cells in layer 9. The embryo was transfected with the plasmid pAcGFP. Scale bar 100 µm. The numbers indicated the corresponding layers according to Ramón y Cajal. (F) and (G) Detailed view of two SCN cells. Arrows indicate the axon branch from the apical dendrite. Asterisks indicate the soma. The embryo was transfected with the plasmid pAcGFP. Scale bar in (F) and (G): 50 µm. L: lateral. R: rostral.

In this study, GFP expression data are only shown for the transfection with two of the three plasmids pAcGFP and pβactineGFP. However, a study with the third plasmid (pCAGGFP; Markus Ballmann, Research internship at the chair of zoology, 2018) showed comparable results. In general, I was able to obtain a bright GFP expression in tectal neurons with all bacterial plasmids but without a preference for particular cell types by one plasmid. None of the tested AAVs led to an expression of GFP in cells.

As the variation of plasmids did not show any selectivity for specific neurons and as specific marker for the SCN were not available, my next approach was to transfect progenitor cells at different stages in the early development of chicken embryos. With this method I attempted to find the right transfection time point at which SCNs are most successfully labeled. I injected plasmids at embryonic day 2 (E2) to E5.

The result of the transfection at E2 was already shown in Figure 19. Transfection at E3 resulted mostly in GFP expression in cells in the superficial layers (Figure 20). Here, several cell types were visible, e.g. horizontal cells in retinorecipient layers (Figure 20B-D). Rarely, layer 13 cells were also visible after transfection at E3 (Figure 20A). Occasionally, the expression was indistinct and cells in several layers were transfected, which might result from the delayed development of the optic tectum in its anterior-posterior axis (Figure 20A). Older embryonic stages could not be evaluated since none of the transfected embryos survived until the developmental stage at which I evaluated the GFP expression.

This approach showed that there are different expression patterns dependent of the transfection time during development. I found a bright fluorescence signal in tectal neurons after transfection with GFP-encoding plasmids at E2 and E3. Unfortunately, both developmental transfection stages were not specific for Shepherd's crook neurons.

In general, the survival rate and the transfection efficiency were low (Figure 21). As the brain structures are completely differentiated at E18, I attempted to optimize the survival rate of transfected embryos until E18 to E21. I chose this developmental range as I planned to perform hybrid voltage sensor imaging experiments at this embryonic stage. The survival rate at E5 was 80 % ± 17 %, at E10 46 % ± 21 %, at E15 32 % ± 22 %, at E20 7 % ± 12 % and at E21 1 % ± 3 % (N=26, n=756, Figure 21A).

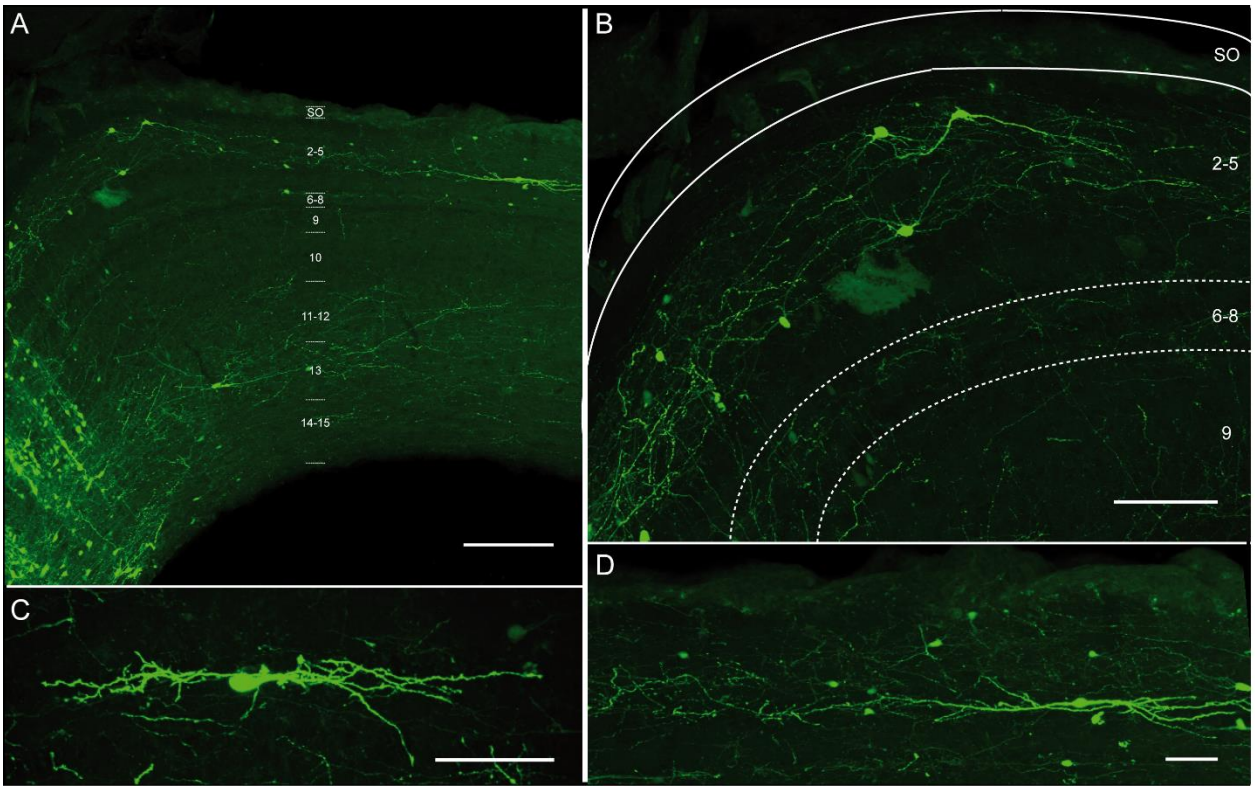

Figure 20. GFP-expressing neurons in the chicken midbrain by transfection at HH20.
(A) Exemplary overview of the optic tectum after transfection with the GFP-encoding plasmid pβactin_eGFP. Scale bar: 200 µm. (B) Transfection of E3 showed mainly GFP expression in neurons in the retinorecipient layers. Scale bar: 100 µm. (C) and (D) Horizontal cells in retinorecipient layers. The soma is located in layer 6 (C) and layer 4 (D). Scale bar in (C) and (D): 50 µm.

Regarding the transfection at four different embryonic stages (Figure 21B and C), the percentage of surviving embryos transfected at E2 was 15 % ± 5 % (N=9, n=271) with a transfection efficiency (proportion of embryos expressing GFP in the tectal cells) of 35 % ± 39 % (N=9, n=271). At E3 transfected embryos survived to a similar amount (15 % ± 3 %; N=4, n=99)) with a transfection efficiency of 5 % ± 11 % (N=4, n=99). The survival rate of later transfected

embryos was 0 % (E4; N=3, n=48) and 5 % ± 2 % (E5; N=13, n=34). The transfection efficiency for these developmental stages was not calculated as no GFP expression was observed.

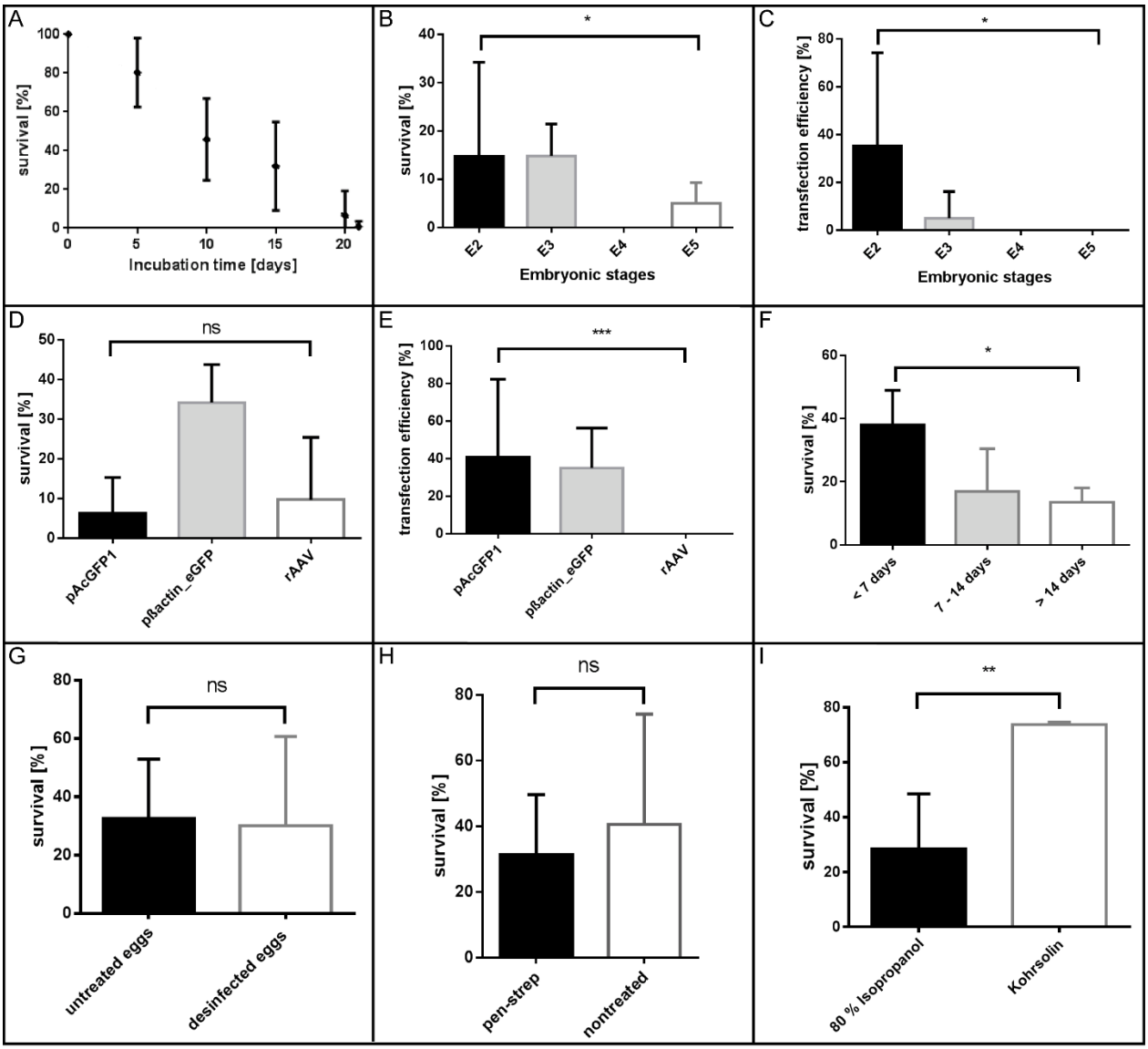

Figure 21. Survival rate of transfected embryos dependent on embryonic stage, plasmid, egg handling and disinfectants.
(A) The survival rate was calculated by the normalization of the surviving embryos at the five developmental stages to the total amount of transfected embryos. E5 80 % ± 17 %. E10 46 % ± 21 %. E15 32 % ± 22 %. E20 7 % ± 12 %. E21 1 % ± 3 %. N=26, n=756. (B) Survival rate of embryos transfected at different embryonic stages. (C) Transfection efficiency after transfection of embryos at different embryonic stages. (D) Survival rate of embryos which are transfected with different vectors. not significant. (E) Transfection efficiency after transfection with different vectors. (B) and (C) E2: N=9, n=271. E3: N=4, n=99. E4: N=3, n=48. E5: N=13, n=34. (D) and (E) pAcGFP: N=19, n=430. pβactineGFP: N=2, n=41. rAAV: N=14, n=27. significant ($p<0.05$): *. not significant: ns. The x-axis indicates the embryonic stages in (B) and (C). The y-axis shows the survival rate in percent [%] in (B and (D).

Figure 21 continued **I** The x-axis indicates the vectors used for transfection (D) and (E). The y-axis shows the transfection rate in percent [%] in (C) and (E). (F) Survival rate is dependent on storage time. The highest survival rate was achieved at an egg storage duration between 0 and 7 days (38 % ± 11 %; N=4, n=150). Between 7 and 14 days the survival rate decreased to 17 % ± 13 % (N=6, n=230). The lowest number of survived animals was counted at egg storage times of 14 days or longer (13 % ± 5 %; N=2, n=69). (G) Survival rate dependent on the disinfection of the egg shell before opening the shell to get access to the embryo for transfection. (H). Adding a mixture of penicillin and streptomycin (pen-strep) to the opened egg before resealing the shell had no impact on the survival rate. (I) Disinfection of the breeder with a commercially available solution increased the survival rate of transfected embryos. significant ($p<0.05$): *. not significant: ns.

I was also interested in the influence of the three different vectors on the survival rate of the embryos and the transfection efficiency with each of these three vectors (Figure 21D and E). The number of embryos surviving until E20 was 6 % ± 9 % in case of pAcGFP with a transfection efficiency of 40 % ± 41 % (N=19, n=430). For pβactin_eGFP, the survival rate was 34 % ± 10 % with a transfection efficiency of 35 % ± 21 % (N=2, n=41). Using rAAV, the survival rate was 10 % ± 16 % in which no GFP expression was observed (N=14, n=27).

Using in ovo electroporation to introduce GFP-encoding vectors, the survival rate of the chicken embryos was low. However, Figure 21A does not describe the observed phenomena in the first and last days of embryonic development. The highest decrease of the embryonic survival rate occured usually in the first 24h after *in ovo* electroporation. A second strong decrease was seen between E18 and E21, where again a lot of embryos died. Potential influenceable causes are the applied current during electroporation, a higher infection rate with viruses or bacteria due to infection caused by the egg handling or a long storage time of the eggs prior to incubation.

Therefore, several parameters were tested to enhance the survival rate in the transfected developing embryos. The comparison of parameters to optimize the survival rate involved the impact of the storage length of the eggs before incubation (Figure 21F, storage temperature 18 °C), the addition of antibiotics (Figure 21 H, penicillin – streptomycin, 10,000 units penicillin and 10 mg streptomycin per mL in 0.9% NaCl, Sigma-Aldrich, 1:100 diluted in chicken-ringer) to the chicken ringer solution, the disinfection of the eggs with 80% isopropanol (Figure 21G) and the impact of enhanced disinfection of breeders with antiviral disinfectants (Khorsolin®) before start of incubation (Figure 21I). The best storage length found in this project was to a maximum of 7 days before incubation (Figure 21F). The survival rate until E21 for a storage time not longer than 7 days was 38 % ± 11 % (N=4, n=150). Storing the eggs between 7 and 14 days reduced the survival rate to 17 % ± 13 % (N=6, n=230). Increasing the storage time to 14 days and longer lead to a survival rate of 13 % ± 5 % (N=2, n=69).

As the low survival rate can also be caused by bacterial or viral infection, I tested several parameters. Adding a mixture of penicillin and streptomycin antibiotics to the developing embryo did not affect the number of survived animals (Figure 21H). The survival rate of untreated embryos was 40 % ± 34 % (N=8, n=107) and the rate of treated 31% ± 18 % (N=8, n=114). Also, the disinfection of the egg shell before opening had no significant impact on the survival rate (Figure 21G). The survival rate of the untreated eggs was 33 % ± 20 % (N=19, n=501) and the survival rate of the disinfected eggs was 30 % ± 31 % (N=7, n=258). At least the disinfection of the breeders before the egg incubation had an impact on the survival rate (Figure 21I). Without disinfection the survival rate decreased to 28 % ± 20 % (N=24, n=656) compared to the survival rate of 74 % ± 1 % (N=2, n=103) while using disinfected breeders.

To avoid the procedure of electroporation with all negative effects of applying voltage pulses to the embryo, adeno-associated viral vectors of four different serotypes (AAV1, 5, 8, and 9) carried by a backbone vector of serotype 2 (AAV2) were tested. However, the survival rate was not enhanced compared to other vectors (Fig 21D and E). Furthermore, none of the viruses resulted in GFP expression. In mice, it was shown that these serotypes resulted in GFP expression (Davidson et al., 2000). To understand this discrepancy, I compared the heparan sulfate proteoglycan (HSPG) receptor of mice and chicken using the online software tool BLAST (basic local alignment search tool). Host cells encode for the receptor (membrane-specific heparan sulfate proteoglycan core protein) required for the uptake of the target gene (O'Donnell, Taylor, & Chapman, 2009). The presentation of HSPG receptor on the host cell surface led to the binding of the virus at the outer cell membrane and the begin of the endocytosis. The amino acid sequence of this protein differs in mouse and chicken (identity score point: 56.1 %, Table 6), which could be the reason for lacking GFP expression in the experiments presented in this study.

Table 5. Alignment of heparan sulfate proteoglycan receptor in mouse and chicken
The amino acid sequence of the heparan sulfate proteoglycan receptor was aligned in mouse (Mus musculus) and chicken (Gallus gallus). The alignment analysis was performed by BLAST search against UniProtKB. E-value: number of distinct alignments that are expected to occur in a database search by chance; Score: numerical value for the quality of the alignment. Higher numbers correspond to higher similarity. Ident.: Sequence identity percent; Positives: residues that are very similar to each other; Query Length: count of residues of the template sequence, Match length: count of residues of the compared sequence.

	Q6KDZ1_CHICK - HSPG receptor *Gallus gallus* (chicken)	B1B0C7_MOUSE - HSPG receptor *Mus musculus* (Mouse)
E-value	0.0	0.0
score	21851	9692
Identity [%]	100	56.1
Positives [%]	100	68.5
query length [bp]	4071	4071
match length [bp]	4071	4375

Signal propagation in Shepherd’s crook neurons after visual and auditory stimulation

In addition to the model, I performed hybrid voltage sensor imaging experiments to analyze the signal propagation in the SCN. The stimulation paradigm of this physiological approach resembled the design of the multi-compartment model.

I tested and optimized the eGFP expression in the chicken midbrain to obtain a sufficient amount of labelled SCNs for hybrid voltage sensor imaging experiments, but I did not achieve this goal. Therefore, I started to label every cell with a patch electrode before recording its activity to stimuli mimicking visual, auditory and audiovisual input. The *in vitro* approach allows to access SCNs in the chicken optic tectum. The optic tectum was oriented in a medio-lateral line in the recording chamber and two stimulation electrodes were positioned in the corresponding layers to mimic visual and auditory input. In this configuration, I typically measured signals from the soma and proximal parts of the apical and basal dendrite. Signals from finer structural elements were usually not distinguishable from noise.

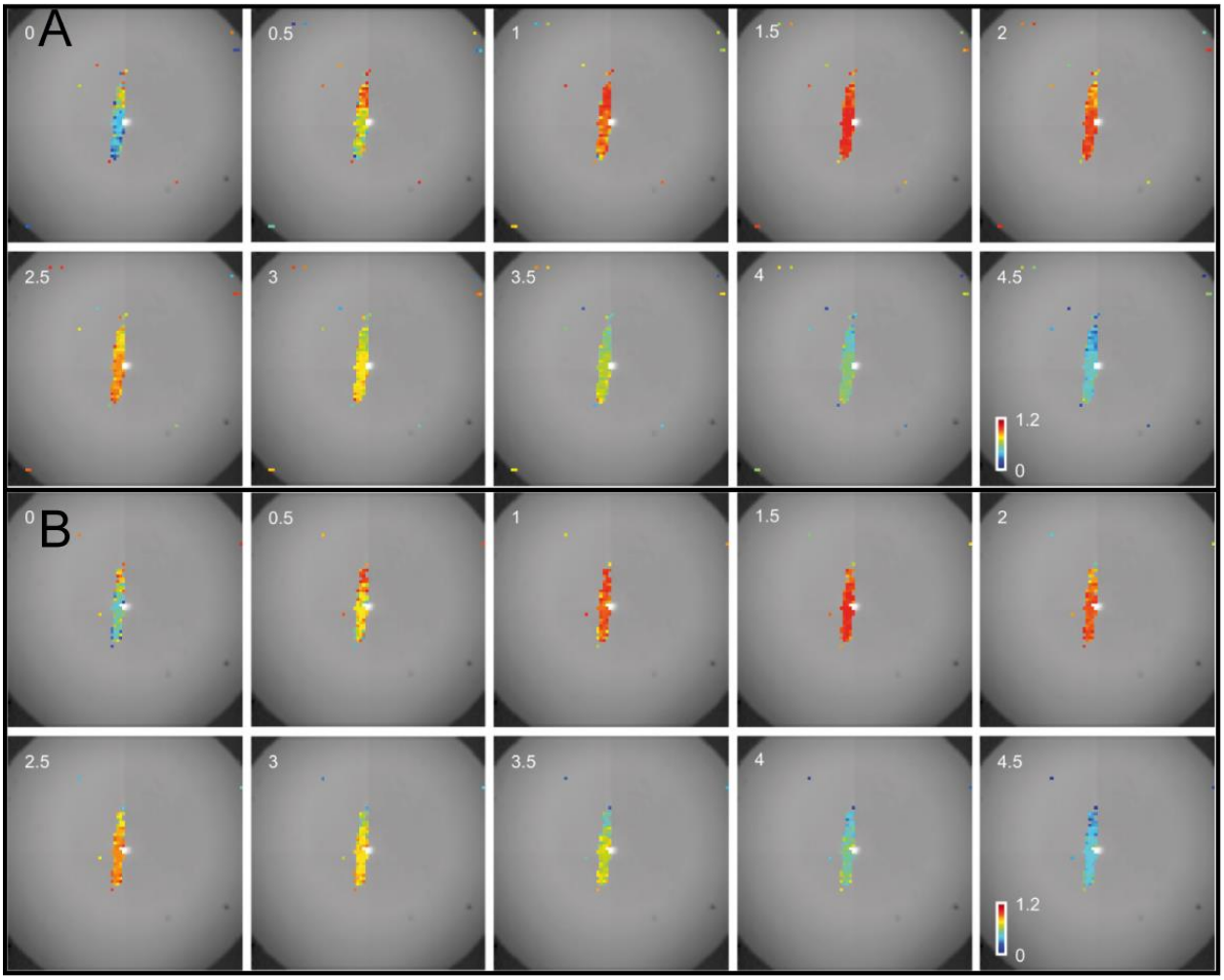

Figure 22. Single frames of an exemplary video showing the signal propagation evoked by visual (A, mean of 4 APs) and auditory stimulation (B, mean of 7 APs). Data were analysed according to Hochbaum et al. (2014). Frames are extracted every 0.5 ms. The amplitude is color-coded (red = high signal amplitude, dark blue = low signal amplitude). Only signals which cross a predefined threshold (~0.2) are plotted. The cells in (A) and (B) are oriented in such a way that the top of the cell in each image points to the superficial layers of the tectum and the bottom of the cell to the deeper layers of the tectum.

Figure 22 shows an exemplary result of a SCN to the stimulation at the apical and basal dendrite, respectively. The signal was averaged, normalized, substituted by a template based on a mean action potential form (Hochbaum et al, 2014) and plotted in chronological order. To occlude noise, only the part of the signal crossing a threshold is visible. In both stimulus conditions (Figure 22A: stimulation of apical dendrite [above the images]; Figure 22B: stimulation of basal dendrite [below the image]) the maximal amplitude is first visible in the upper part before it continues to spread to the lower part of the neuron.

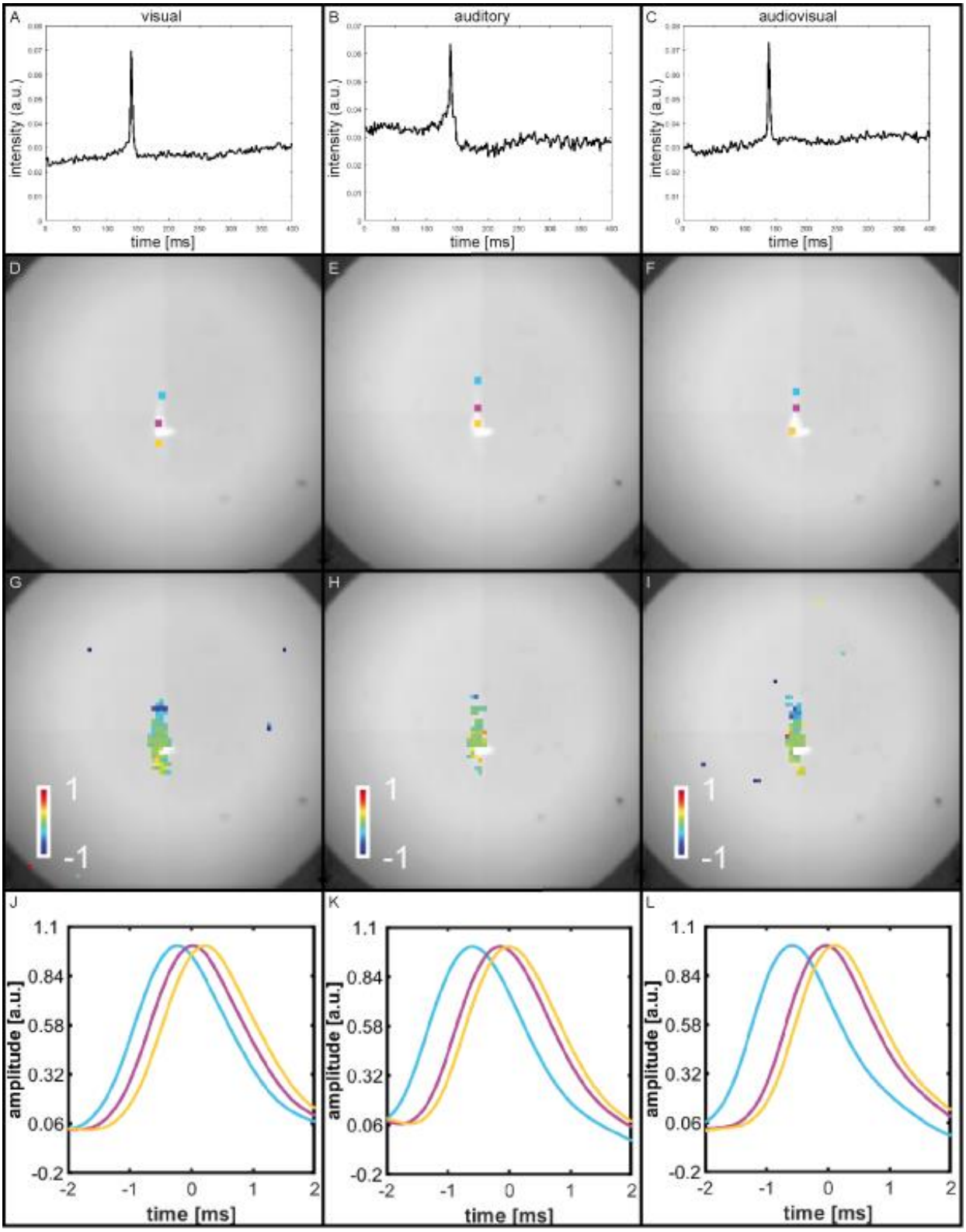

Figure 23. The signal propagation is independent of the stimulation site.
Traces of single pixels of SCN response to stimulation of apical dendrite (A, visual, N=4), basal dendrite (B, auditory, N=7) and the combination of apical and basal dendrites (C, audiovisual, N=6). In (D) to (F) the three selected points are shown used in following images (color code).

Figure 23 continued **I** The third row shows the average latency of the peak of the action potential the 'visual stimulation' experiment (G) and the 'auditory stimulation' experiment (H) and during simultaneous 'visual and auditory stimulation' experiment (I). The color bar represents -1 (blue) to +1 ms (red). Processed response at the three selected points to 'visual stimulation' (J), 'auditory stimulation' (K), and simultaneous 'visual and auditory stimulation' (L). Raw data were ten times oversampled, the time point of action potential occurrence was extracted by cross correlation of raw data and a template of an action potential. Raw data was then replaced by the template to correct for effects on signal amplitude caused by labelling and intensity differences.

Figure 23 compares the response of the neuron shown in Figure 22 to visual stimulation (Figure 23A), auditory stimulation (Figure 23B) and simultaneous stimulation of visual and auditory (Figure 23C). The upper row shows the response at a single pixel at the soma. In all cases, the cell responded with a short action potential. In Figure 23D to E (second row), the panels show the DiO-labelled cell overlaid with the three selected pixels. The panel in the third row (G – I) shows the relative latency of the maximum of the action potential in a color code (blue -1 ms to red +1 ms). This analysis showed that, independent of the site of stimulation, the propagation of the signal started always apical of the soma and spreads towards basal (visual n=4, auditory n=7, audiovisual n=6). The corresponding processed data of selected points on the neuron confirmed the statement of signal propagation independent of stimulation site (oversampled, sorted via cross correlation to a template and raw data substitution with this template to correct for amplitude errors caused by different pixel intensities according to Hochbaum et al. (2014); Figure 26 J - L).

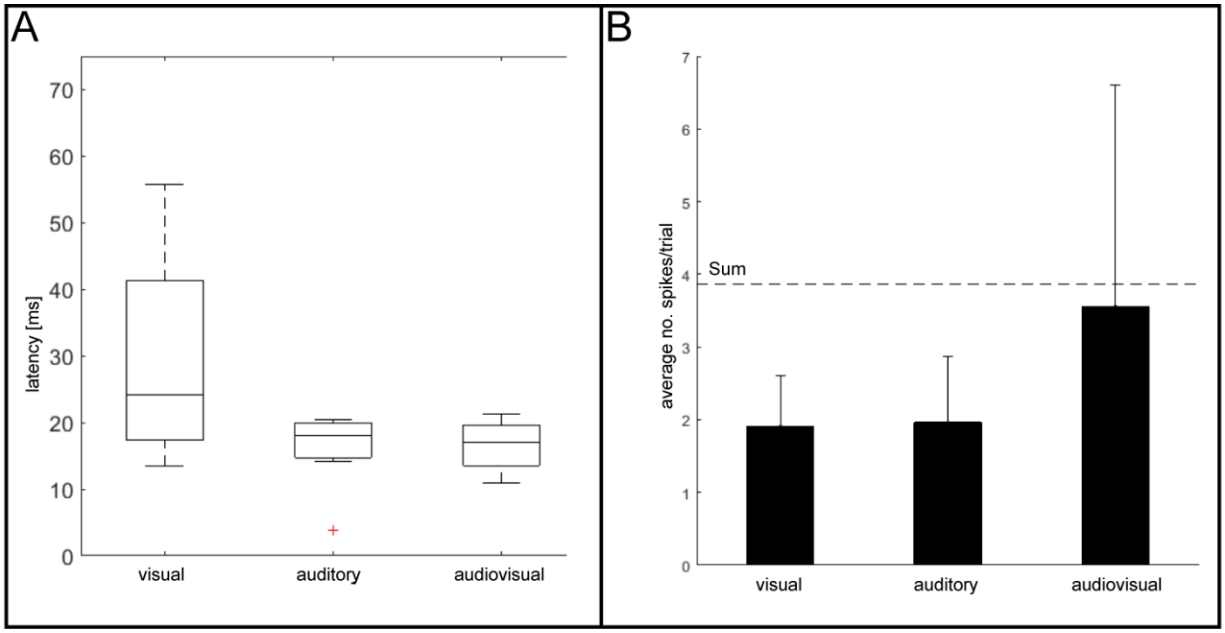

Figure 24. (A) Latency to stimulation at different stimulation sites in Shepherd's crook neurons. Responses seems to be evoked slightly faster to auditory (N = 7) and audiovisual stimuli (N = 4) compared to visual stimuli (N=4) Kruskal-Wallis test: visual compared to auditory: p= 0.54, visual compared to audiovisual: p= 0.46, auditory compared to audiovisual: p= 0.96. (B) Multisensory stimulation seems to enhance the average number of spikes per trial. One trial contains three single stimuli with an inter-stimulus interval of 200 ms. Audiovisual stimulation (3.27 spikes/trial, N=6) lead to an increased spike number compared to visual (1.74 spikes/trial, N=4) and auditory (1.89 spikes/trial, N=7) stimulation, respectively. The summation of spikes evoked after visual and auditory stimulation is still higher. Kruskal-Wallis test: visual compared to auditory: p= 0.39, visual compared to audiovisual: p= 0.09, auditory compared to audiovisual: p= 0.59.

Next to the question of signal spread in SCN, I was interested if there is evidence for multimodal integration. Multimodal integration should lead to a faster, enhanced and more reliable response in SCN. First, I compared the latencies of neuronal responses evoked by uni- and bimodal stimulation paradigms (Figure 24B). The latency of an action potential after the presentation of visual input (24.13 ms ± 12 ms, n=4) was longest compared to the latency of an action potential after the presentation of auditory (18 ms ± 19.25 ms, n=7) and audiovisual input (17 ms ± 3.06 ms, n=4, Figure 27). However, the differences were not significant. Next, I analyzed the response probability and by counting the evoked spikes per trial, which corresponds to three stimuli, and compared the number of spikes per trial for each stimulation paradigm (Figure 24A). Based on the stimulation protocol, the prediction was that during one trial 3 spikes are evoked. Visual input evoked responses with a probability of 58.02 % (1.74 spikes/trial, N=4, n= 10), auditory input evoked responses with a probability of 62.96 % (1.89 spikes/trial, N=7, n=9), and audiovisual input evoked responses with a probability of 108.89 % (3.27 spikes/trial, N=6, n= 24). The response probability to bimodal activation tends to be higher compared to visual or

auditory activation, however, this difference is not significant ($p>0.05$, Kruskal-Wallis test). No response enhancement was found greater than the sum of responses after unimodal stimulation (Figure 28).

In my stimulation paradigm, I stimulated the axon of retinal ganglion cells innervating the superficial layers by a stimulation electrode (visual stimulation) located in layer 2 to 4 and the axons projecting from the FRLx/IC to the deeper layers of the optic tectum by a stimulation electrode located in the deeper layers (auditory stimulation). However, the axon of SCN also cross the deep tectal layers, which could lead to direct, retrograde stimulation of SCN instead of synaptic basal activation. In case of direct stimulation, I expected to see nearly no delay between stimulus presentation and cell activity. However, such exceptionally short latencies were never found. Furthermore, such direct retrograde evoked potentials should be insensitive to calcium ion removal. I performed a series of pharmacological experiments using calcium free ACSF (Figure 25). The spiking activity after visual as well as after auditory stimulation decreased completely when no calcium ions were present anymore. These experiments underpinned that the way I stimulated the neurons led to synaptic rather than direct stimulation.

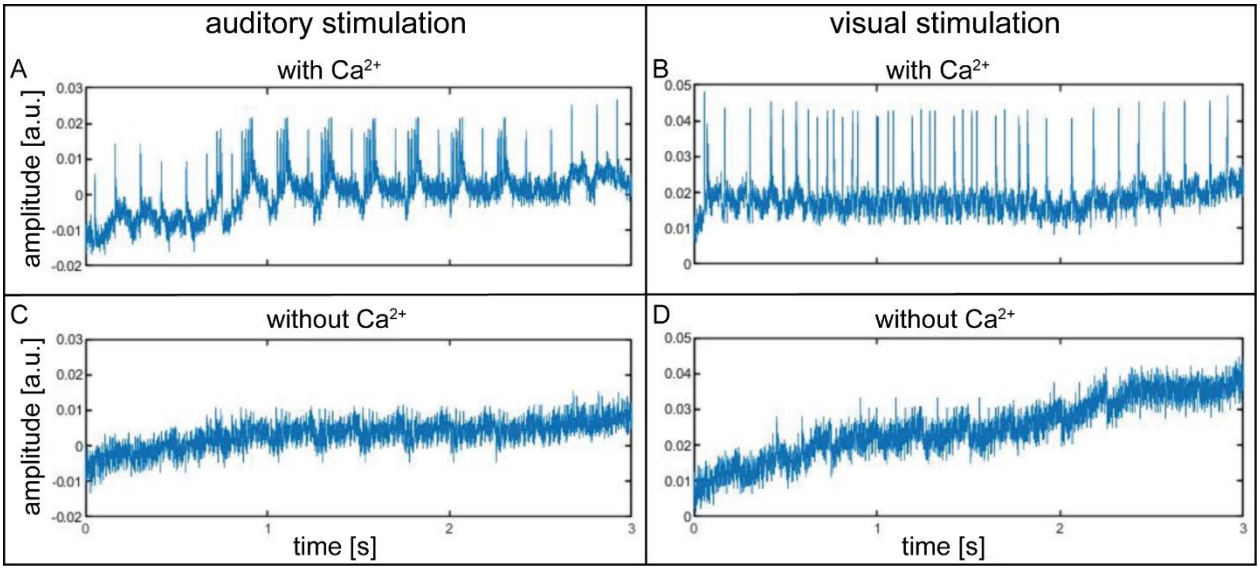

Figure 25. Pharmacological experiments investigating the nature of responses evoked by stimulation in upper (visual) and deeper layers (auditory)
Auditory (A) and visual (B) stimulation evoked spiking in Shepherd's crook neurons. Washing out calcium form the tissue by using calcium-free aCSF solution lead to the loss of spiking after auditory (C) and visual (D) stimulation.

Effect of missing retinal innervation on the development of Shepherd's crook neurons

I already could support the hypothesis that the Shepherd´s crook neuron receives different sensory information at its separate dendritic areas in the retinorecipient layers and the deep layers of the optic tectum. In this part of my thesis, I asked how removal of one sensory information influence the development of SCN anatomy and of the whole tectum.

Thus, I examined the changes of the optic tectum and of the morphology of Shepherd's crook neurons after early eye anlagen removal; in particular the fine dendritic structures.

First, the influence of unilateral lesions on the TeO was analyzed. Using this unilateral enucleation method, the embryos developed a normal hemisphere used as control, and an altered one (Figure 26). The layer thickness of the two tectal hemispheres was compared.

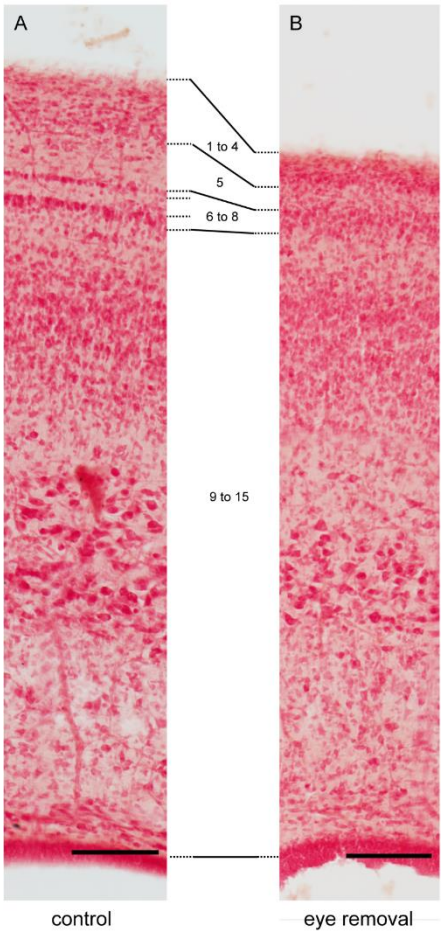

Figure 26. The optic tectum is reduced after unilateral removal of the eye anlagen. (A) The retinorecipient layers of a control optic tectum. Layer 6 and 8 are clearly visible as single-cell (layer 6) and multiple-cell (layer 8) band. (N = 11, n = 60). (B) The early eye removal has an impact on the retinorecipient layers. (N = 11, n = 60). Scale bar: 200 mm. Figure reproduced by Lischka, Yan, Weigel, & Luksch, 2018, with permission from the publisher.

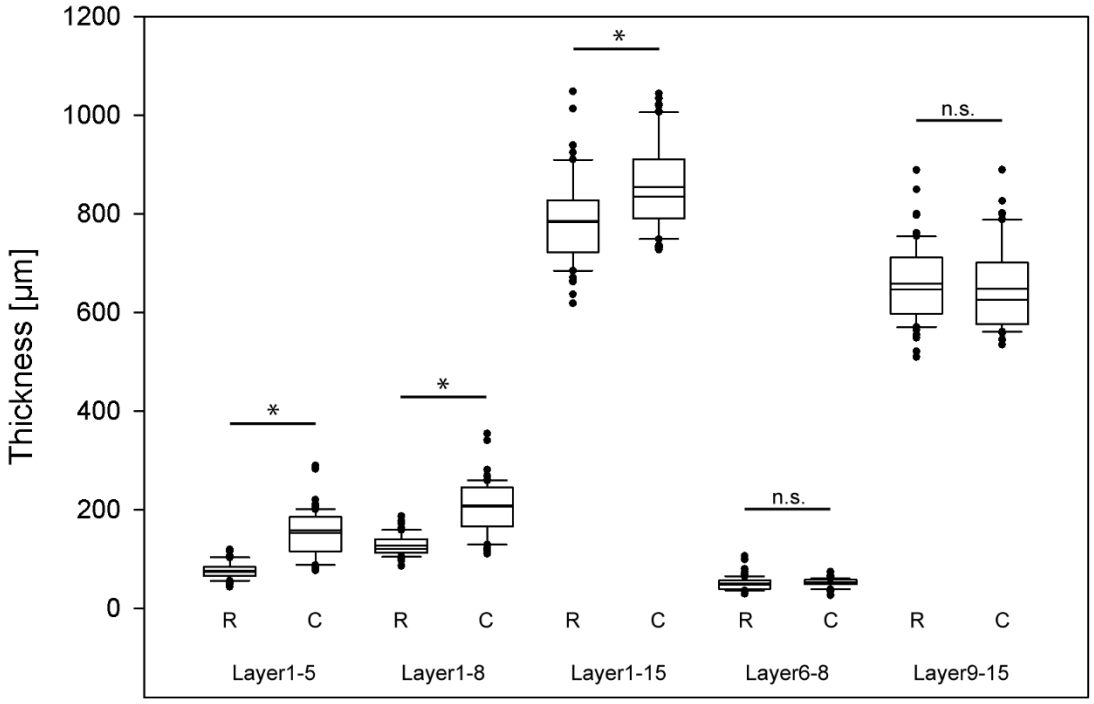

Figure 27. The effect of the eye anlagen removal on the thickness of the optic tectum.
Layer 1 to 5, layer 1 to 8, layer 6 to 8, and layer 1 to 15 are significantly reduced after early eye anlagen removal. C: control, R: early eye anlagen removal. Statistical test: Kolmogorov-Smirnov test followed by the Mann-Whitney rank sum test * significant. n.s. not significant. Figure reproduced from Lischka, Yan, Weigel, & Luksch, 2018, with permission from the publisher.

"In detail, the thickness of layer 1 – 5, layer 1 – 8, layer 1 – 15 and layer 6 – 8 was compared (Figure 27 and Table 7). Without retinal innervation, the retinorecipient layers of the TeO (layer 1 – 8) are strongly reduced by 42 % ($p < 0.001$ (Kolmogorov-Smirnov test followed by the Mann-Whitney rank sum test); early eye removal: 121.56 ± 16.63 µm, N = 11, n = 60; control: 208.96 ± 42.23 µm, N = 11, n = 60). Albeit the thickness of layer 9 – 15 was not changed ($p = 0.142$; early eye removal: 647.54 ± 61.53 µm, N = 11, n = 60; control: 626.52 ± 67.85 µm, N = 11, n = 60). In normally developed tecta, layer 6 is a one-cell layer, layer 7 contains no somata and layer 8 is again a densely packed cell layer. After early eye removal, this differentiation is lost, and the three layers are in a diffuse arrangement leading to a slight but not significant thinner layer 6 – 8 in enucleated embryos ($p = 0.091$; enucleated: 48.56 ± 10.61 µm; control: 53.70 ± 6.38 mm, each N = 11, n = 60). Layer 1 – 5 are considerably thinner when retinal innervation is lacking ($p < 0.001$; early eye removal: 74.09 ± 13.02 µm, N = 11, n = 60; control: 158.09 ± 37.62 µm, N = 11, n = 60).

Table 6. Layer thickness of early eye removal and control embryos.
Median values, the reduction after eye removal and significance levels are shown. Statistical test: Kolmogorov-Smirnov test followed by the Mann-Whitney rank sum test. * significant. n.s. not significant. † no reduction, the thickness increased in the lesioned embryo. Table reproduced from Lischka, Yan, Weigel, & Luksch, 2018, with permission from the publisher.

	Control [µm]	*Early eye removal [µm]*	*Significance*	*Reduction of [%]*
Layer 1 – 5 [µm]	158.09 ± 37.62	74.09 ± 13.02	*, p < 0.001	51.13
Layer 1 – 8 [µm]	208.96 ± 42.23	121.56 ± 16.63	*, p < 0.001	41.83
Layer 1 – 15 [µm]	835.73 ± 70.96	783.11 ± 67.09	*, p < 0.001	6.30
Layer 6 – 8 [µm]	53.70 ± 6.38	48.56 ± 10.61	n.s., p = 0.091	9.57
Layer 9 – 15 [µm]	262.52 ± 67.85	647.54 ± 61.53	n.s., p = 0.142	None†

It seems that the reduction of these layers (L1 to 5) is responsible for the overall reduction of retinorecipient layers when retinal innervation was missing. To further parse the reduction in these layers, I immunostained against calbindin (Figure 31), which is known to be expressed in layer 5 neurons. The calbindin-positive cells in layer 5 are horizontal cells with multipolar dendrites. The dendrites are running parallel to the surface of the optic tectum (Luksch & Golz, 2003). In the control optic tectum, I found somata and neurites of calbindin-positive cells in layer 5. Both, the number of cells and fine projections seem to be reduced by enucleation and also the thickness of the layer (Figure 28, p < 0.001; enucleated: 11.77 ± 1.51 µm, control: 42.92 ± 4.96 µm, each N = 2, n = 3; Table 8). However, enucleation also remarkably affected the size of layer 1–4 (p < 0.001; enucleated: 65.98 ± 1.98 mm, control: 162.18 ± 16.58 mm; each N = 2, n = 3).

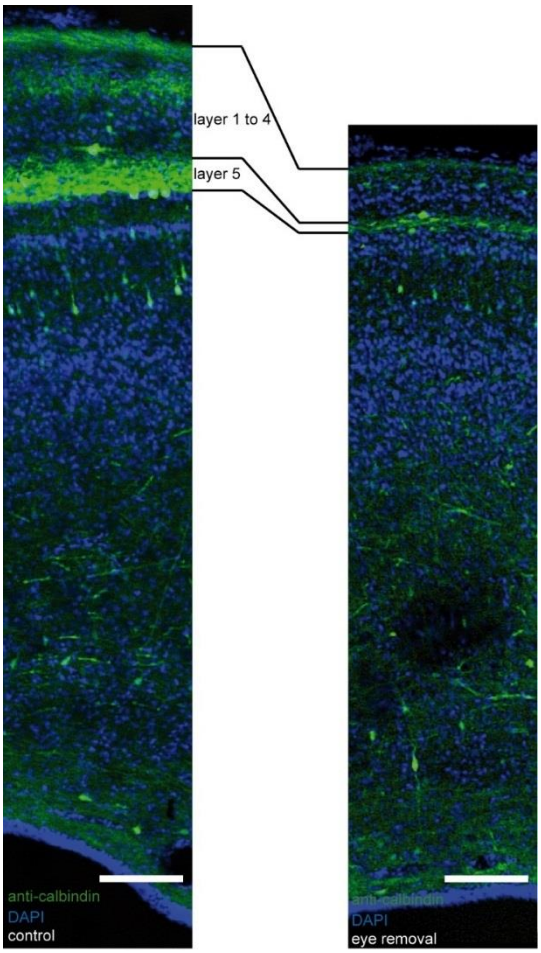

Figure 28. Strong reduction in layer 5 after early eye removal
(A) Calbindin is mainly expressed in the stratum opticum and layer 5 of the TeO. (B) The unilateral eye anlagen removal at an early embryonic stage causes the reduction of layer 5. Scale bar: 100 mm. Figure reproduced from Lischka, Yan, Weigel, & Luksch, 2018, with permission from the publisher.

Table 7. The superficial layers are significantly reduced after early eye removal.
Median values, the reduction after eye removal and significance levels are shown. * significant. Table reproduced from Lischka, Yan, Weigel, & Luksch, 2018, with permission from the publisher.

	Control [µm]	*Early eye removal [µm]*	*Significance*	*Reduction of [%]*
Layer 1 – 5 [µm]	208.44 ± 16.36	77.95 ± 3.20	*, $p < 0.001$	62.60
Layer 1 – 4 [µm]	162.18 ± 16.58	65.98 ± 1.98	*, $p < 0.001$	59.32
Layer 5 [µm]	42.92 ± 4.96	11.77 ± 1.51	*, $p < 0.001$	72.58

Furthermore, the lack of retinal innervation on Shepherd's crook neurons was analyzed by measuring different morphometrical parameters. The somata of SCNs are located in layer 10 with an apical dendrite extending to the retinorecipient layers and a basal dendrite ramifying in the deep layers. The axon emerges from the apical dendrite in layer 10a/9." After enucleation, the dendritic fine structures were reduced (Figure 29, $p = 0.032$, early eye removal: $N = 4$, $n = 10$; control: $N = 5$, $n = 13$). The reduction of the fine structures is based on the analysis of the surface of the apical and basal dendrites in cells of control and early eye removal hemispheres.

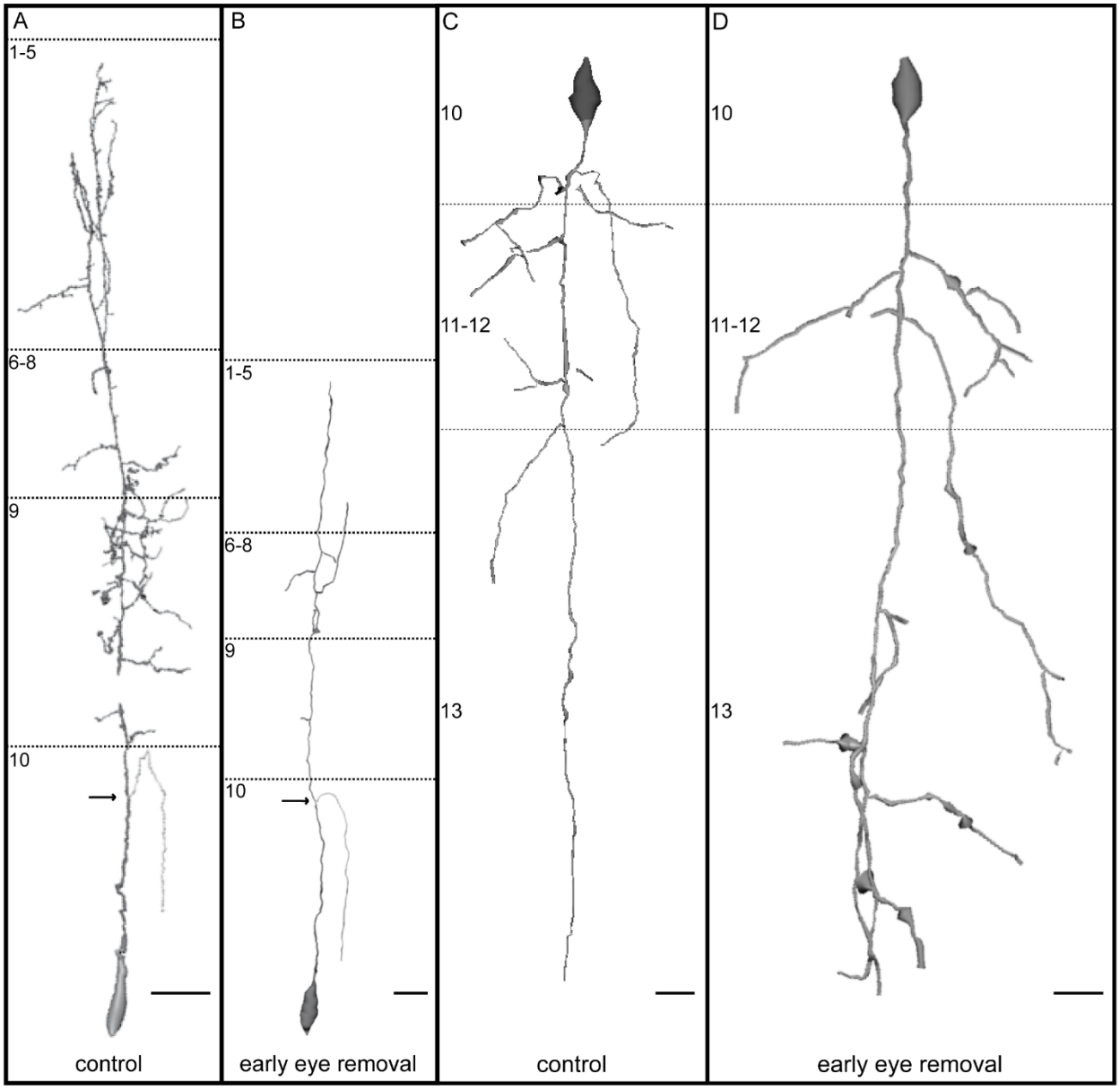

Figure 29. The early eye removal affects the outgrowth of the fine dendritic structures.
(A) Soma, primary dendrite, axon branch, and apical dendrite of SCN. (B) Soma, primary dendrite, axon branch, and apical dendrite of SCN after early eye removal. (C) Soma and basal dendrite of SCN. (D) Soma and basal dendrite of SCN after early eye removal. Figure reproduced from Lischka, Yan, Weigel, & Luksch, 2018, with permission from the publisher.

"To further quantify this, I analyzed the number of bifurcations and the surface of the apical dendrites. Both values were reduced by enucleation. I also compared the number of bifurcations and the dendritic surface of the basal dendrites. Here, I did not find any differences indicating that the number of bifurcations was altered after the removal of retinal innervation ($p = 0.512$, early eye removal: $N = 4$, $n = 6$; control: $N = 4$, $n = 6$). In addition, a significant reduction

(18.62 %) was found in the distance between the soma and the end of the apical dendrite (control: 229.64 ± 48.25, early eye removal: 186.88 ± 26.59, p = 0.008, Figure 30, upper left panel) as well as a significant reduction (16.54 %) of the distance between the axon branch and layer 8 (control: 100.59 ± 32.58, early eye removal: 83.95 ± 14.16, p = 0.021, Figure 30, lower left panel). This was expected because of the general reduction in size of the retinorecipient layers."[25] Other morphological parameters such as soma size, distance to the axon branch and to the basal dendrite were not significantly affected by enucleations (Figure 30).

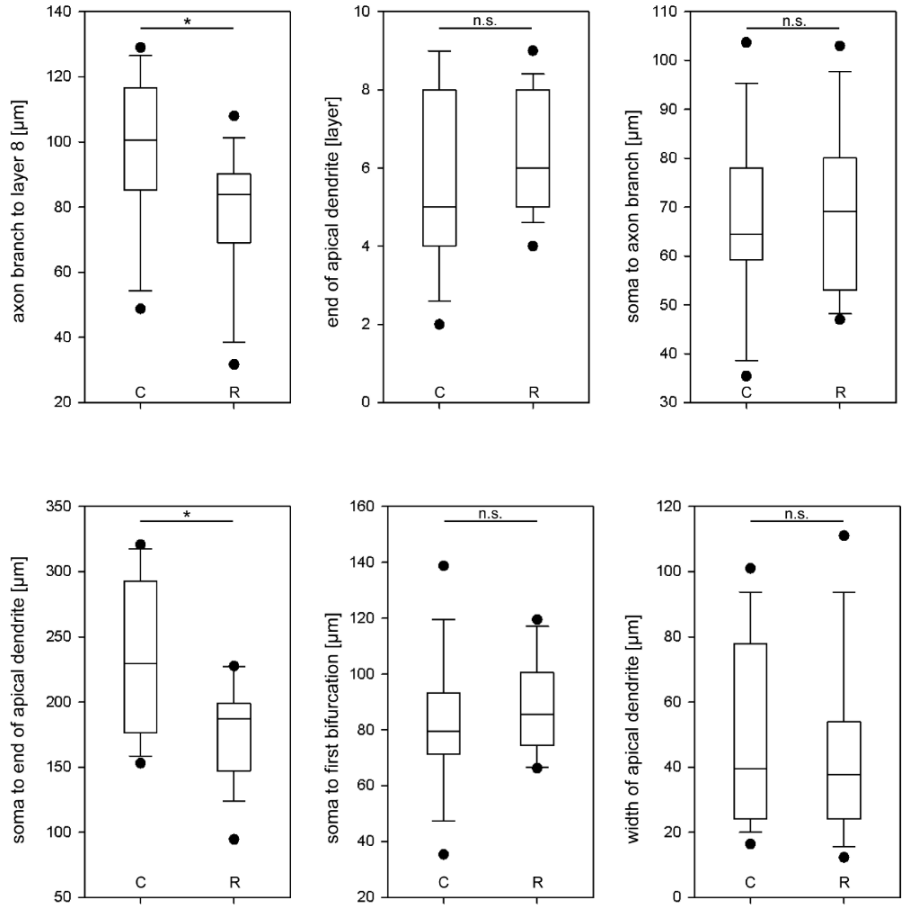

Figure 30. Morphological parameters of Shepherd's crook neurons in control and enucleated tecta
Six different parameters were measured and compared. There is a significant difference in the length of the soma location and the end of the apical dendrite between control and removal (d lower left). Furthermore, the length between the axon branch and the beginning of layer 8 is also significantly different (top left). The other parameters (length from the soma to the first bifurcation, length from the soma to the axon branch, layer in which the apical dendrite ends and width of the apical dendrite) are not significantly different. C: control. R: early eye removal. Statistical test: paired t-test. *: significant. n.s.: not significant. Figure reproduced from Lischka, Yan, Weigel, & Luksch, 2018, with permission from the publisher.

[25] Lischka, Yan, Weigel, & Luksch, 2018

Discussion

The paragraph ‘Expression patterns of structural proteins and ion channels in Shepherd’s crook neurons’ is modified from the Discussion section that corresponds to the following publication:

“Expression patterns of ion channels and structural proteins in a multimodal cell type of the avian optic tectum” (Lischka, Ladel et al., 2018)

The article is published in The Journal of Comparative Neurology, which permits authors the reproduction of published articles for dissertations without charge of further license.

- -

The paragraph ‘Influence of retinal innervation on Shepherd’s crook neurons’ is modified from the Discussion section that corresponds to the following publication:

“Effects of early eye removal on the morphology of a multisensory neuron in the chicken optic tectum” (Lischka, Yan et al., 2018)

The article is published in Brain Research, which permits authors the reproduction of published articles for dissertations without charge of further license.

Multisensory integration is crucial to recognize potential sources of danger earlier compared to the reaction to a single sensory cue (Stein et al., 2014). A spatial and temporal combination of two sensory (bimodal) cues can evoke enhanced or depressed responses compared to the unimodal presentation in cell types capable of multisensory integration (Stein & Stanford, 2008). The optic tectum is a brain region, where primary sensory information is processed. Different sensory modalities arrive at distinct layers and are processed to higher brain regions. *In vivo* recordings showed that the optic tectum is also a multimodal integrating structure (Knudsen, 1982; Maczko et al., 2006; Winkowski & Knudsen, 2007; Zahar, Reches, & Gutfreund, 2008). So far, it is not known, which neurons do integrate this multisensory information. The Shepherd´s crook neuron, first described in the early 20th century (Ramón y Cajal, 1909), is assumed to

integrate auditory and visual inputs. In this thesis, I used neuroanatomical, modelling, and electrophysiological methods to understand the integration of information and the information flow in Shepherd's crook neurons. I first discuss the single chapters and their special aspects independently. In a last chapter, I summarize my findings and discuss it in a broader context of multimodal integration and axopetal information flow.

Expression patterns of structural proteins and ion channels in Shepherd's crook neurons

"I first analyzed the location of structural proteins and ion channels known to play a significant role in the signal propagation of many neurons. SCNs and their morphology with the characteristic presumed axon origin were already described more than a century ago by Ramón y Cajal (1909). This morphology led him to assume that the soma is not involved in the propagation of visual input to the axon, which points to an alternative signal flow of nerve impulses (Triarhou, 2014). I was interested in a more detailed view of the morphology, in particular of the soma and the action potential generation site, to better understand the integration of dendritic input in SCNs."[26] Therefore, specific ion channels were chosen, which are known to be responsible for high repetitive and precisely timed firing as it is necessary for spatial and temporal integration of sensory information (Chatelier, Zhao, Bois, & Chahine, 2010; Royeck et al., 2008; Rush, Dib-Hajj, & Waxman, 2005; L.-Y. Wang, Gan, Forsythe, & Kaczmarek, 1998).
"To first confirm the proposed identity of the axon and the location of its origin, I used an antibody against NF200 to differentiate the axon. There are four neurofilament subunits (heavy, medium and light neurofilament, and α-internexin), but only the heavy neurofilament (NF 200) is highly abundant in the axon of different neurons (Yuan, Rao, Veeranna, & Nixon, 2012). By immunostaining NF200 and analyzing its localization in SCNs, I could corroborate the interpretation of Ramón y Cajal (1909) that the branching originating from the apical dendrite and projecting to the isthmic nuclei is the axon. Usually, action potentials are generated at the AIS that is mostly located near the transition of the soma and the axon (Gulledge & Bravo, 2016). As SCNs have a unique morphology with an axon branching at a more distal point on the apical dendrite and as the location of the AIS is critical for the question of information flow and integration, I studied the location of the action potential generation site by using an antibody against Ankyrin G. This protein is known to stabilize ion channels in the membrane at the AIS (Kole & Stuart, 2012). I found that the AIS in SCNs extends from the branching point of the axon from the apical dendrite up to 50 µm on the apical dendrite. By double labeling both structural

[26] Lischka, Ladel, Luksch, & Weigel, 2018

proteins, NF200 and Ankyrin G, no overlap between both markers was found indicating a separation of the AIS and the axon itself.

Ankyrin G stabilizes ion channels in the membrane (Kole & Stuart, 2012). For instance, other studies showed that Ankyrin G anchors voltage-gated sodium channel subtypes in the membrane of the AIS (Hedstrom, Ogawa, & Rasband, 2008; Kuba, Oichi, & Ohmori, 2010). To generate action potentials a dense expression of voltage-gated sodium channels (Na_v) in the AIS is required (Hodgkin & Huxley, 1952; Kole & Stuart, 2012), as they are essential for the excitation of neurons (Khaliq, Zayd, Gouwens, Nathan, & Raman, 2003). I found a high expression of sodium channels ($PanNa_v$) on the axon directly after the AIS. In a lower density, these ion channels are also abundant on the soma, the primary dendrite and the AIS. Three different sodium channel subtypes ($Na_v1.1$, $Na_v1.2$, $Na_v1.6$) have been identified to be localized in the AIS (Kole & Stuart, 2012). $Na_v1.6$ is the most prominent voltage-gated sodium channel in the nodes of Ranvier, the AISs and dendrites of the central nervous system (Caldwell et al., 2000). A dense expression of the voltage-gated sodium channel subtype $Na_v1.6$ in the AIS was already described for various neuron types (Purkinje neurons of mice: (Jenkins & Bennett, 2001; Kuba et al., 2014); neurons in the avian nucleus laminaris: (Kuba et al., 2014)). I was interested which subtype mainly contributes to the signal propagation in SCN. The immunohistological data suggest that $Na_v1.6$ is the dominant sodium channel expressed in SCNs. Nav1.6 was highly expressed on the axon distal to the axon initial segment, but weakly expressed on the AIS. This is a discrepancy to the expected expression pattern since it is often described that Ankyrin anchors sodium channels in the membrane of the AIS (Hedstrom et al., 2008; Kuba et al., 2012). A study by Palmer and Stuart (2006) showed an action potential initiation zone at the distal end of the AIS in pyramidal neurons in layer 5 of the rat cortex. This finding receives support by a theoretical study of Mainen, Joerges, Huguenard, and Sejnowski (1995) that showed that the distal site of the AIS is the favorite site for action potential initiation."[27] The authors explained this shifted AIS location by the large electric load of the soma and dendrites. The distal end of the AIS seemed to be shielded from this electrical sink as it is located nearby the myelinated region, which is assumed to have a high membrane resistance and low capacitance. "The increased sodium channel density near the distal end of the AIS in SCN suggests a similar action potential generation as in layer 5 pyramidal neurons (Palmer & Stuart, 2006). Other studies described also the expression of the subtype $Na_v1.2$ at the AIS (Hu et al., 2009; Lorincz & Nusser, 2010). However, I could not detect any specific fluorescence signal for this subtype with the tested

[27] Lischka, Ladel, Luksch, & Weigel, 2018

antibody against $Na_v1.2$ (data not shown). Probably this voltage-gated sodium channel is not expressed in the tectal layer 10 cell type at the tested age (between post hatch day 1 and 3). Data of the nucleus laminaris in chicken suggests that $Na_v1.2$ is only expressed until embryonic day 18 (Kuba et al., 2014).

Physiologically, $Na_v1.6$ controls the fast spiking activity in neurons. This sodium channel subtype contributes to a persistent Na^+ current and leads to a high precision of temporal firing (Khaliq, Zayd, et al., 2003; Osorio et al., 2010; Raman, Sprunger, Meisler, & Bean, 1997). A precise temporal firing should help to integrate and process both visual and auditory input simultaneously at the AIS and axon. It has been reported that dendritic sodium channels play a role in burst discharge. In pyramidal cells of weakly electric fish, they are also essential for synaptic plasticity of excitatory input to the dendrites (Clarke & Maler, 2017; Turner, Maler, Deerinck, Levinson, Rock, & Ellisman, 1994). In SCNs, I also found an expression of sodium channels on the primary dendrite, although at lower density. However, the expression of dendritic sodium channels in SCNs is not investigated in detail in this thesis and has to be clarified in the future.

Next to voltage-gated sodium channels, voltage-gated potassium channels are essential for the excitability by re- and hyperpolarization during action potentials. An interesting candidate for auditory and visual information processing in chicken is the channel subtype 3.1b. It enables repetitive firing at high frequencies in neurons (Rudy B, McBain CJ, 2001) and is necessary in temporal coding of auditory information in the chicken brainstem by action potential width reduction and the transmission of high frequency temporal information with little jitter (Parameshwaran et al., 2001; Parameshwaran-Iyer, Carr, & Perney, 2003; Perney & Kaczmarek, 1997; Wang et al., 1998). Moreover, all isthmic nuclei also express this K_v subtype (Wang et al., 2006). In SCNs, I found a high amount of $K_v3.1b$ channels on the soma, the primary dendrite and the beginning of the AIS. As SCNs are the only input neurons to the isthmic nuclei, this ion channel expression likely shows a precise temporal interaction between these neurons in the intermediate layer 10 of the TeO and their output, the isthmic nuclei. Both voltage-gated sodium and potassium channel subtypes point to a fast and highly precise signal processing in the SCN.

The propagation to the isthmic nuclei is eased by the myelination of the axon. The action potential generated in the AIS has to travel a long distance to the isthmic nuclei. Shao, Lai, Meyer, Luksch, and Wessel (2009) reported that neurons in the IPC respond to stimulation in layer 10 with fast and strong EPSPs (latency 7 to 10 ms).

Another voltage gated potassium channel which supports fast spiking is the subtype $K_v3.3$. In weakly electric fish, this subtype is mainly expressed on the soma and the dendrites and is complementary to $K_v3.1$ (Deng et al., 2005). In mice, some cell types co-express $K_v3.1$ and $K_v3.3$ with different expression patterns (Chang et al., 2007). It would be of interest to test whether $K_v3.3$ is present similarly on SCN but I found no suitable antiserum to test this proposition."[28]

To summarize the data, I confirmed that SCN possesses an axon-carrying apical dendrite. The origin of the axon at the first bifurcation of the apical dendrite leads to the characteristic Shepherd's crook appearance. This axon initial segment with a length of 92 to 115 µm is the only possible site of action potential generation. I also found ion channels that contribute to fast spiking with high frequencies. "Combining the detailed neuroanatomy with physiological data will help to further understand multisensory integration on the subcellular level."[29]

[28] Lischka, Ladel, Luksch, & Weigel, 2018
[29] Lischka, Ladel, Luksch, & Weigel, 2018

Multi-compartment model based on anatomical data

The parameters for the multi-compartment model were derived from the expression patterns of voltage-gated sodium and potassium ion channels and structural proteins combined with morphological parameters such as the length of soma and dendrites, distance between soma and axon branch, and axon initial segment location. The activation of the model was triggered by a stochastic distribution of input spikes. By using the multi-compartment model, I investigated the integration of auditory and visual information in SCNs.

In previous studies in birds and mammals, multisensory integrating cells were shown to respond stronger to the combination of two sensory inputs than to a single sensory input (Meredith & Stein, 1986; Stein et al., 2014; Zahar et al., 2008). The multi-compartment model was activated by stimuli mimicking visual, auditory, and audiovisual information. The highest average action potential rate was seen after the simultaneous activation of both the apical (mimicking of the incoming visual information) and basal (mimicking of the incoming auditory information) input regions. The increased action potential rate is evidence for the ability of Shepherd's crook neurons to integrate two different incoming sensory input.

Several studies showed that a temporally shifted presentation of two modalities produced a higher response. However, delayed presentation has to be aligned in a time window precisely timed. Variations of the delay resulted in increased or decreased responses (Meredith, Nemitz, & Stein, 1987; Reches & Gutfreund, 2008; Zahar et al., 2008). Physiologically this makes sense if the different latencies of visual and auditory signals from the sensory organs to important brain regions are taken into account. "For chicken, the latencies of visual and auditory inputs to tectal laminae have not been exactly determined. Motion stimuli evoke neural responses in the optic tectum after about 100 ms (Verhaal & Luksch, 2016b). In the barn owl, tectal cells in the intermediate and deep layers respond to visual stimuli, for example, looming dots, 120–150 ms after stimulus onset (Mysore, Asadollahi, & Knudsen, 2010). The delay for auditory stimuli has not been measured in chicken. In barn owls, auditory input is processed much faster than visual input. Auditory input was recorded in the inferior colliculus (IC) approximately 13 ms after stimulus onset (Spitzer, Bala, & Takahashi, 2004). Stimulation in the IC evokes responses in the intermediate layers of the optic tectum with a delay of 8–10 ms (DeBello & Knudsen, 2004). Due

to the retinal processing delay the visual signal reaches the midbrain about 100ms later than the auditory input, the precise tuning for integration of distinct sensory information has to take place in the midbrain."[30] Meredith and colleagues (1987) described the temporal factors which determining multisensory integration in an *in vivo* study in the cat superior colliculus. A maximal enhancement was found when the periods of peak activity of the unimodal stimuli overlapped rather than aligning the unimodal stimulus onset or response latencies (Meredith, Nemitz, & Stein, 1987). Thus, there is an optimal time window for multisensory enhancement, which depends on latencies and ongoing activity. I tested simultaneous and 100 ms delayed activation of apical and basal synaptic input regions. However, a pre-activation of one sensory input lead to no significant enhancement of the spiking response in the multi-compartment model. It is likely that a delay of 100 ms is not optimal for the cell to enhance its spike rate. So far, the delay of the incoming sensory information at the primary senses (photoreceptors, hair cells) to the Shepherd's crook neurons is not described. To show in how far the SCNs response is sensitive to different arrival times it is necessary to be tested with a wider range of delays *in silico* and verified *in vitro* or *in vivo*.

[30] Lischka, Ladel, Luksch, & Weigel, 2018

Plasmid construction, plasmid amplification and plasmid transfection in chicken embryos for GFP expression in layer 10 neurons

In addition to the immunohistology and the *in-silico* project, hybrid voltage sensor imaging studies were performed. The design of these experiments resembled the design of the multi-compartment model. In the imaging experiments, voltage sensitive fluorescence markers were used. In a first approach, I used genetically expressed fluorescent proteins (GFP) as electron donor.

Genetic manipulation of cell types in the nervous system is a common tool to study different research topics like detailed neuroanatomy, cell-cell interaction, neural activity of single cells or networks. In chicken embryos, *in ovo* electroporation is a widely used technique to manipulate cells or brain regions with plasmids (Funahashi et al., 1999; Muramatsu, Mizutani, Ohmori, & Okumura, 1997; Nakamura et al., 2000). Plasmids encoding specific genes, which are expected to be expressed in neuronal cells, are introduced by electric pulses to cause pores in the cell membrane and allow the uptake of the plasmid DNA. The DNA is further expressed in the cell for instance by knocking down genes or expressing fluorescent dyes. In this study, the aim was to produce chicken embryos with GFP-encoding tectal neurons in layer 10 to image the activity after electrical stimulation with FRET (Chanda et al., 2005; Fink et al., 2012; Wang et al., 2010). The genetic prelabeling of the cells should replace the time-consuming labeling of single neurons with a fluorescent voltage sensor.

One approach was based on the cellular development of the optic tectum (Grace Gray & Sanes, 1991). The specific stratification of the chicken optic tectum develops in three migratory waves. In the first wave, the deeper layers start to develop (between E3 and E5). In the second wave, the superficial layers develop (between E4 and E7) and in the third wave the intermediate layers start to develop (between E6 and E8; LaVail & Cowan, 1971; Nakamura & Sugiyama, 2004). In previous studies, transfection at E3 and E4 labels neuronal cells in layer 13 to 15, while after transfection at E5 neuronal cells in layer 4 to 10 and at E6 predominantly neuronal cells in layer 10 are intensely labeled (Fedtsova, Quina, Wang, & Turner, 2008). Four different developmental

stages for the transfection of the embryo with a GFP-encoding plasmid were chosen (E2, E3, E4, and E5) to evaluate the expression pattern of GFP. A slightly different expression pattern was visible between transfections at E2 and E3. While at E2 eGFP expression in deeper layers was dominating, more neurons in the superficial layers were labelled at E3. However, the exclusive transfection of layer 10 neurons at one of these developmental days was not possible. While animals transfected in E2 and E3 survived well and yielded labeled neurons, most embryos died when transfected at E4 and E5. A probable reason is related to handling issues. At day 2 the embryo is in the so-called hammer-head stage in which the three brain vesicles are very prominent (HH11). At day 4 the embryo already started to turn its whole body. Because of the body movement the access to the mesencephalon is easier at developmental day 2 than at developmental day 4 or 5. Moreover, the amnion started to grow around the embryo at HH11 and the head capsule starts to develop at E3, which constitutes an additional barrier to inject the GFP-encoding vectors in the vesicles with a fine glass capillary at later stages. Also, the distance between the electrodes and thus the conductance is difficult to control at later stages. A greater distance between the anode and cathode results in lower transfection efficiency (Nakamura & Funahashi, 2001). Furthermore, the blood vessels start to extend on E3. The risk to injure blood vessels is high and can lead to serious damage of the embryo during electroporation.

The second approach made use of different promotors (CMV, βactin, CAG), which controlled the GFP expression of the plasmids. Different promoters affect the intensity of GFP expression (Yang et al., 2014). Injection of the three different plasmid types resulted in GFP-expressing cells in the optic tectum. There was no preference for one plasmid type in this brain region. The transfection with each of the three plasmids resulted in a bright GFP expression in multiple cells in the layered tectal structure. Nevertheless, the transfection efficiency was generally low and unspecific for the three different plasmids. In summary, specific transfection control was not achieved with either approach.

To specifically express GFP in SCN, I propose sequencing the genome. Modern techniques like single cell sequencing (e.g. with single cell RNA sequencing scRNAseq) allow to identify cell specific markers (e.g. promoter, transcription factor) (Zeng & Sanes, 2017). Specific cell markers could be used to establish stable transgenic lines for anatomical and electrophysiological approaches or to generate plasmids encoding cell-specific promoters. For instance in zebrafish, various stable transgenic lines with reproduceable patterns of transgene expression are established even for tectal cells (Förster et al., 2017; Higashijima, 2008; Preuss, Trivedi, Vom

Berg-Maurer, Ryu, & Bollmann, 2014; Stuart, Vielkind, McMurray, & Westerfield, 1990). In transgenic animals the targeting of the gene-of-interest on a single animal basis is omitted. Here, cell types of interest are directly labelled under the control of a specific promoter (Liu, 2013). Potential markers that are known to be expressed in the optic tectum and layer 10 are Brn3a (Fedtsova et al., 2008) and Ap-2δ (Hesse et al., 2011), respectively. Brn3a belongs to the Brn3 family of POU-domain transcription factors. It plays an important role in differentiation, survival, and axonal elongation during the development of retinal ganglion cells in mice (S. Wang et al., 2002). It is often used as marker for retinal ganglion cells. In mice, it has been shown that Brn3a is specifically expressed by retinal ganglion cells projecting to the contralateral superior colliculus (Quina et al., 2005). Colocalization studies of Brn3a and Shepherd's crook neurons revealed that this transcription factor is also present in SCN (Kretzinger, 2008). Another candidate for a specific marker belongs to the transcription factor family Ap-2. This transcription factor is involved during development, differentiation, and tumorigenesis. The Ap-2 family contains 5 genes which encode for five distinct proteins (Eckert, Buhl, Weber, Jäger, & Schorle, 2005). Ap-2δ is almost exclusively expressed in the midbrain but was also found in lower levels in the diencephalon, forebrain, spinal cord, and the retina, and for a short period in the developing heart (Hesse et al., 2011). The analysis of the Ap-2δ midbrain expression in chicken embryos showed a colocalization of the transcription factor with Shepherd's crook neurons in a certain time window in development (Schaub, 2018). The identification of these two candidates for specific markers for Shepherd's crook neurons in the chicken optic tectum provide an option to generate more specific plasmids in future projects.

The '*in ovo* electroporation' method still proves to be difficult in respect to the accuracy of DNA incorporation in the desired brain region. Viability of electroporation in embryos is low, since current amplitudes necessary to succeed may be harmful to the embryo (Momose et al., 1999). I tested several parameters to increase the survival rate of the embryos. Disinfection of the breeder before incubation with Kohrsolin, a germicide with a broad spectrum of activity, enhanced the survival rate by more than 50 %. To optimize the efficiency of the '*in ovo* electroporation' method, Momose et al. (1999) developed the 'microelectroporation' method. This method allowed a higher survival rate and transfection efficiency due to locally precise application of the electric field with lower applied voltages. In preliminary studies in our lab, a significant higher survival rate and transfection efficiency was confirmed by *in ovo* electroporating GFP-encoding plasmids in the second vesicle (Ballmann, 2018; see Figure 3E in Momose et al., 1999). However, transfection specificity did not depend on survival rates.

To overcome problems of electroporation, incorporation of GFP-encoding vector into the DNA with viral vector (e.g. retroviruses) would be ideal (Davidson et al., 2000; Matsui, Tanabe, Watanabe, & Balaban, 2012). I tested different serotypes of recombinant adeno-associated viral vectors. None of the vectors resulted in eGFP expressing neurons in the chicken midbrain. AAVs contain specific gene sequences, which will be integrated in the genome and expressed from these vector-containing cells. Adenovirus cell entry and intracellular translocation require interaction of viral proteins with host proteins to elicit specific signaling (Medina-Kauwe, 2003). This lock-and-key mechanism is highly specific. I assumed that the chicken cell receptor and the viral vector (AAV2) are not compatible in the cells in the chicken midbrain. This assumption is based on the amino acid sequence alignment of murine and chicken HSPG receptor. Matsui et al. (2012) reported that viral vectors of serotype 2 (AAV2) cannot transfer genes in chicken neuronal cells. They claimed a different viral vector to be able to transfer genes in avian cells, called avian adeno-associated vector (A3V, see also Bossis & Chiorini, 2003). Nevertheless, the cell type specificity of GFP expression is determined by the promoter and/or viral tropism in this avian-associated viral vector (Matsui et al., 2012). A3V could be promising for the use of viral vectors to transfect tectal neurons in chicken embryos.

After time-consuming, but inefficacious testing of various approaches to achieve the goal of specifically labelled neurons in layer 10 of the optic tectum, the method for the following hybrid voltage sensor imaging experiments was changed. Neurons were directly labeled with a patch clamp electrode with DiO immediately before signal recording.

Signal propagation in Shepherd's crook neurons after visual and auditory stimulation

Shepherd's crook neurons project to each of the three isthmic nuclei and synchronize the enhancing and suppressive mechanism in this network (Garrido-Charad et al., 2018; Goddard et al., 2014; Lai et al., 2011; Marín et al., 2005; Meyer et al., 2008; Y. Wang et al., 2006). Maczko et al. (2006) studied the responsiveness of the isthmic nuclei to unisensory stimuli. Visual and auditory input evoked responses in neuronal units in the isthmic nuclei. The isthmic nuclei receive only input from the SCNs. Based on the ability of the isthmic nuclei to respond to visual and auditory information, I examined whether SCNs also respond to visual and auditory input and how these inputs are processed in SCNs.

In order to study the spatiotemporal activity pattern, I used hybrid voltage sensor imaging, an optical imaging method. This method was applied to record action potentials and their propagation in neurons in cell culture and slice preparations with high temporal fidelity (Bradley, Luo, Otis, & DiGregorio, 2009; Chanda et al., 2005; Fink et al., 2012). This method uses Förster resonance energy transfer (Fernandez, Taylor, & Bezanilla, 1983; Jesús González & Tsien, 1995; Jesus González & Tsien, 1997) which leads to a high voltage sensitivity within the physiological most relevant range of membrane potentials. Two components function as electron donor (DiO) and electron acceptor (DPA), respectively. The electron donor was applied to the cell membrane of single neurons via a patch electrode, while the electron acceptor was bath applied before and during the experiments. DPA is voltage-sensitive and moves between the inner and outer cell membrane layers according to changes in membrane voltage (Cohen et al., 1974; Honig & Hume, 1989; Wu, Russell, Nguyen, & Karten, 2003). During resting potential state, the electron acceptor is located at the outer cell membrane. While changing from resting potential to depolarization in neurons, the electron acceptor moves with the negatively charged ions and stays in the inner cell membrane as long as depolarization is maintained (Chanda et al., 2005). The electron donor in our experiments is assumed to be anchored in the inner cell membrane. The jump of the electron acceptor from the outer to the inner membrane causes an electron uptake from the fluorescent electron donor, which reduces the fluorescence intensity of the fluorophore. The temporal resolution of the measurable intensity change is comparable to

patch clamp recordings (Fernandez et al., 1983; Chanda et al., 2005; Bradley et al., 2009; Voll, 2015). This method allows recording with high temporal resolution of cell activity and additionally a high spatial resolution of the activity in the whole cell.

However, optical methods have some technical limits. The presence of DPA can perturb the excitability by adding capacitance to the membrane (Bradley et al., 2009; Sjulson & Miesenböck, 2007, 2008). Patch experiments in our lab also showed a concentration dependent effect on the capacitance (Voll, 2015). I used DPA in an uncritical concentration, thus, negative effects should be minimized but cannot excluded completely. A promising alternative quencher is D3, which was developed and is currently tested in the University of Bonn (LIFE & BRAIN Center, Therese Alich, personal communication). This quencher seems not to affect the membrane capacitance.

Available cameras for hybrid voltage sensor imaging balance between spatial resolution, temporal resolution and sensitivity. Usually two parameters are optimized with the acceptance of a quality loss in the third parameter. For the hybrid voltage sensor imaging experiments a very sensitive charge-coupled device (CCD) camera with a high temporal resolution was used, but with a low spatial resolution of 80x80 pixels with a pixel size auf ~4µm^2. Thus, the spatial resolution is limited by optical scattering of the emitted fluorescence (Orbach & Cohen, Lawrence, B., 1983). This leads to a loss of signal-to-noise ratio of the cell activity on fine dendritic and axonal structures. Also, EPSPs are not detectable as the change of membrane potential evoked by these events was too weak. Therefore, only super-threshold cell activity and signal propagation on the primary dendrite and soma could be measured in this study.

To mimic visual and auditory input to the optic tectum, two custom-made stimulation electrodes were positioned in the corresponding layers. In such an artificial situation, electrical stimulation can only roughly imitate natural stimuli. For example, the number and intensity of retinal ganglion cell (RGC) activation and, thus, the postsynaptic activity in the SNC through this kind of stimulation depended on the position of the electrode relative to the synaptic endings and the SCN. In birds, 20 types of retinal ganglion cells are described so far that terminate in the retinorecipient layers of the TeO (Yamagata et al., 2006). To drive the activity in SCNs, it may be possible that only a certain number or type of RGCs need to be active. Also, it is likely that the optimal activation of a dendrite depends on the temporal and spatial summation of the incoming signal. By stimulating in the superficial layers, I was neither able to control the activation of specific types nor the activation of the same types of RGCs in different brain slices. This means that the amount of activated RGCs varies across brain slices and I had to adapt stimuli intensities in every experiment.

The chicken is an auditory generalist and it is not clear to what extent auditory processing in the optic tectum is relevant in this species. However, Verhaal and Luksch (2016a) showed that even chicken benefit from multimodal integration. In the barn owl, an auditory specialist, the neurons in the tectum form a map of auditory space. The auditory map is superimposed on the visual map (Knudsen, 1982). In the owl, neurons have precisely defined receptive fields for auditory and visual stimuli emerging from a specific spatial location in the environment. Based on these findings, Niederleitner et al. (2016) analysed the auditory projection to the chicken optic tectum in more detail. In this study, a relay nucleus (FRLx) was described that establishes an additional auditory projection to the optic tectum besides the auditory inputs from the inferior colliculus. The study also showed that the projections from FRLx passed through layer 13 and extended up to layer 10 of the optic tectum. Following Niederleitner et al. (2016), different positions in the external part of the IC, the FRLx and layer 13 of the optic tectum were tested as stimulation sites for the activation of SCNs. The stimulation of the external part of the IC and the FRLx resulted in no reliable results to evoke activity in Shepherd's crook neurons (G. Huang, 2017) presumably due to cut connections or activation of neurons projecting to other parts of the TeO. Therefore, in this study the auditory activation was mimicked by a stimulation electrode positioned in layer 13 of the optic tectum. In summary, an electrical stimulation in the superficial (layer 2 to 4) lead to spiking activity in Shepherd's crook neurons and simulated the incoming visual signal as well as an electrical stimulation in the deep layer (layer 13) lead to spiking activity in SCNs and simulated the incoming auditory signal. To exclude direct stimulation I blocked the synaptic transmission with calcium free ringer in a set of experiments. This is in line with measured latencies and pharmacological data of patch clamp experiments in SCNs (Huang, 2017).

The process of combining visual and auditory signals in neurons is named audiovisual integration. That means that an organism integrates visual and auditory information with the requirement that the output of a stimulus combination is different from the response to each stimulus alone (Stein et al., 2014). The combination of visual and auditory stimuli helps the organism to perform saliency mapping in bimodal environments (Hazan, Kra, Yarin, Wagner, & Gutfreund, 2015). In behavioral studies, Verhaal and Luksch (2016a) showed that adult chicken are able to combine visual and auditory information to better detect stimuli, especially when the stimuli were weak.

In this thesis, I saw first evidence for multisensory enhancement in the multicompartment model after simultaneous activation of visual and auditory input regions. My hVOS experiments showed that Shepherd's crook neurons propagate visual and auditory input in the optic tectum. For linear

(additive) integration, I expected that the output of visual and auditory stimulation was the sum of both individual outputs (visual and auditory alone). For non-linear (sub- or super-additive) integration, the output was expected to be different from the sum and for super-enhanced integration the expectation was that the output is much higher than visual and auditory output alone. The multi-compartment model based on neuroanatomical data of SCN already showed with this simple activation paradigm that SCNs respond stronger to double stimulation of apical and basal dendritic regions than to single stimulation of one dendritic input region. A combined audiovisual stimulation in hVOS experiments resulted in a more robust response with a shortened latency. The enhancement was not greater than the sum of the visual and auditory activity, suggesting sub-additive integration. However, data were not significant and, in contrast to the multicompartment model, were only recorded at the soma. In contrast, Meredith and Barry Stein (1986) showed that the combined presentation of visual and auditory input in the cat superior colliculus lead to a super-enhancement, i.e. non-linear integration. Meredith and Barry Stein (1986, see also Stanford, Quessy, & Stein, 2005) also showed that simultaneous presentation of weak stimuli evoked a stronger response than the simultaneous presentation of stimuli which already evoke the strongest response when they are presented alone. This phenomenon was called 'inverse effectiveness'. This phenomenon was also discussed by Holmes and Spence (2005). Superadditivity can only be achieved by the weakest unimodal inputs. In the imaging experiments, the strength of stimulation was chosen in a way that an action potential was reliable evoked. Subthreshold responses cannot be recorded with hVOS. Maybe a response of one or two action potentials is the maximal response that can be evoked in SCNs *in vitro*. Thus, only a slight increase due to simultaneous can be expected. If I had used subthreshold stimuli, the combined stimulation at two distinct input regions may have evoked response in a more super-additive manner. Results of whole-cell recordings revealed an enhanced action potential firing after the simultaneous presentation of two subthreshold stimuli at the apical and basal dendrite (Huang, 2017). Taking all data of SCN into account I suggest that cue combination takes places in SCN for instance to align or associate cues from different modalities. However, recordings were performed only at the soma far away from the site of action potential initiation. Thus, the output of SCN may diverge from the somatic recording. I suggest *in vivo* recordings in postsynaptic neurons of the isthmic nuclei to finally answer the question of the amount of multisensory enhancement in the SCN.

The signal spread starting on the primary dendrite and moving on to the soma was independent of the activated stimulation site (visual, auditory, audiovisual). The directed signal propagation also confirmed the location of the axon initial segment already shown by the neuroanatomical

data. As I had no data regarding the signal propagation on the axon, I was not able to evaluate the signal propagation on the axon of SCNs. Most likely, the propagation recorded in this study is a backpropagation from the action potential generation site to the soma passing the primary dendrite. This is supporting the hypothesis of axopetal information flow as proposed by (Ramón y Cajal, 1909). The possible role of this information flow will be discussed later.

Effect of missing retinal innervation on the development of Shepherd's crook neurons

---

This paragraph 'Influence of missing retinal innervation on development of Shepherd's crook neurons' is modified from the Discussion section that corresponds to the following publication:

"Effects of early eye removal on the morphology of a multisensory neuron in the chicken optic tectum" (Lischka, Yan et al., 2018)

The article is published in Brain Research, which permits authors the reproduction of published articles for dissertations without charge or further license.

"The development of the nervous system including outgrowth and synaptic pruning strongly depends on a complex interplay of cellular and molecular mechanisms (Nakamura & Sugiyama, 2004; Watanabe et al., 2018; Watanabe & Yaginuma, 2015). One key factor is the sensory input (Wallace & Stein, 1997). Without sensory input, networks are not established, and synaptic pruning is reduced (Chechik, Meilijson, & Ruppin, 1999; Low & Cheng, 2006). Other studies in the optic tectum showed that missing retinal input leads to a reduction of the tectal thickness (Fujiwara, Ohozone, & Naito, 2000; Kelly, James, & Cowan, 1972) and changes the dendritic morphology of neurons in the retinorecipient layers (Luksch & Poll, 2002)."[31] Since the Shepherd´s crook neurons receive retinal input at distinct dendrites, I was interested whether and how retinal deafferentation affects the neuron as whole or only these retinorecipient dendrites. "I confirmed the reduction of the thickness of the retinorecipient layers demonstrated by Kelly and Cowan (1972) and could also corroborate that the clearly discernible structure of layers 6, 7 and 8 is lost upon deafferentation and appears diffuse and not distinguishable anymore, probably due to a major reduction of layer 7. Interestingly, the major reduction of retinorecipient layers is caused by reduction of layer 1 – 5. In layer 5 horizontal cells are localized which are presumably in direct contact to the projections from the retina (Luksch & Golz, 2003). I showed a reduction of layer 5 thickness by an anti-calbindin staining after early

[31] Lischka, Yan, Weigel, & Luksch, 2018

eye removal. Calbindin is expressed in a subpopulation of layer 5 cells (chicken: Luksch & Golz, 2003; zebra finch: Heyers, Manns, Luksch, Güntürkün, & Mouritsen, 2008). Moreover, in layer 5 the characteristic bottlebrush dendritic endings of SGC cell dendrites are located. Luksch and Poll (2002) found these endings to be deformed after early eye removal, which probably contributes to the overall reduction of layer 5. Additionally, layers 1 – 4 are also remarkably thinner.

The gross morphology of Shepherd's crook neurons (e.g. position of neuron, soma size, location of axon origin) was not altered by retinal deafferentation. This is not surprising, considering the ontogenesis of the optic tectum. The migration of SCN precursor cells is finished at embryonic day 10 and the gross morphology has been established (Domesick & Morest, 1977). Ingrowth of retinal projection to the superficial layers starts not before embryonic day 12 (LaVail & Cowan, 1971; Scicolone et al., 2006). Reduction of the length of the apical dendrite and of the distance from the axon branch to layer 8 is likely a phenomenon of the overall layer thickness reduction, and not an alteration in the growth of apical dendrites. However, the fine structures of the apical dendrites, such as dendritic branching pattern and dendritic endings, are less pronounced after early eye anlagen removal.

This developmental change seems to be caused by the lack of retinal innervation since branching of the basal dendrites is not affected. For the development of the fine dendritic structures at the apical dendrite additional cues such as patterned sensory input is required which induce further differentiation (Wong & Ghosh, 2002). To establish a functional network, neuronal activity of other neurons is required for precise synaptogenesis (Miller & Kaplan, 2003). Thus, the changes in apical dendritic morphology are likely caused by the missing retinal input."[32] My data confirm that apical dendrites of SCN are receiving retinal inputs. "Furthermore, I showed that, even with deafferentation of one sensory input, multimodal cells still retain the anatomical requirement to receive other sensory inputs."[33]

[32] Lischka, Yan, Weigel, & Luksch, 2018
[33] Lischka, Yan, Weigel, & Luksch, 2018

General discussion and conclusion

My thesis focused on the processing of visual and auditory information in a particular neuron, the Shepherd´s crook neuron (SCN), located in the intermediate layers of the chicken optic tectum. The avian optic tectum is comparable with the mammalian superior colliculus or optic tectum in other vertebrate groups as it is similar in structure, retinotopic map formation and functions. Although there is a diversity among these animal groups, the optic tectum has a common feature: the processing of sensory information. In nature, an incident is usually not only accompanied by a single sensory signature such as, e.g., visual or auditory. A combined integration of different unisensory information, called multimodal integration, enables the animal to react faster and more reliable (Corneil, van Wanrooij, Munoz, & van Opstal, 2002; Stein & Meredith, 1994; Verhaal & Luksch, 2016a). How different sensory input is processed in the dendritic tree of an individual neuron is however not known so far. In order to answer this, I first investigated the morphology of the neuron in great detail. This allowed me to build a multicompartment model together with Thomas Künzel (RWTH Aachen). In this model and in accompanying in-vitro imaging experiments, I then investigated how SCN react to stimulation of both dendritic areas alone mimicking visual and auditory input and in combination mimicking bimodal stimulation.

According to several studies, multisensory integration is based on three general principles. First, the visual and the auditory components have to be aligned in space (Jiang, Jiang, & Stein, 2002; Stein, Meredith, Huneycutt, & McDade, 1989; Stein, Huneycutt, & Meredith, 1988). Second, the visual and auditory components had to be aligned in time (Corneil et al., 2002; Meredith & Stein, 1986, Meredith, Nemitz, & Stein, 1987). Third, the likelihood of multisensory facilitation is increased, when uni-sensory components are presented with low amplitudes (Stein & Meredith, 1994). Multisensory facilitation means the facilitated processing of one sensory input when another sensory input is present at the same time. Multisensory integration may also lead to signal depression.

In my thesis, I performed electrophysiological experiments on brain slices. A brain slice preparation is quite artificial. An alignment in space and time was achieved by the positioning of the stimulation electrodes in the topographically organized OT and the temporal control of the presentation of an electrical stimulus by the stimulus generator equipment and software. However, a single electric pulse differs from a naturalistic scene. Nevertheless, I could show that

SCN respond to each unimodal stimulus and to a combination of both. Here, I expected a super-enhancement of the combined signal as it was shown by Meredith and Stein (1986). However, regarding the number of spikes evoked by the stimulation paradigms, I recorded a sub-additive response at the soma. From those hVOS data, I conclude that bimodal stimuli lead at least to a more reliable response. However, I could not record at the axon beyond the spike initiation zone. The multi compartment model, which is based on the morphology and ion channel composition of SCN, showed an even higher spike rate on the axon to audiovisual stimulation compared to each modality alone, which conforms to the definition of super-enhancement. Since it is not possible to verify this by *in vitro* optical imaging or patch-clamp, recording the activity of postsynaptic neurons in the isthmic system *in vitro* or *in vivo* might be a possibility to see effects like super-enhancement.

Timing in multisensory enhancement in SCN is an interesting point. Multisensory enhancement usually considers the simultaneous presentation of two sensory stimuli. Zahar et al. (2008) termed this a somewhat paradoxical result. They argued that in natural situations the peak activity of collicular neurons are rarely temporally aligned. They showed that the synchronization of visual and auditory stimuli elicited desynchronized tectal activity and redefined the alignment hypothesis to that a bimodal response underlies a time window of integration (see also Stein & Meredith, 1994). In Shepherd's crook neurons, this is likely to be the case, too. In general, it is known that the visual signal is processed slower than the auditory signal in the nervous system. The visual signal reaches the midbrain estimated 80 to 100 ms later that the auditory input. On the other hand, light travels faster (300000000 m/s) through the air than sound (330 m/s) when looking at it from a physical context. Therefore, the optimal window in which two senses evoke stronger responses than one sense has to take in account the physical and neural properties of light and sound travel times (Vroomen & Keetels, 2010). The different nature of the sensory information makes a restriction to an optimal window of a few milliseconds implausible. The different physical travel velocities have a high impact in natural scenes and the compensation of target distances (King, 2005). Imagine a predator in different distances to a chicken: A distance of 30 meters would result in a delayed auditory perception of about 90 ms, which than would coincident at the tectum with the visual information. Shorter distances would lead to a preceeding auditory input in the tectum but to a maximum of about 80 to 100ms. The question therefore arises whether and, if yes, where neural processing delays are counterbalanced. The particular morphology of SCN may play a role here. It might be that the longer travelling distance of basal input to the AIS is used to equalize different velocities in presynaptic processes. The axon origin on the apical dendrite, thus, might introduce a short delay for the faster auditory

signal to synchronize multisensory information in this cell type. However, neither my physiological data do point into that direction because of lower latencies if the basal dendrite was stimulated nor the idea of a relatively wide window of temporal integration fits to a delay line in SCN. I also tested a delay of 100 ms in the multicompartment model, which did not lead to an enhanced response. However, 100 ms might too long to be sensible for SCN. Thus, different response delays to visual and auditory stimuli should be tested in further *in vitro* or *in vivo* recordings. In preliminary data of the multi-compartment model, it is shown that at shorter audiovisual delays the response rate increases and is even more increased when the basal stimulation site is active before the apical stimulation site.

The axon origin at the apical dendrite is a particularity of the SCN. If it does not play a role in delaying signals, what are other plausible roles? I showed that action potentials are generated at the axon origin by immunohistological and physiological approaches confirming the axopetal information flow. Incoming visual input can thus directly excite the axon without passing the soma as proposed in the concept of axopetal information flow by Ramón y Cajal ((1909); see also: (Häusser et al., 1995; Thome et al., 2014; Triarhou, 2014)). In dopaminergic neurons in the substantia nigra in rats, recordings showed that the axon branching off the dendrite experiences the action potential before the soma. The final site of synaptic integration in these neurons will take place rather in the dendritic region prior to the axon than in the soma (Häusser et al., 1995). In SCN cells, incoming auditory information passes the soma on the way to the AIS. The faster auditory signal can predepolarize the soma and the primary dendrite and, thus, can modulate the gain of the neuron for the visual input as shown for neurons in the visual cortex of cats (Cardin, Kumbhani, Contreras, & Palmer, 2010; Cardin, Palmer, & Contreras, 2007; Melonakos, White, & Fernandez, 2016). By this, the visual signal might be detected faster and more reliably. This can only be tested by correlating the output of SCN with their activation.

A particular type of CA1 pyramidal neurons in the hippocampus of mice have axons that frequently originate at a basal dendrite. Those axon carrying dendrites were more efficient in eliciting action potentials compared to regular basal dendrites. This seems to be caused by a lower activation threshold for action potentials and higher intrinsic excitability leading to a higher probability for evoking action potentials (Thome et al., 2014). Another issue, which can arise by action potentials generated far away from the soma on axon-carrying dendrites, are effects due to backpropagation. This might lead to a refractory period influencing the following responses. The coincidence of backpropagating action potentials with incoming synaptic inputs might have an important implication for precise timing of action potential initiation.

In summary, in my thesis I was able to resolve questions and confirm hypothesis regarding the cellular morphology, molecular localization, sensory information processing, and the ability of multimodal integration in this bimodal cell type. Other questions, such as the detailed physiological role of the axon carrying dendrite and function of axopetal information flow in SCNs, remain unresolved. However, these questions are amenable to investigation with both the modeling and the in-vitro preparation established here.

References

Anderson, L. L., Hawkins, N. A., Thompson, C. H., Kearney, J. A., & George, A. L. (2017). Unexpected Efficacy of a Novel Sodium Channel Modulator in Dravet Syndrome. *Scientific Reports*, *7*(1), 1682. https://doi.org/10.1038/s41598-017-01851-9

Aschauer, D. F., Kreuz, S., Rumpel, S., & Qiu, J. (2013). Analysis of Transduction Efficiency, Tropism and Axonal Transport of AAV Serotypes 1, 2, 5, 6, 8 and 9 in the Mouse Brain. *PLoS ONE*, *8*(9), e76310. https://doi.org/10.1371/journal.pone.0076310

Ballmann, M. (2018). Neuronale Netzwerkanalyse In ovo Mikroelektroporation bei Gallus gallus (research internship). Technical University of Munich.

Barkovich, A. J., Millen, K. J., & Dobyns, W. B. (2009). A developmental and genetic classification for midbrain-hindbrain malformations. *Brain: a Journal of Neurology*, *132*(12), 3199–3230. https://doi.org/10.1093/brain/awp247

Benowitz, Larry, I., & Karten, Harvey. Organization of the tectofugal visual pathway in the pigeon: A retrograde transport study. *The Journal of Comparative Neurology*, *167*, 503–520.

Bossis, I., & Chiorini, J. A. (2003). Cloning of an Avian Adeno-Associated Virus (AAAV) and Generation of Recombinant AAAV Particles. *Journal of Virology*, *77*(12), 6799–6810. https://doi.org/10.1128/JVI.77.12.6799-6810.2003

Bradley, J., Luo, R., Otis, T., & DiGregorio, D. (2009). Submillisecond Optical Reporting of Membrane Potential In Situ Using a Neuronal Tracer Dye. *Journal of Neuroscience*, *29*(29), 9197–9209. https://doi.org/10.1523/JNEUROSCI.1240-09.2009

Burger, C., Gorbatyuk, O. S., Velardo, M. J., Peden, C. S., Williams, P., Zolotukhin, S., Muzyczka, N. (2004). Recombinant AAV viral vectors pseudotyped with viral capsids from serotypes 1, 2, and 5 display differential efficiency and cell tropism after delivery to different regions of the central nervous system. *Molecular Therapy: the Journal of the American Society of Gene Therapy*, *10*(2), 302–317. https://doi.org/10.1016/j.ymthe.2004.05.024

Caldwell, J. H., Schaller, K. L., Lasher, R. S., Peles, E., & Levinson, S. R. (2000). Sodium channel Na(v)1.6 is localized at nodes of ranvier, dendrites, and synapses. *Proceedings of the National Academy of Sciences of the United States of America*, *97*(10), 5616–5620. https://doi.org/10.1073/pnas.090034797

Cardin, J. A., Kumbhani, R. D., Contreras, D., & Palmer, Larry. (2010). Cellular mechanisms of temporal sensitivity in visual cortex neurons. *The Journal of Neuroscience: the Official Journal of the Society for Neuroscience*, *30*(10), 3652–3662. https://doi.org/10.1523/JNEUROSCI.5279-09.2010

Cardin, J. A., Palmer, Larry, & Contreras, D. (2007). Stimulus feature selectivity in excitatory and inhibitory neurons in primary visual cortex. *The Journal of Neuroscience: the Official Journal of the Society for Neuroscience*, *27*(39), 10333–10344. https://doi.org/10.1523/JNEUROSCI.1692-07.2007

Chanda, B., Blunck, R., Faria, L. C., Schweizer, F. E., Mody, I., & Bezanilla, F. (2005). A hybrid approach to measuring electrical activity in genetically specified neurons. *Nature Neuroscience*, *8*(11), 1619–1626. https://doi.org/10.1038/nn1558

Chang, S. Y., Zagha, E., Kwon, E., Ozaita, A., Bobik, M., Martone, M. E., . . . Rudy, B. (2007). Distribution of Kv3.3 potassium channel subunits in distinct neuronal populations of mouse brain. *The Journal of Comparative Neurology*, *502*(6), 953–972. https://doi.org/10.1002/cne.21353

Chatelier, A., Zhao, J., Bois, P., & Chahine, M. (2010). Biophysical characterisation of the persistent sodium current of the Nav1.6 neuronal sodium channel: A single-channel analysis. *Pflugers Archiv: European Journal of Physiology*, *460*(1), 77–86. https://doi.org/10.1007/s00424-010-0801-9

Chechik, G., Meilijson, I., & Ruppin, E. (1999). Neuronal Regulation: A Mechanism for Synaptic Pruning During Brain Maturation. *Neural Computation*, *11*(8), 2061–2080. https://doi.org/10.1162/089976699300016089

Clarke, S. E., & Maler, L. (2017). Feedback Synthesizes Neural Codes for Motion. *Current Biology: CB*, *27*(9), 1356–1361. https://doi.org/10.1016/j.cub.2017.03.068

Cohen, L., Salzberg, B. M., Davila, H. V., Ross, W. N., Landowne, D., Waggoner, A. S., & Wang, C. (1974). Changes in axon fluorescence during activity: Molecular probes of membrane potential. *The Journal of Membrane Biology*, *19*(1), 1–36. https://doi.org/10.1007/BF01869968

Constantine-Paton, M. (1990). Patterned Activity, Synaptic Convergence, And The NMDA Receptor In Developing Visual Pathways. *Annual Review of Neuroscience*, *13*(1), 129–154. https://doi.org/10.1146/annurev.neuro.13.1.129

Corneil, B. D., van Wanrooij, M., Munoz, D. P., & van Opstal, A. J. (2002). Auditory-visual interactions subserving goal-directed saccades in a complex scene. *Journal of Neurophysiology*, *88*(1), 438–454. https://doi.org/10.1152/jn.2002.88.1.438

Crossland, W. J., & Hughes, C. P. (1978). Observations on the afferent and efferent connections of the avian isthmo-optic nucleus. *Brain Research*, *145*(2), 239–256. https://doi.org/10.1016/0006-8993(78)90860-0

Davidson, B. L., Stein, C., Heth, J. A., Martins, I., Kotin, R. M., Derksen, T. A., . . . Chiorini, J. A. (2000). Recombinant adeno-associated virus type 2, 4, and 5 vectors: transduction of variant cell types and regions in the mammalian central nervous system. *Proceedings of the National Academy of Sciences of the United States of America*, *97*(7), 3428–3432. https://doi.org/10.1073/pnas.050581197

Davies, M. N. O., & Green, P. R. (1994). Multiple Sources of Depth Information: An Ecological Approach. In M. N. O. Davies & P. R. Green (Eds.), *Perception and Motor Control in Birds: An Ecological Approach* (pp. 339–356). Berlin, Heidelberg: Springer Berlin Heidelberg. https://doi.org/10.1007/978-3-642-75869-0_19

DeBello, W. M., & Knudsen, Eric. (2004). Multiple sites of adaptive plasticity in the owl's auditory localization pathway. *The Journal of Neuroscience: the Official Journal of the Society for Neuroscience*, *24*(31), 6853–6861. https://doi.org/10.1523/JNEUROSCI.0480-04.2004

Deng, Q., Rashid, A. J., Fernandez, F., Turner, R., Maler, L., & Dunn, R. J. (2005). A C-terminal domain directs Kv3.3 channels to dendrites. *The Journal of Neuroscience: the Official Journal of the Society for Neuroscience*, *25*(50), 11531–11541. https://doi.org/10.1523/JNEUROSCI.3672-05.2005

Deng, C., & Rogers, L. J. (2002). Prehatching visual experience and lateralization in the visual Wulst of the chick. Behavioural Brain Research, 134(1-2), 375–385. https://doi.org/10.1016/S0166-4328(02)00050-5

Domesick, V. B., & Morest, D.K. (1977). Migration and differentiation of shepherd's crook cells in the optic tectum of the chick embryo. *Neuroscience*, *2*(3), 477–491. https://doi.org/10.1016/0306-4522(77)90012-4

Dooling, R. J., Fay, R. R., & Popper, A. N. (2000). *Comparative Hearing: Birds and Reptiles*. *Springer Handbook of Auditory Research, 0947-2657: Vol. 13*. New York, NY: Springer New York; Imprint; Springer.

Eckert, D., Buhl, S., Weber, S., Jäger, R., & Schorle, H. (2005). The AP-2 family of transcription factors. *Genome Biology*, *6*(13).

Engelage, J., & Bischof, H.-J. The Orgnaization of the tectofugal pathway in birds_a comparative review, pp. 137–158.

Fedtsova, N., Quina, L. A., Wang, Shirong, & Turner, E. (2008). Regulation of the development of tectal neurons and their projections by transcription factors Brn3a and Pax7. *Developmental Biology*, *316*(1), 6–20. https://doi.org/10.1016/j.ydbio.2007.12.040

Fernandez, J., Taylor, R., & Bezanilla, F. (1983). Induced capacitance in the squid giant axon: Lipophilic ion displacement currents. *J. Gen. Physiol.*, *82*, 331–346.

Fink, A. E., Bender, K. J., Trussell, L. O., Otis, Thomas, DiGregorio, David, & Arabzadeh, E. (2012). Two-Photon Compatibility and Single-Voxel, Single-Trial Detection of Subthreshold Neuronal Activity by a Two-Component Optical Voltage Sensor. *PLoS ONE*, *7*(8), e41434. https://doi.org/10.1371/journal.pone.0041434

Förster, D., Arnold-Ammer, I., Laurell, E., Barker, A. J., Fernandes, A. M., Finger-Baier, K., . . . Kubo, F. (2017). Genetic targeting and anatomical registration of neuronal populations in the zebrafish brain with a new set of BAC transgenic tools. *Scientific Reports*, *7*(1), 5230. https://doi.org/10.1038/s41598-017-04657-x

Frost, B. J., & Nakayama, K. (1983). Single visual neurons code opposing motion independent of direction. Science, 220(4598), 744–745.

Frost, B. J., Wylie, D. R., & Wang, Y.-C. (1990). The processing of object and self-motion in the tectofugal and accessory optic pathways of birds. Vision Research, 30(11), 1677–1688.

Fujiwara, A., Ohozone, Y., & Naito, J. (2000). The Developmental Study on Lamination of the Optic Tectum in Relation to the Retinotectal Projection in Chicks and Chick Embryos. *Journal of Veterinary Medical Science*, *62*(5), 511–516. https://doi.org/10.1292/jvms.62.511

Funahashi, J.-i., Okafuji, T., Ohuchi, H., Noji, S., Tanaka, H., & Nakamura, H. (1999). Role of Pax-5 in the regulation of a mid-hindbrain organizer's activity. *Development, Growth and Differentiation*, *41*(1), 59–72. https://doi.org/10.1046/j.1440-169x.1999.00401.x

Gähwiler, B. (1997). Organotypic slice cultures: a technique has come of age. *Trends in Neurosciences*, *20*(10), 471–477. https://doi.org/10.1016/S0166-2236(97)01122-3

Garrido-Charad, F., Vega-Zuniga, T., Gutiérrez-Ibáñez, C., Fernandez, P., López-Jury, L., González-Cabrera, C., . . . Marín, Gonzalo J. (2018). "Shepherd's crook" neurons drive and synchronize the enhancing and suppressive mechanisms of the midbrain stimulus selection network. *Proceedings of the National Academy of Sciences*, 201804517. https://doi.org/10.1073/pnas.1804517115

Gill, F. (2007). *Ornithology* (3rd ed.). New York: W.H. Freeman.

Giolli, R. A., Blanks, R. H.I., & Lui, F. (2006). The accessory optic system: Basic organization with an update on connectivity, neurochemistry, and function. In *Progress in Brain Research. Neuroanatomy of the Oculomotor System* (Vol. 151, pp. 407–440). Elsevier. https://doi.org/10.1016/S0079-6123(05)51013-6

Goddard, C. A., Mysore, Shreesh, Bryant, A. S., Huguenard, J. R., & Knudsen, Eric. (2014). Spatially reciprocal inhibition of inhibition within a stimulus selection network in the avian midbrain. *PLoS ONE*, *9*(1), e85865. https://doi.org/10.1371/journal.pone.0085865

González, Jesus, & Tsien, R. Y. (1997). Improved indicators of cell membrane potential that use fluorescence resonance energy transfer. *Chemistry & Biology*, *4*(4), 269–277. https://doi.org/10.1016/S1074-5521(97)90070-3

González, Jesús, & Tsien, R. Y. (1995). Voltage sensing by fluorescence resonance energy transfer in single cells. *Biophysical Journal*. (69), 1272–1280.

Gray, G., Leber, S. M., & Sanes, J. (1990). Migratory patterns of clonally related cells in the developing central nervous system. *Experientia*, *46*(9), 929–940. https://doi.org/10.1007/BF01939386

Gray, Grace, & Sanes, Joshua. (1991). Migratory paths and phenotypic choices of clonally related cells in the avian optic tectum. *Neuron*, *6*(2), 211–225. https://doi.org/10.1016/0896-6273(91)90357-6

Gulledge, A. T., & Bravo, J. J. (2016). Neuron Morphology Influences Axon Initial Segment Plasticity. *ENeuro*, *3*(1). https://doi.org/10.1523/ENEURO.0085-15.2016

Gutiérrez-Ibáñez, C., Iwaniuk, A. N., Lisney, T. J., Faunes, M., Marín, Gonzalo J., & Wylie, Douglas R. (2012). Functional implications of species differences in the size and morphology of the isthmo optic nucleus (ION) in birds. *PLoS ONE*, *7*(5), e37816. https://doi.org/10.1371/journal.pone.0037816

Hamburger, V., & Hamilton, H. L. (1951). A series of normal stages in the development of the chick embryo. *Journal of Morphology*, *1*(88), 231–272.

Häusser, M., Stuart, Greg, Racca, C., & Sakmann, B. (1995). Axonal initiation and active dendritic propagation of action potentials in substantia nigra neurons. *Neuron*. (15), 637–647.

Hazan, Y., Kra, Y., Yarin, I., Wagner, H., & Gutfreund, Yoram. (2015). Visual-auditory integration for visual search: A behavioral study in barn owls. *Frontiers in Integrative Neuroscience*, *9*, 11. https://doi.org/10.3389/fnint.2015.00011

Hedstrom, K. L., Ogawa, Y., & Rasband, M. N. (2008). AnkyrinG is required for maintenance of the axon initial segment and neuronal polarity. *The Journal of Cell Biology*, *183*(4), 635–640. https://doi.org/10.1083/jcb.200806112

Hesse, K., Vaupel, K., Kurt, S., Buettner, R., Kirfel, J., & Moser, M. (2011). Ap-2δ is a crucial transcriptional regulator of the posterior midbrain. *PLoS ONE*, *6*(8), e23483. https://doi.org/10.1371/journal.pone.0023483

Heyers, D., Manns, M., Luksch, Harald, Güntürkün, O., & Mouritsen, H. (2008). Calcium-binding proteins label functional streams of the visual system in a songbird. *Brain Research Bulletin*, *75*(2-4), 348–355. https://doi.org/10.1016/j.brainresbull.2007.10.029

Higashijima, S.-i. (2008). Transgenic zebrafish expressing fluorescent proteins in central nervous system neurons. *Development, Growth & Differentiation*, *50*(6), 407–413. https://doi.org/10.1111/j.1440-169X.2008.01023.x

Hochbaum, D. R., Zhao, Y., Farhi, S. L., Klapoetke, N., Werley, C. A., Kapoor, V., . . . Cohen, A. (2014). All-optical electrophysiology in mammalian neurons using engineered microbial rhodopsins. *Nature Methods*, *11*(8), 825–833. https://doi.org/10.1038/nmeth.3000

Hodgkin, A. L., & Huxley, A. F. (1952). A quantitative description of membrane current and its application to conduction and excitation in nerve. *The Journal of Physiology*, *117*(4), 500–544.

Hodos, W., & Karten, H. (1970). Visual intensity and pattern discrimination deficits after lesions of ectostriatum in pigeons. The Journal of Comparative Neurology, 140(1), 53–68. https://doi.org/10.1002/cne.901400104

Holmes, Nicholas P.; Spence, Charles (2005): Multisensory integration: space, time and superadditivity. In: Current biology: CB 15 (18), R762-4. https://doi.org/10.1016/j.cub.2005.08.058.

Honig, M. G., & Hume, R. I. (1989). DiI and DiO: versatile fluorescent dyes for neuronal labelling and pathway tracing. *TINS*, *12*(9), 333–341.

Hu, W., Tian, C., Li, T., Yang, M., Hou, H., & Shu, Y. (2009). Distinct contributions of Nav1.6 and Nav1.2 in action potential initiation and backpropagation. *Nature Neuroscience*, *12*(8), 996–1002. https://doi.org/10.1038/nn.2359

Huang, G. (2017). Multimodal Integration in Shepherd´s Crook Neurons (Master Thesis). Technical University of Munich.

Huang, Y., Williams, J., & Johnson, S. M. (2012). Brain slice on a chip: opportunities and challenges of applying microfluidic technology to intact tissues. *Lab on a Chip*, *12*(12), 2103–2117. https://doi.org/10.1039/c2lc21142d

Jarvis, C. D. (1974). Visual discrimination and spatial localization deficits after lesions of the tectofugal pathway in pigeons. Brain, Behavior and Evolution, 9(3), 195–228. https://doi.org/10.1159/000123665

Jassik-Gerschenfeld, D., & Guichard, J. (1972). Visual receptive fields of single cells in the pigeon's optic tectum. *Brain Research*, *40*(2), 303–317. https://doi.org/10.1016/0006-8993(72)90136-9

Jenkins, S. M., & Bennett, V. (2001). Ankyrin-G coordinates assembly of the spectrin-based membrane skeleton, voltage-gated sodium channels, and L1 CAMs at Purkinje neuron initial segments. *The Journal of Cell Biology*, *155*(5), 739–746. https://doi.org/10.1083/jcb.200109026

Jiang, W., Jiang, H., & Stein, Barry. (2002). Two corticotectal areas facilitate multisensory orientation behavior. *Journal of Cognitive Neuroscience*, *14*(8), 1240–1255. https://doi.org/10.1162/089892902760807230

Karten, H., Hodos, W., Nauta, W. J., & Revzin, A. M. (1973). Neural connections of the "visual wulst" of the avian telencephalon. Experimental studies in the piegon (Columba livia) and owl (Speotyto cunicularia). *The Journal of Comparative Neurology*, *150*(3), 253–278. https://doi.org/10.1002/cne.901500303

Karten, Harvey, Cox, K., & Mpodozis, J. (1997). Two distinct populations of tectal neurons have unique connections within the retinotectorotundal pathway of the pigeon (Columba livia). *The Journal of Comparative Neurology*, *387*(3), 449–465. https://doi.org/10.1002/(SICI)1096-9861(19971027)387:3<449::AID-CNE10>3.3.CO;2-0

Kelly, James, P., & Cowan, W. M. (1972). Studies on the Development of the Chick Optic Tectum. III. Effects of Early Eye Removal. *Brain Research*, *42*, 263–288.

Khaliq, Zayd, M., Gouwens, Nathan, W., & Raman, I. M. (2003). The contribution of resurgent sodium current to high-frequency firing in purkinje neurons_an experimental and modeling study. *Journal of Neuroscience*. (23), 4899–4912.

King, Andrew J. (2005): Multisensory Integration. Strategies for Synchronization. In: Current Biology 15 (9), R339-R341. https://doi.org/10.1016/j.cub.2005.04.022.

Klump, G. M. (2013). Sound Localization in Birds. In R. R. Fay, A. N. Popper, & R. J. Dooling (Eds.), *Springer Handbook of Auditory Research. Comparative hearing: Birds and reptiles* (Vol. 13, pp. 249–307). [Place of publication not identified]: Springer. https://doi.org/10.1007/978-1-4612-1182-2_6

Knudsen, E., & Konishi, M. (1978). A neural map of auditory space in the owl. *Science*, *200*(4343), 795–797. https://doi.org/10.1126/science.644324

Knudsen, E. I. (1987). Neural derivation of sound source location in the barn owl. An example of a computational map. *Annals of the New York Academy of Sciences*, *510*, 33–38.

Knudsen, Eric. (1982). Auditory and visual maps of space in the optic tectum of the owl. *The Journal of Neuroscience*. (9), 1177–1194.

Knudsen, Eric. (2004). Sensitive periods in the development of the brain and behavior. *Journal of Cognitive Neuroscience*, *16*(8), 1412–1425. https://doi.org/10.1162/0898929042304796

Knudsen, Eric. (2007). Fundamental Components of Attention. *Annual Review of Neuroscience*, *30*(1), 57–78. https://doi.org/10.1146/annurev.neuro.30.051606.094256

Knudsen, Eric, Cohen, Y., & Masino, T. (1995). Characterization of a forebrain gaze field in the archistriatum of the barn owl-microstimulation and anatomical connections. *The Journal of Neuroscience*, *15*(7), 5139–5151.

Knudsen, Eric, & Knudsen, Phyllis. (1983). Space-Mapped auditory projections from the inferior colliculus to the optic tectum in the barn owl (Tyto alba). *Journal of Comparative Neurology*. (218), 187–196.

Kole, M. H.P., & Stuart, Greg J. (2012). Signal Processing in the Axon Initial Segment. *Neuron*, *73*(2), 235–247. https://doi.org/10.1016/j.neuron.2012.01.007

Köppl, C., & Carr, C. E. (2003). Computational diversity in the cochlear nucleus angularis of the barn owl. *Journal of Neurophysiology*, *89*(4), 2313–2329. https://doi.org/10.1152/jn.00635.2002

Krabichler, Q., Vega-Zuniga, T., Carrasco, D., Fernandez, M., Gutiérrez-Ibáñez, C., Marín, Gonzalo, & Luksch, Harald. (2017). The centrifugal visual system of a palaeognathous bird, the Chilean Tinamou (Nothoprocta perdicaria). *The Journal of Comparative Neurology*, *525*(11), 2514–2534. https://doi.org/10.1002/cne.24195

Kretzinger, U. (2008) (Master Thesis). Chair of Zoology, Technical University of Munich.

Kuba, H., Adachi, R., & Ohmori, H. (2014). Activity-Dependent and Activity-Independent Development of the Axon Initial Segment. *Journal of Neuroscience*, *34*(9), 3443–3453. https://doi.org/10.1523/JNEUROSCI.4357-13.2014

Kuba, Hiroshi, Oichi, Y., & Ohmori, Harunori. (2010). Presynaptic activity regulates Na+ channel distribution at the axon initial segment. *Nature*, *465*(7301), 1075–1078. https://doi.org/10.1038/nature09087

Kuenzel, T., Wirth, M. J., Luksch, Harald, Wagner, H., & Mey, Jorg. (2009). Increase of Kv3.1b expression in avian auditory brainstem neurons correlates with synaptogenesis in vivo and in vitro. *Brain Research*, *1302*, 64–75. https://doi.org/10.1016/j.brainres.2009.09.046

Lai, D., Brandt, Sebastian, Luksch, Harald, & Wessel, R. (2011). Recurrent antitopographic inhibition mediates competitive stimulus selection in an attention network. *Journal of Neurophysiology*, *105*(2), 793–805. https://doi.org/10.1152/jn.00673.2010

LaVail, J. H., & Cowan, W. M. (1971). The development of the chick optic tectum. I. normal morphology and cytoarchitectonic development. *Brain Research*, *28*(3), 391–419. https://doi.org/10.1016/0006-8993(71)90053-9

Lischka, K., Ladel, S., Luksch, Harald, & Weigel, Stefan. (2018). Expression patterns of ion channels and structural proteins in a multimodal cell type of the avian optic tectum. *The Journal of Comparative Neurology*, *526*(3), 412–424. https://doi.org/10.1002/cne.24340

Lischka, K., Yan, J., Weigel, Stefan, & Luksch, Harald. (2018). Effects of early eye removal on the morphology of a multisensory neuron in the chicken optic tectum. *Brain Research*, *1691*, 9–14. https://doi.org/10.1016/j.brainres.2018.04.018

Liu, C. (2013). Strategies for designing transgenic DNA constructs. *Methods in Molecular Biology (Clifton, N.J.)*, *1027*, 183–201. https://doi.org/10.1007/978-1-60327-369-5_8

Lorincz, A., & Nusser, Z. (2010). Molecular identity of dendritic voltage-gated sodium channels. *Science*, *328*(5980), 906–909. https://doi.org/10.1126/science.1187958

Low, L. K., & Cheng, H.-J. (2006). Axon pruning: An essential step underlying the developmental plasticity of neuronal connections. *Philosophical Transactions of the Royal Society of London. Series B, Biological Sciences*, *361*(1473), 1531–1544. https://doi.org/10.1098/rstb.2006.1883

Luksch, H. (2003). Cytoarchitecture of the avian optic tectum: neuronal substrate for cellular computation. *Reviews in the Neurosciences*, *14*(1-2), 85–106.

Luksch, Harald, Cox, K., & Karten, Harvey. (1998). Bottlebrush dendritic endings and large dendritic fields: Motion-detecting neurons in the tectofugal pathway. *Journal of Comparative Neurology*. (396), 399–414.

Luksch, Harald, & Golz, S. (2003). Anatomy and physiology of horizontal cells in layer 5b of the chicken optic tectum. *Journal of Chemical Neuroanatomy*, *25*(3), 185–194. https://doi.org/10.1016/S0891-0618(03)00010-3

Luksch, Harald, Karten, Harvey, Kleinfeld, D., & Wessel, R. (2001). Chattering and Differential Signal Processing in Identified Motion-Sensitive Neurons of Parallel Visual Pathways in the Chick Tectum. *The Journal of Neuroscience*, *21*(16), 6440–6446. https://doi.org/10.1523/JNEUROSCI.21-16-06440.2001

Luksch, Harald, Khanbabaie, R., & Wessel, R. (2004). Synaptic dynamics mediate sensitivity to motion independent of stimulus details. *Nature Neuroscience*, *7*(4), 380–388. https://doi.org/10.1038/nn1204

Luksch, Harald, & Poll, A. (2002). Early enucleation does not alter the gross morphology of identified projection neurons in the chicken optic tectum. *Neuroscience Letters*, *331*(1), 41–44. https://doi.org/10.1016/S0304-3940(02)00835-2

MacLeod, K. M., & Carr, C. E. (2005). Synaptic dynamics and intensity coding in the cochlear nucleus. In D. Pressnitzer, A. de Cheveigné, S. McAdams, & L. Collet (Eds.), *Auditory Signal Processing* (pp. 500–508). New York, NY: Springer New York. https://doi.org/10.1007/0-387-27045-0_61

Maczko, K. A., Knudsen, P., & Knudsen, E. I. (2006). Auditory and Visual Space Maps in the Cholinergic Nucleus Isthmi Pars Parvocellularis of the Barn Owl. *Journal of Neuroscience*, *26*(49), 12799–12806. https://doi.org/10.1523/JNEUROSCI.3946-06.2006

Mainen, Z. F., Joerges, J., Huguenard, J. R., & Sejnowski, T. J. (1995). A model of spike initiation in neocortical pyramidal neurons. *Neuron*, *15*(6), 1427–1439. https://doi.org/10.1016/0896-6273(95)90020-9

Marín, Gonzalo, Mpodozis, J., Mpdozis, J., Sentis, E., Ossandón, T., & Letelier, J. C. (2005). Oscillatory bursts in the optic tectum of birds represent re-entrant signals from the nucleus isthmi pars parvocellularis. *The Journal of Neuroscience : the Official Journal of the Society for Neuroscience*, *25*(30), 7081–7089. https://doi.org/10.1523/JNEUROSCI.1379-05.2005

Matsui, R., Tanabe, Y., Watanabe, D., & Balaban, E. (2012). Avian Adeno-Associated Virus Vector Efficiently Transduces Neurons in the Embryonic and Post-Embryonic Chicken Brain. *PLoS ONE*, *7*(11), e48730. https://doi.org/10.1371/journal.pone.0048730

Medina, L., & Reiner, A. (2000). Do birds possess homologues of mammalian primary visual, somatosensory and motor cortices? *Trends in Neurosciences*, *23*(1), 1–12. https://doi.org/10.1016/S0166-2236(99)01486-1

Medina-Kauwe, L. K. (2003). Endocytosis of adenovirus and adenovirus capsid proteins. *Advanced Drug Delivery Reviews*, *55*(11), 1485–1496. https://doi.org/10.1016/j.addr.2003.07.010

Melonakos, E. D., White, J. A., & Fernandez, F. (2016). Gain Modulation of Cholinergic Neurons in the Medial Septum-Diagonal Band of Broca Through Hyperpolarization. *Hippocampus*, *26*(12), 1525–1541. https://doi.org/10.1002/hipo.22653

Meredith, M. A., Nemitz, J. W., & Stein, B. E. (1987). Determinants of multisensory integration in superior colliculus neurons. I. Temporal factors. Journal of Neuroscience, 7(10), 3215–3229. Retrieved from http://www.jneurosci.org/content/jneuro/7/10/3215.full.pdf

Meredith, M. Alex, & Stein, Barry. (1986). Visual, auditory, and somatosensory convergence on cells in superior colliculus results in multisensory integration. *Journal of Neurophysiology*. (3).

Mey, Jörg, & Thanos, S. (2000a). Development of the visual system of the chick. *Brain Research Reviews*, *32*(2-3), 343–379. https://doi.org/10.1016/S0165-0173(99)00022-3

Mey, Jörg, & Thanos, S. (2000b). Development of the visual system of the chick. I. Cell differentiation and histogenesis. *Brain Research Reviews*, *32*, 343–379.

Meyer, U., Shao, J., Chakrabarty, S., Brandt, Sebastian F., Luksch, Harald, & Wessel, R. (2008). Distributed delays stabilize neural feedback systems. *Biological Cybernetics*, *99*(1), 79–87. https://doi.org/10.1007/s00422-008-0239-8

Miceli, Dom, Repérant, Jacques, Bavikati, R., Rio, Jean-Paul, & Volle, M. (1997). Brain-stem afferents upon retinal projecting isthmo-optic and ectopic neurons of the pigeon centrifugal visual system demonstrated by retrograde transneuronal transport of rhodamine β-isothiocyanate. *Visual Neuroscience*, *14*(02), 213–224. https://doi.org/10.1017/S0952523800011354

Miller, F. D., & Kaplan, D. R. (2003). Signaling mechanisms underlying dendrite formation. *Current Opinion in Neurobiology*, *13*(3), 391–398. https://doi.org/10.1016/S0959-4388(03)00072-2

Momose, T., Tonegawa, A., Takeuchi, J., Ogawa, H., Umesono, K., & Yasuda, K. (1999). Efficient targeting of gene expression in chick embryos by microelectroporation. *Development, Growth and Differentiation*, *41*(3), 335–344. https://doi.org/10.1046/j.1440-169X.1999.413437.x

Müller, S. C., & Scheich, H. (1985). Functional organization of the avian auditory field L. *Journal of Comparative Physiology a*, *156*(1), 1–12. https://doi.org/10.1007/BF00610661

Muramatsu, T., Mizutani, Y., Ohmori, Y., & Okumura, J.-i. (1997). Comparison of Three Nonviral Transfection Methods for Foreign Gene Expression in Early Chicken Embryosin Ovo. *Biochemical and Biophysical Research Communications*, *230*(2), 376–380. https://doi.org/10.1006/bbrc.1996.5882

Mysore, S., Asadollahi, A., & Knudsen, E. I. (2010). Global Inhibition and Stimulus Competition in the Owl Optic Tectum. *Journal of Neuroscience*, *30*(5), 1727–1738. https://doi.org/10.1523/JNEUROSCI.3740-09.2010

Nakamura, H., & Funahashi, J.-i. (2001). Introduction of DNA into Chick Embryos by *in Ovo* Electroporation. *Methods*, *24*(1), 43–48. https://doi.org/10.1006/meth.2001.1155

Nakamura, H., & Sugiyama, S. (2004). Polarity and laminar formation of the optic tectum in relation to retinal projection. *Journal of Neurobiology*, *59*(1), 48–56. https://doi.org/10.1002/neu.10339

Nakamura, H., Watanabe, Y., & Funahashi, J.-i. (2000). Misexpression of genes in brain vesicles by in ovo electropration. *Development, Growth & Differentiation*. (42), 199–201.

Niederleitner, B., Gutierrez-Ibanez, C., Krabichler, Q., Weigel, Stefan, & Luksch, Harald. (2016). A novel relay nucleus between the inferior colliculus and the optic tectum in the chicken (Gallus gallus). *Journal of Comparative Neurology*, *525*(3), 513–534. https://doi.org/10.1002/cne.24082

Niederleitner, B., & Luksch, Harald. (2012). Neuronal morphology in subdivisions of the inferior colliculus of chicken (Gallus gallus). *Journal of Chemical Neuroanatomy*, *44*(1), 24–33. https://doi.org/10.1016/j.jchemneu.2012.03.004

O'Donnell, J., Taylor, K., & Chapman, M. S. (2009). Adeno-associated virus-2 and its primary cellular receptor—Cryo-EM structure of a heparin complex. *Virology*, *385*(2), 434–443. https://doi.org/10.1016/j.virol.2008.11.037

Orbach, H. S., & Cohen, Lawrence, B. (1983). Optical monitoring of acivity from many areas of the *in vitro* and *in vivo* salamander olfactory bulb: A new method for studying functional organization in the vertebrate central nervous system. *The Journal of Neuroscience*, *3*(11), 2251–2262.

Osorio, N., Cathala, L., Meisler, M. H., Crest, M., Magistretti, J., & Delmas, P. (2010). Persistent Nav1.6 current at axon initial segments tunes spike timing of cerebellar granule cells. *The Journal of Physiology*, *588*(Pt 4), 651–670. https://doi.org/10.1113/jphysiol.2010.183798

Pakan, J. M. P., & Wylie, Douglas R. W. (2006). Two optic flow pathways from the pretectal nucleus lentiformis mesencephali to the cerebellum in pigeons (Columba livia). *The Journal of Comparative Neurology*, *499*(5), 732–744. https://doi.org/10.1002/cne.21108

Palmer, Lucy, & Stuart, Greg J. (2006). Site of action potential initiation in layer 5 pyramidal neurons. *The Journal of Neuroscience: the Official Journal of the Society for Neuroscience*, *26*(6), 1854–1863. https://doi.org/10.1523/JNEUROSCI.4812-05.2006

Parameshwaran, S., Carr, C. E., & Perney, T. M. (2001). Expression of the Kv3.1 potassium channel in the avian auditory brainstem. *Journal of Neuroscience*. (2), 485–494.

Parameshwaran-Iyer, S., Carr, C. E., & Perney, T. M. (2003). Localization of KCNC1 (Kv3.1) potassium channel subunits in the avian auditory nucleus magnocellularis and nucleus laminaris during development. *Journal of Neurobiology*, *55*(2), 165–178. https://doi.org/10.1002/neu.10198

Pena, J. L., & Gutfreund, Yoram. (2014). New perspectives on the owl's map of auditory space. *Current Opinion in Neurobiology*, *24*, 55–62. https://doi.org/10.1016/j.conb.2013.08.008

Pérez, M. L., & Peña, J. L. (2006). Comparison of midbrain and thalamic space-specific neurons in barn owls. *Journal of Neurophysiology*, *95*(2), 783–790. https://doi.org/10.1152/jn.00833.2005

Perney, T. M., & Kaczmarek, L. K. (1997). Localization of a high threshold potassium channel in the rat cochlear nucleus. *Journal of Comparative Neurology*, *386*(2), 178–202. https://doi.org/10.1002/(SICI)1096-9861(19970922)386:2<178::AID-CNE2>3.0.CO;2-Z

Perrins, C. (1990). *The illustrated encyclopaedia of birds: The definitive guide to birds of the world*. London: Headline.

Preuss, S. J., Trivedi, C. A., Vom Berg-Maurer, C. M., Ryu, S., & Bollmann, J. H. (2014). Classification of object size in retinotectal microcircuits. *Current Biology: CB*, *24*(20), 2376–2385. https://doi.org/10.1016/j.cub.2014.09.012

Quina, L. A., Pak, W., Lanier, J., Banwait, P., Gratwick, K., Liu, Y., . . . Turner, E. (2005). Brn3a-expressing retinal ganglion cells project specifically to thalamocortical and collicular visual pathways. *The Journal of Neuroscience: the Official Journal of the Society for Neuroscience*, *25*(50), 11595–11604. https://doi.org/10.1523/JNEUROSCI.2837-05.2005

Raman, I. M., Sprunger, L. K., Meisler, M. H., & Bean, B. P. (1997). Altered Subthreshold Sodium Currents and Disrupted Firing Patterns in Purkinje Neurons of Scn8a Mutant Mice. *Neuron*, *19*(4), 881–891. https://doi.org/10.1016/S0896-6273(00)80969-1

Ramón y Cajal, S. (1909). Histologie du système nerveux de l'homme & des vertébrés.

Reches, A., & Gutfreund, Y. (2008). Stimulus-Specific Adaptations in the Gaze Control System of the Barn Owl. *Journal of Neuroscience*, *28*(6), 1523–1533. https://doi.org/10.1523/JNEUROSCI.3785-07.2008

Repérant, J., Ward, R., Miceli, D., Rio, J., Médina, M., Kenigfest, N. B., & Vesselkin, N. P. (2006). The centrifugal visual system of vertebrates: A comparative analysis of its functional anatomical organization. *Brain Research Reviews*, *52*(1), 1–57. https://doi.org/10.1016/j.brainresrev.2005.11.008

Rogers, Lesley, J. (1995). The development of Brain and Behaviour in the Chicken. *TINS*, *7*(1), 245–248. https://doi.org/10.1127/ejm/7/1/0245

Rosa Salva, O., Mayer, U., & Vallortigara, G. (2015). Roots of a social brain: Developmental models of emerging animacy-detection mechanisms. *Neuroscience and Biobehavioral Reviews*, *50*, 150–168. https://doi.org/10.1016/j.neubiorev.2014.12.015

Royeck, M., Horstmann, M.-T., Remy, S., Reitze, M., Yaari, Y., & Beck, H. (2008). Role of axonal NaV1.6 sodium channels in action potential initiation of CA1 pyramidal neurons. *Journal of Neurophysiology*, *100*(4), 2361–2380. https://doi.org/10.1152/jn.90332.2008

Rubel, E. W., & Fritzsch, B. (2002). Auditory system development: Primary auditory neurons and their targets. *Annual Review of Neuroscience*, *25*, 51–101. https://doi.org/10.1146/annurev.neuro.25.112701.142849

Rudy B, McBain CJ. (2001). Kv3 channels: voltage-gated K+channels designed for high-frequency repetitive firing. *Trends in Neuroscience*. (24).

Rush, A. M., Dib-Hajj, S. D., & Waxman, S. G. (2005). Electrophysiological properties of two axonal sodium channels, Nav1.2 and Nav1.6, expressed in mouse spinal sensory neurones. *The Journal of Physiology*, *564*(Pt 3), 803–815. https://doi.org/10.1113/jphysiol.2005.083089

Schaub, Carina. (2018). (Master Thesis). Technical University of Munich

Scicolone, G., Ortalli, A. L., Alvarez, G., López-Costa, J. J., Rapacioli, M., Ferrán, J. L., Flores, V. (2006). Developmental pattern of NADPH-diaphorase positive neurons in chick optic tectum is sensitive to changes in visual stimulation. *The Journal of Comparative Neurology*, *494*(6), 1007–1030. https://doi.org/10.1002/cne.20878

Sebesteny, T., Davies, C., D., Zayatis, N., Németh, A., & Tömböl, T. (2002). The ramification and connections of retinal fibres in layer 7 of the domestic chick optic tectum: a Golgi impregnation, anterograde tracer and GABA-immunogold study. *J. Anat.*, *200*, 169–183.

Shao, J., Lai, D., Meyer, U., Luksch, Harald, & Wessel, R. (2009). Generating oscillatory bursts from a network of regular spiking neurons without inhibition. *Journal of Computational Neuroscience*, *27*(3), 591–606. https://doi.org/10.1007/s10827-009-0171-5

Shin, D. H., Lee, K.-S., Lee, E., Cho, S., Kim, Jaehyup, Kim, Jong, . . . Lee, W. (2003). The correspondence between the labeling patterns of antibody RT97, neurofilaments, microtubule associated protein 1B and tau varies with cell types and development stages of chicken retina. *Neuroscience Letters*, *342*(3), 167–170. https://doi.org/10.1016/S0304-3940(03)00276-3

Simpson, J. I. (1984). The Accessory Optic System. Annual Review of Neuroscience, 7, 13–41.

Simpson, J. I., Leonard, C. S., & Soodak, R. E. (1988). The Accessory Optic System Analyzer of Self-Motion a. Annals of the New York Academy of Sciences, 545(1), 170–179. https://doi.org/10.1111/j.1749-6632.1988.tb19562.x

Sjulson, L., & Miesenböck, G. (2007). Optical recording of action potentials and other discrete physiological events: a perspective from signal detection theory. *Physiology (Bethesda, Md.)*, *22*, 47–55. https://doi.org/10.1152/physiol.00036.2006

Sjulson, L., & Miesenböck, G. (2008). Rational optimization and imaging in vivo of a genetically encoded optical voltage reporter. *The Journal of Neuroscience: the Official Journal of the Society for Neuroscience*, *28*(21), 5582–5593. https://doi.org/10.1523/JNEUROSCI.0055-08.2008

Spitzer, M. W., Bala, A. D. S., & Takahashi, T. T. (2004). A neuronal correlate of the precedence effect is associated with spatial selectivity in the barn owl's auditory midbrain. *Journal of Neurophysiology*, *92*(4), 2051–2070. https://doi.org/10.1152/jn.01235.2003

Sridharan, D., & Knudsen, Eric. (2015). Gamma oscillations in the midbrain spatial attention network: Linking circuits to function. *Current Opinion in Neurobiology*, *31*, 189–198. https://doi.org/10.1016/j.conb.2014.11.006

Stanford, T. R., Quessy, S., & Stein, Barry. (2005). Evaluating the operations underlying multisensory integration in the cat superior colliculus. *The Journal of Neuroscience : the Official Journal of the Society for Neuroscience*, *25*(28), 6499–6508. https://doi.org/10.1523/JNEUROSCI.5095-04.2005

Stein, B., Meredith, M. A., Huneycutt, W. S., & McDade, L. (1989). Behavioral Indices of Multisensory Integration: Orientation to Visual Cues is Affected by Auditory Stimuli. *Journal of Cognitive Neuroscience*, *1*(1), 12–24. https://doi.org/10.1162/jocn.1989.1.1.12

Stein, Barry, & Meredith, M. Alex. (1994). *The merging of the senses* (2. print). *Cognitive neuroscience series*. Cambridge, Mass.: MIT Press.

Stein, Barry, Scott Huneycutt, W., & Alex Meredith, M. (1988). Neurons and behavior: the same rules of multisensory integration apply. *Brain Research*, *448*(2), 355–358. https://doi.org/10.1016/0006-8993(88)91276-0

Stein, Barry, & Stanford, T. R. (2008). Multisensory integration: current issues from the perspective of the single neuron. *Nature Reviews Neuroscience*, *9*(4), 255–266. https://doi.org/10.1038/nrn2331

Stein, Barry, Stanford, T. R., Ramachandran, R., Perrault, T. J., & Rowland, B. A. (2009). Challenges in quantifying multisensory integration: Alternative criteria, models, and inverse effectiveness. *Experimental Brain Research*, *198*(2-3), 113–126. https://doi.org/10.1007/s00221-009-1880-8

Stein, Barry, Stanford, T. R., & Rowland, B. A. (2014). Development of multisensory integration from the perspective of the individual neuron. *Nature Reviews Neuroscience*, *15*(8), 520–535. https://doi.org/10.1038/nrn3742

Stuart, Gary, Vielkind, J. R., McMurray, J. V., & Westerfield, M. (1990). Stable lines of transgenic zebrafish exhibit reproducible patterns of transgene expression. *Development*, *109*, 577–584.

Sullivan, W. E., & Konishi, M. (1984). Segregation of stimulus phase and intensity coding in the cochlear nucleus of the barn owl. *The Journal of Neuroscience*, *4*(7), 1787–1799. https://doi.org/10.1523/JNEUROSCI.04-07-01787.1984

Surace, E. M., & Auricchio, A. (2008). Versatility of AAV vectors for retinal gene transfer. *Vision Research*, *48*(3), 353–359. https://doi.org/10.1016/j.visres.2007.07.027

Thome, C., Kelly, T., Yanez, A., Schultz, C., Engelhardt, M., Cambridge, S. B., . . . Egorov, A. V. (2014). Axon-Carrying Dendrites Convey Privileged Synaptic Input in Hippocampal Neurons. *Neuron*, *83*(6), 1418–1430. https://doi.org/10.1016/j.neuron.2014.08.013

Ting, J. T., Daigle, T. L., Chen, Q., & Feng, G. (2014). Acute brain slice methods for adult and aging animals: application of targeted patch clamp analysis and optogenetics. *Methods in Molecular Biology (Clifton, N.J.)*, *1183*, 221–242. https://doi.org/10.1007/978-1-4939-1096-0_14

Triarhou, L. C. (2014). Axons emanating from dendrites: phylogenetic repercussions with Cajalian hues. *Frontiers in Neuroanatomy*, *8*, 347. https://doi.org/10.3389/fnana.2014.00133

Turner, R., Maler, L., Deerinck, T., Levinson, S, Rock, & Ellisman, M. H. (1994). TTX-sensitive dendritic sodium channels underlie oscillatory discharge in a vertebrate sensory neuron. *The Journal of Neuroscience*. (14), 6453–6471.

Uchiyama, H., Ohno, H., & Kodama, R. (2012). Lesion of the isthmo-optic nucleus impairs target selection for visually guided reaching. *Behavioural Brain Research*, *233*(2), 359–366. https://doi.org/10.1016/j.bbr.2012.05.008

Vega-Zuniga, T., Mpodozis, J., Karten, Harvey, Marín, Gonzalo, Hain, S., & Luksch, Harald. (2014). Morphology, projection pattern, and neurochemical identity of Cajal's "centrifugal neurons": The cells of origin of the tectoventrogeniculate pathway in pigeon (Columba livia) and chicken (Gallus gallus). *Journal of Comparative Neurology*, *522*(10), 2377–2396. https://doi.org/10.1002/cne.23539

Vega-Zuniga, T., Trost, D., Schicker, K., Bogner, E. M., & Luksch, Harald. (2018). The Medial Ventrothalamic Circuitry: Cells Implicated in a Bimodal Network. *Frontiers in Neural Circuits*, *12*, 9. https://doi.org/10.3389/fncir.2018.00009

Verhaal, J., & Luksch, Harald. (2016a). Multimodal integration in the chicken. *The Journal of Experimental Biology*, *219*(Pt 1), 90–95. https://doi.org/10.1242/jeb.129387

Verhaal, J., & Luksch, Harald. (2016b). Neuronal responses to motion and apparent motion in the optic tectum of chickens. *Brain Research*, *1635*, 190–200. https://doi.org/10.1016/j.brainres.2016.01.022

Voll, K. (2015). Signal propagation in eGFP expressing neurons of the chicken optic tectum (Master Thesis). Technical University of Munich.

Vroomen, J., & Keetels, M. (2010). Perception of intersensory synchrony: a tutorial review. In: *Attention, perception & psychophysics, 72(4)*, 871–884, https://doi.org/10.3758/APP.72.4.871.

Wallace, M. T., & Stein, Barry. (1997). Development of Multisensory Neurons and Multisensory Integration in Cat Superior Colliculus. *The Journal of Neuroscience*, *17*(7), 2429–2444. https://doi.org/10.1523/JNEUROSCI.17-07-02429.1997

Wang, D., Zhang, Z., Chanda, B., & Jackson, M. B. (2010). Improved Probes for Hybrid Voltage Sensor Imaging. *Biophysical Journal*, *99*(7), 2355–2365. https://doi.org/10.1016/j.bpj.2010.07.037

Wang, L.-Y., Gan, Li, Forsythe, I. D., & Kaczmarek, L. K. (1998). Contribution of the Kv3.1 potassium channel to high-frequency firing in mouse auditory neurones. *The Journal of Physiology*, *509*(Pt 1), 183–194. https://doi.org/10.1111/j.1469-7793.1998.183bo.x

Wang, Steven, Mu, X., Bowers, W. J., Kim, D.-S., Plas, D. J., Crair, M. C., . . . Klein, W. H. (2002). Brn3b/Brn3c double knockout mice reveal an unsuspected role for Brn3c in retinal ganglion cell axon outgrowth. *Development*, *129*, 467–477.

Wang, Y., Brzozowska-Prechtl, A., & Karten, Harvey. (2010). Laminar and columnar auditory cortex in avian brain. *Proceedings of the National Academy of Sciences of the United States of America*, *107*(28), 12676–12681. https://doi.org/10.1073/pnas.1006645107

Wang, Y., & Karten, Harvey. (2010). Three subdivisions of the auditory midbrain in chicks (Gallus gallus) identified by their afferent and commissural projections. *The Journal of Comparative Neurology*, *518*(8), 1199–1219. https://doi.org/10.1002/cne.22269

Wang, Y., Luksch, Harald, Brecha, N. C., & Karten, Harvey. (2006). Columnar projections from the cholinergic nucleus isthmi to the optic tectum in chicks (Gallus gallus): A possible substrate for synchronizing tectal channels. *The Journal of Comparative Neurology*, *494*(1), 7–35. https://doi.org/10.1002/cne.20821

Wang, Y., Major, D. E., & Karten, Harvey. (2004). Morphology and connections of nucleus isthmi pars magnocellularis in chicks (Gallus gallus). *The Journal of Comparative Neurology*, *469*(2), 275–297. https://doi.org/10.1002/cne.11007

Wang, Y., Zorio, D. A. R., & Karten, Harvey. (2017). Heterogeneous organization and connectivity of the chicken auditory thalamus (Gallus gallus). *The Journal of Comparative Neurology*, *525*(14), 3044–3071. https://doi.org/10.1002/cne.24262

Watanabe, Y., Sakuma, C., & Yaginuma, H. (2014). Nrp1-mediated Sema3A signals coordinate laminar formation in the developing chick optic tectum. *Development (Cambridge, England)*, *141*(18), 3572–3582. https://doi.org/10.1242/dev.110205

Watanabe, Y., Sakuma, C., & Yaginuma, H. (2018). Dispersing movement of tangential neuronal migration in superficial layers of the developing chick optic tectum. *Developmental Biology*, *437*(2), 131–139. https://doi.org/10.1016/j.ydbio.2018.03.010

Watanabe, Y., & Yaginuma, H. (2015). Tangential cell migration during layer formation of chick optic tectum. *Development, Growth & Differentiation*, *57*(8), 539–543. https://doi.org/10.1111/dgd.12238

Weigel, S., Flisikowska, T., Schnieke, A., & Luksch, H. (2014). Hybrid voltage sensor imaging of eGFP-F expressing neurons in chicken midbrain slices. *Journal of Neuroscience Methods*, *233*, 28–33. https://doi.org/10.1016/j.jneumeth.2014.05.034

Wild, J. M. (1985). The avian somatosensory system. I. Primary spinal afferent input to the spinal cord and brainstem in the pigeon (Columba livia). *The Journal of Comparative Neurology*, *240*(4), 377–395. https://doi.org/10.1002/cne.902400406

Wild, J. M. (1995). Convergence of somatosensory and auditory projections in the avian torus semicircularis, including the central auditory nucleus. *The Journal of Comparative Neurology*, *358*(4), 465–486. https://doi.org/10.1002/cne.903580402

Winkowski, D. E., & Knudsen, E. I. (2007). Top-Down Control of Multimodal Sensitivity in the Barn Owl Optic Tectum. *Journal of Neuroscience*, *27*(48), 13279–13291. https://doi.org/10.1523/JNEUROSCI.3937-07.2007

Witten, I. B., & Knudsen, Eric. (2005). Why Seeing Is Believing: Merging Auditory and Visual Worlds. *Neuron*, *48*(3), 489–496. https://doi.org/10.1016/j.neuron.2005.10.020

Wong, R., & Ghosh, A. (2002). Activity-dependent regulation of dendritic growth and patterning. *Nature Reviews. Neuroscience*, *3*(10), 803–812. https://doi.org/10.1038/nrn941

Woolley, S. M. N., & Casseday, J. H. (2004). Response properties of single neurons in the zebra finch auditory midbrain: response patterns, frequency coding, intensity coding, and spike latencies. *Journal of Neurophysiology*, *91*(1), 136–151. https://doi.org/10.1152/jn.00633.2003

Woolley, S. M. N., Gill, P., & Theunissen, F. E. (2006). Stimulus-dependent auditory tuning results in synchronous population coding of vocalizations in the songbird midbrain. *The Journal of Neuroscience: the Official Journal of the Society for Neuroscience*, *26*(9), 2499–2512. https://doi.org/10.1523/JNEUROSCI.3731-05.2006

Wu, C.-C., Russell, R.M., Nguyen, R.T., & Karten, H.J. (2003). Tracing developing pathways in the brain: a comparison of carbocyanine dyes and cholera toxin b subunit. *Neuroscience*, *117*(4), 831–845. https://doi.org/10.1016/S0306-4522(02)00833-3

Wylie, Douglas R. W., Gutierrez-Ibanez, C., Pakan, J. M. P., & Iwaniuk, A. N. (2009). The optic tectum of birds: Mapping our way to understanding visual processing. *Canadian Journal of Experimental Psychology/Revue Canadienne De Psychologie Expérimentale*, *63*(4), 328–338. https://doi.org/10.1037/a0016826

Wylie, Douglas R. W., Pakan, J. M. P., Elliott, C. A., Graham, D. J., & Iwaniuk, A. N. (2007). Projections of the nucleus of the basal optic root in pigeons (Columba livia): a comparison of the morphology and distribution of neurons with different efferent projections. *Visual Neuroscience*, *24*(5), 691–707. https://doi.org/10.1017/S0952523807070599

Yamagata, M., Weiner, J. A., Dulac, C., Roth, K. A., & Sanes, Joshua. (2006). Labeled lines in the retinotectal system: Markers for retinorecipient sublaminae and the retinal ganglion cell subsets that innervate them. *Molecular and Cellular Neuroscience*, *33*(3), 296–310. https://doi.org/10.1016/j.mcn.2006.08.001

Yang, C., Li, X., Li, Q., Fu, S. L., Li, H., Guo, Z. K., . . . Zhao, S. (2014). Evaluation of three different promoters driving gene expression in developing chicken embryo by using in vivo electroporation. *Genetics and Molecular Research : GMR*, *13*(1), 1270–1277. https://doi.org/10.4238/2014.February.27.12

Yuan, A., Rao, M. V., Veeranna, & Nixon, R. A. (2012). Neurofilaments at a glance. *Journal of Cell Science*, *125*(14), 3257–3263. https://doi.org/10.1242/jcs.104729

Zahar, Y., Reches, A., & Gutfreund, Y. (2008). Multisensory Enhancement in the Optic Tectum of the Barn Owl: Spike Count and Spike Timing. *Journal of Neurophysiology*, *101*(5), 2380–2394. https://doi.org/10.1152/jn.91193.2008

Zeng, H., & Sanes, Joshua. (2017). Neuronal cell-type classification: challenges, opportunities and the path forward. *Nature Reviews. Neuroscience*, *18*(9), 530–546. https://doi.org/10.1038/nrn.2017.85

Zhang, L., & Poo, M. M. (2001). Electrical activity and development of neural circuits. *Nature Neuroscience*, *4 Suppl*, 1207–1214. https://doi.org/10.1038/nn753

Abbrevations

AIS	axon initial segment
Aivm	ventromedial portion of the intermediate arcopallium
bp	base pair
CAG	CMV early enhancer / chicken β actin
CM	caudal nidopallium
CMV	cytomegalovirus
DCN	dorsal column and external cuneate nuclei
DiO	3,3'-dioctadecyloxa-carbocyanine perchlorate
DPA	dipicrylamine
eGFP	cytosolic GFP
EPSP	excitatory postsynaptic potential
FRET	Förster resonance energy transfer
FRLx	external part of the formatio reticularis lateralis
GABA	γ-aminobutyric acid
GFP	green fluorescence protein
GLd	nucleus geniculatius lateralis pars dorsalis
HH	Hamburger Hamilton stage
IC	inferior colliculus
ICc	central part of the inferior colliculus
ICx	external part of the inferior colliculus
ILD	interaural level difference

IMC	nucleus isthmi pars magnocellularis
ION	istmo-optic nucleus
IPC	nucleus isthmi pars parvocellularis
ISI	interstimulus interval
ITD	interaural time difference
LM	nucleus lentiformis mesencephalic
mGFP	farnesylated GF
MLd	nucleus mesencephalicus lateralis pars dorsalis
nBOR	nucleus of the basal optic root
NA	nucleus angularis
Nd	dorsal nidopallium
NGS	normal goat serum
NHS	normal horse serum
NM	nucleus magnocellularis
OPT	nucleus opticus principalis thalami
Ov	nucleus ovoidalis
p	plasmid
PB	phosphate buffer
PBS	phosphate buffer with 0.75 % NaCl
PCR	Polymerase Chain Reaction
rAAAV	recombinant avian adeno-associated viral vector
rAAV	recombinant adeno-associated viral vector
RCAS	Replication-Competent ASLV long terminal repeat (LTR) with a splice acceptor
RGC	retinal ganglion cell

RI	regio intermedius
SAC	stratum album centrale
SC	superior colliculus
SCN	Shepherd’s crook neuron
SFP	stratum fibrosum periventriculare
SGC	stratum griseum centrale
SGFS	stratum griseum et fibrosum superficiale
SGP	stratum griseum periventriculare
SLU	nucleus isthmi pars semiluminaris
SO	stratum opticum
TeO	optic tectum

List of figures

List of tables

Anhang I

Eidesstattliche Erklärung

Ich erkläre an Eides statt, dass ich die bei der Fakultät Wissenschaftszentrum Weihenstephan für Ernährung, Landnutzung und Umwelt der TUM zur Promotionsprüfung vorgelegte Arbeit mit dem Titel ‚Multimodal integration in single neurons in the midbrain of chicken (*Gallus gallus domesticus*)' am Lehrstuhl für Zoologie unter der Anleitung und Betreuung durch Prof. Dr. Harald Luksch ohne sonstige Hilfe erstellt und bei der Abfassung nur die gemäß § 6 Ab. 6 und 7 Satz 2 angebotenen Hilfsmittel benutzt habe.

Ich habe keine Organisation eingeschaltet, die gegen Entgelt Betreuerinnen und Betreuer für die Anfertigung von Dissertationen sucht, oder die mir obliegenden Pflichten hinsichtlich der Prüfungsleistungen für mich ganz oder teilweise erledigt.

Ich habe die Dissertation in dieser oder ähnlicher Form in keinem anderen Prüfungsverfahren als Prüfungsleistung vorgelegt.

Ich habe den angestrebten Doktorgrad noch nicht erworben und bin nicht in einem früheren Promotionsverfahren für den angestrebten Doktorgrad endgültig gescheitert.

Die öffentlich zugängliche Promotionsordnung der TUM ist mir bekannt, insbesondere habe ich die Bedeutung von § 28 (Nichtigkeit der Promotion) und § 29 (Entzug des Doktorgrades) zur Kenntnis genommen. Ich bin mir der Konsequenzen einer falschen Eidesstattlichen Erklärung bewusst.

Mit der Aufnahme meiner personenbezogenen Daten in die Alumni-Datei der TUM bin ich einverstanden.

Ort, Datum, Unterschrift

Curriculum Vitae

ACADEMIC EDUCATION

05/2015 - 10/2018	Doctoral thesis under the supervision of Prof. Dr. Harald Luksch and Dr. Stefan Weigel Technical University of Munich, Department of Animal Science, Chair of Zoology Title: “Multimodal integration in single neurons in the midbrain of chicken (*Gallus gallus domesticus*)”
10/2011 - 09/2014	Master programme M.Sc. Molecular Ecology University of Bayreuth, Department of Biology, Chemistry, and Earth Sciences Master thesis: “Calcium imaging in Mauthner cells during habituation in zebrafish”
10/2008 - 09/2011	Bachelor programme B.Sc. Biology University of Bayreuth, Department of Biology, Chemistry, and Earth Sciences Bachelor thesis: “Temperature-dependence of response properties of leech sensory neurons”

Acknowledgements

I am very gratefully to my Doktorvater Prof. Dr. Harald Luksch. During the time of my thesis he continuously supported the project and motivated me. His scientific guidance helped me in all the time of project work and writing.

I am also very grateful to my supervisor Dr. Stefan Weigel for giving me the opportunity to work on this extremely interesting project. Through his assistance I was able to gain immense knowledge on relevant topics for the multimodal integration project. His continuous supporting during experimental work, data analysis and writing essentially contributed to the outcome of this research project.

I want to thank the collaborators of this project: Prof. Dr. Benjamin Schusser and Theresa Thoma for sharing their knowledge on plasmid construction and western blotting; Dr. habil. Tatiana Filisikowska for helping me with the plasmid construction at the beginning of the *in ovo* electroporation project; and Dr. Thomas Künzel for supporting the project with his immense knowledge on modelling.

Thanks to Birgit Seibel for laboratory assistance, Yvonne Schwarz for the help in antibody staining and *in ovo* electroporation and Gaby Schwabedissen for the help in *in ovo* electroporation.

I want to thank the students Simone Ladel and Jiamin Yan for significantly contributing to the results in this thesis.

I also want to thank Dr. Klaus Michel for being my mentor.

I thank Dr. Lutz Kettler for comments on an earlier version of this thesis.

Thanks to Quirin Krabichler, Wolfgang Greiter, Max Bothe, Stephen Hörpel, Michi Forsthofer, and Gianmarco Maldarelli for the pleasant atmosphere in our PhD office.

Last but not least, thanks to all the other members and former members of the Chair of Zoology for creating such a nice working environment.